Heterogeneity versus Anisotropy and the State of Stress in Stable Cratons: Observations from a Deep Borehole of Opportunity in Northeastern Alberta, Canada

Wenjing Wang[1], Douglas Ray Schmitt[1], and Judith Chan[2]

[1]Purdue University
[2]Earth Signal Processing Ltd.

November 23, 2022

Abstract

Geophysical logs collected from a deep borehole drilled to the Canadian Shield in Northeastern Alberta shed valuable lights on the state of stress in stable cratons. Observed breakout azimuths rotate between three depth intervals, from N100°E at 1650-2000 m to N173°E at 2000-2210 m, and finally to N145°E at the bottom. No obvious fractures that might disturb stresses were found; and these rotating breakouts can be interpreted either as being due to a heterogenous stress field or formation elastic and strength anisotropy. The latter interpretation is favored because the breakout azimuths are strongly controlled by rock metamorphic textures as validated by their close correlations with both dip directions of foliation planes and polarization directions from dipole sonic logs. Monte Carlo realizations further demonstrate that anisotropic metamorphic rocks subjected to a uniform horizontal stress direction could result in the observed azimuth-rotating breakouts. The stress magnitudes inferred from this analysis, which incorporates both the rock anisotropy and weak foliation failure planes, suggest a normal faulting regime and a maximum horizontal compression direction consistent with that in the overlying Western Canadian Sedimentary Basin (NE-SW) and the motion of the North American plate. The inferred stress magnitudes are low and Mohr-Coulomb analyses demonstrate that the formation is not near the critical loading for slip on weak planes. However, more detailed investigations should be conducted since Monte Carlo calculations indicate that analyses from breakout widths, particularly when a conventional Kirsch-based formula is employed, are highly nonunique, allowing for large variations in potential stress states.

Posted on 23 Nov 2022 — CC-BY-NC 4 — https://doi.org/10.1002/essoar.10512083.1 — This a preprint and has not been peer reviewed. Data may be preliminary.

Heterogeneity versus Anisotropy and the State of Stress in Stable Cratons: Observations from a Deep Borehole of Opportunity in Northeastern Alberta, Canada

Wenjing Wang[1*], Douglas R. Schmitt[1,3], Judith Chan[2,3]

[1] Earth, Atmospheric, and Planetary Sciences Department, Purdue University, West Lafayette, Indiana, USA, 47907

[2] Earth Signal Processing Ltd., Calgary, Alberta, Canada, T2P 2X6

[3] Formerly, Department of Physics, University of Alberta, Edmonton, Alberta, Canada, T6G 2E1

[*] Corresponding author: Wenjing Wang (wang4084@purdue.edu)

Key Points:

- Image and geophysical logs are obtained in a borehole drilled to nearly 2.5 km in the stable metamorphic craton in north-east Alberta.
- Breakout directions change over distinct depth sections; and these mostly correlate with metamorphic foliations and elastic anisotropy.
- Breakout morphologies, interpreted using Monte Carlo simulations within the weak failure plane model, indicate low stress magnitudes.

Abstract

Geophysical logs collected from a deep borehole drilled to the Canadian Shield in Northeastern Alberta shed valuable lights on the state of stress in stable cratons. Observed breakout azimuths rotate between three depth intervals, from N100°E at 1650-2000 m to N173°E at 2000-2210 m, and finally to N145°E at the bottom. No obvious fractures that might disturb stresses were found; and these rotating breakouts can be interpreted either as being due to a heterogenous stress field or formation elastic and strength anisotropy. The latter interpretation is favored because the breakout azimuths are strongly controlled by rock metamorphic textures as validated by their close correlations with both dip directions of foliation planes and polarization directions from dipole sonic logs. Monte Carlo realizations further demonstrate that anisotropic metamorphic rocks subjected to a uniform horizontal stress direction could result in the observed azimuth-rotating breakouts. The stress magnitudes inferred from this analysis, which incorporates both the rock anisotropy and weak foliation failure planes, suggest a normal faulting regime and a maximum horizontal compression direction consistent with that in the overlying Western Canadian Sedimentary Basin (NE-SW) and the motion of the North American plate. The inferred stress magnitudes are low and Mohr-Coulomb analyses demonstrate that the formation is not near the critical loading for slip on weak planes. However, more detailed investigations should be conducted since Monte Carlo calculations indicate that analyses from breakout widths, particularly when a conventional Kirsch-based formula is employed, are highly nonunique, allowing for large variations in potential stress states.

Plain Language Summary

Drilling induced failure patterns are extensively exploited to infer the state of stress in the subsurface. Directions of these patterns along the depth are widely observed to have variations but the common practice is averaging to get a single number. However, in our observations from a unique borehole drilled to the crystalline basement in Northeastern Alberta, the directions rotate dramatically along three depth intervals, rendering the simple averaging approach infeasible. In addition, the shape of failure patterns exhibits a crescent moon shape, instead of a conventional rectangular vertical patch. Here, we attribute the anomalous direction rotations to the different rock strength while the rock is compressed at different angles, referred as strength anisotropy. The assertion of strength anisotropy is backed up by the observations of layered weak rock structures.

Simulations further qualitatively demonstrate that rocks with anisotropic strength under a constant compressive stress direction fail in the weak planes, influencing the direction of failure patterns. Therefore, when working in anisotropic rock formations for the state of stress, the effect of anisotropy should be a predominant consideration instead of a simple averaging.

Keywords: in-situ stress, strength anisotropy, stress rotation, cratonic tectonics, geophysical logging

1 Introduction

Our knowledge of the state of stress within the metamorphic cores of Precambrian cratons remains scant. This is readily confirmed in a cursory examination of the World Stress Map (Heidbach et al., 2018) with blank zones over the vast cratonic regions of North America, Eurasia, Australia, and Africa. There are, of course, many stress indicators reported from boreholes drilled into the overlying platforms, but the bulk of the indicators came from resource-based drillings only into the veneer of sediments, as is certainly the case in the study area (Figure 1). The reasons for scarcity of information range from the lack of drilling targets of economic interests to the aseismicity in these tectonically stable areas. Certainly, large numbers of boreholes have been drilled shallowly into the cratons most often for mine exploration and development and for liquid waste disposal, but data from these are rarely available.

Our recent demands for geothermal energy and fluid waste disposal often exploit the deepest sediments that immediately overlie the cratons; and this means that the presumably “stable” cratons can no longer be safely ignored. Indeed, there have already been notable consequences arising from waste fluid disposal into or adjacent to the cratons, with the earliest example of this being perhaps the series of earthquakes near Denver in the 1960s, which were induced by injection of pressurized chemical wastes directly into the Precambrian basement at the Rocky Mountain Arsenal (e.g., Healy et al., 1968).

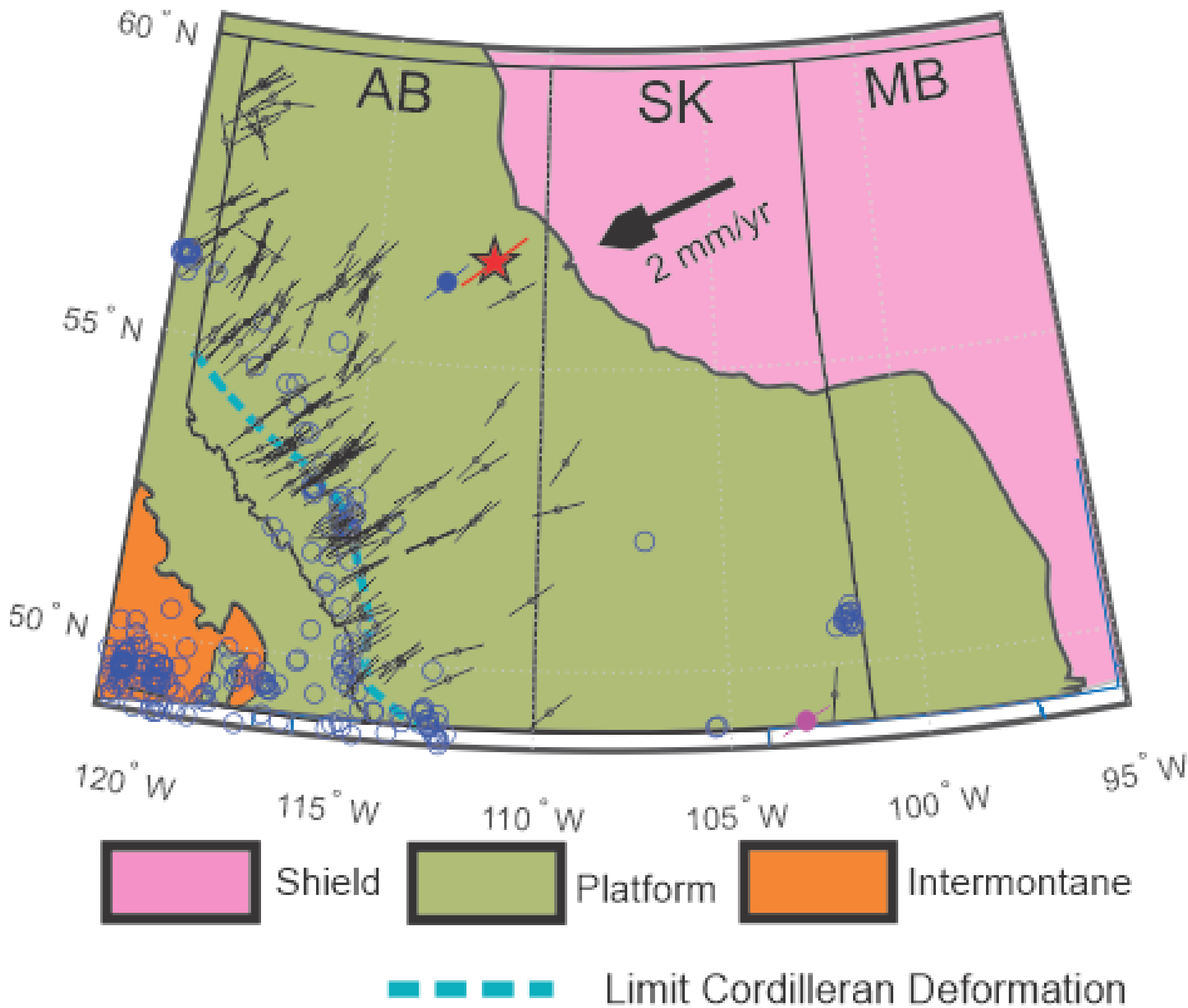

Figure 1. Simplified bedrock geological map showing the location of the Hunt Well in NE Alberta (denoted by the red star) in relation to portions of the Shield (pink) and Platform (light green) as defined according to the presence of sedimentary formations and Intermontane (orange) of the North American Craton. Black circles indicate the position of stress directions determined from borehole observations in the Phanerozoic sediments as indicated by the throughgoing line orientation from the World Stress Map 2016 compilation (Heidbach et al., 2018), more recent determinations of Shen et al. (2019) and Shen et al. (2021), other observations by Morin (2017) in NE Alberta (blue large dot) and Stork et al. (2018) in deep SE Saskatchewan. Relative plate motion of 2 mm/year with azimuth 244.5° obtained using the GRMS v2.1 (Kreemer et al., 2014) is shown by the thick black arrow. The eastern limit of the Cordilleran deformation front (CDF) is indicated by the light blue dashed line. The epicenters of all the events > M_b 2.5 in the area from 1980 to 2021 from the USGS database (https://earthquake.usgs.gov/earthquakes/search/) are shown as open blue circles. Please refer to Text S1 for more detailed information on data sources.

Currently, however, societally important efforts are focusing on the disposal of large volumes of produced brines or greenhouse gases via injection into the deepest porous Phanerozoic sediments that, in many locales globally, rest nonconformally upon the Precambrian crystalline basement at the "Great Unconformity" (Marshak et al., 2017); and there are now numerous examples of such practices. Injection of large volumes of waste waters produced during hydrocarbon recovery into the Paleozoic Arbuckle Formation of Oklahoma and Kansas resulted in significantly higher levels of seismicity (e.g., Ellsworth et al., 2015; Keranen et al., 2014; Walsh III & Zoback, 2015; Weingarten et al., 2015) within the underlying Proterozoic crystalline basement with depths ranging from 2 km to 8 km (Kolawole et al., 2019). Sequestration of supercritical CO_2 into the late Cambrian Mount Simon Formation sandstones in Illinois, too, has induced small magnitude seismicity in the basement (Bauer et al., 2016; Goertz-Allmann et al., 2017) although this appears locally to depend on the presence of low permeability barriers (Bondarenko et al., 2021; Williams-Stroud et al., 2020). CO_2 injection to the Basal Cambrian sandstone in NE Alberta has also led to minor levels of seismicity up to 2.5 km depths within the craton beneath the Quest CCS project (Harvey et al., 2021) while in contrast as in 2018 no detectable seismicity had yet appeared from injection to the Cambrian Deadwood Formation clastics at the Aquistore project in the Williston Basin (Stork et al., 2018). The deepest porous formations, too, contain the most heat energy making them attractive geothermal reservoirs (Jordan et al., 2020; Moeck et al., 2009; Weides et al., 2014) with the same basal Deadwood Formation of the Williston Basin currently being commercially developed for combined electrical generation and direct heat (Marcia & Scott, 2021).

In these and other cases, although there may be a reasonable understanding of quantitative stress conditions in the explored sedimentary veneers, knowledge of the quantitative state of stress within the basement itself generally remains unknown. This lack of knowledge, too, affects the capacity to extrapolate stress magnitudes, directions, and even expected faulting regimes into the metamorphic cratonic basement adversely affecting our ability to assess risk (e.g., Zoback & Gorelick, 2012). Indeed, near the study borehole, regional geothermal assessments of the oldest Paleozoic sediments (Ardakani & Schmitt, 2016) and even deep into the craton itself (Droessler & de Pencier, 2020) have recently been carried out, and these developments further motivate the need to understand the crustal stress in the area. Development of preferential flow paths along planes of weakness in such foliated rock masses will be important to engineered geothermal systems (e.g., Guglielmi et al., 2021).

Additionally, given that in many places "young" sediments were passively deposited on much older igneous and metamorphic surfaces eroded at the Great Unconformity, one might even question the degree to which stresses couple between the Phanerozoic platforms and the Precambrian basements. In the Western Canada Sedimentary Basin (WCSB) the stress direction indicators were obtained from geophysical logs exclusively in the sedimentary Phanerozoic platform (Figure 1). The uniformity of the NE-SW azimuth of the greatest horizontal compression S_H, its general geometric relationship normal to the eastern edge of the Cordilleran Deformation Front (CDF) and parallel to the modern plate motion all suggest that the sediments, and presumably the underlying craton, are coupled mechanically to the lithospheric motion (Bell & Gough, 1979; Fordjor et al., 1983; Reiter et al., 2014). Coupling of the craton to the sediments might also be complicated by the thick Devonian Prairie Evaporites (Grobe, 2000), for example, decoupling of stress regimes has been documented across salt deposits in the North German Basin (Röckel & Lempp, 2003). However, this coupling has not been confirmed directly by measurements into the crystalline craton.

Here, we provide a rare glimpse into the stress state within the metamorphic craton beneath the sedimentary platform using logging data obtained from a deep borehole of opportunity. We first review stress state studies from boreholes in cratonic and comparable crystalline terranes. We then detail the aspects of the geology and the rather unique completion of this borehole and present an extensive series of geophysical and image logs obtained for the purposes of geothermal assessments. We are not aware of any other studies in which this range of complementary instruments has been used in a foliated metamorphic craton. Interpretations of borehole failure features are not so straightforward as the orientations of the stress indicators vary over different sections of the borehole, but the interpretation considering the rock texture and strength anisotropy constrained from both image and dipole shear sonic logs does indicate that stress directions are consistent with those observed in the overlying Phanerozoic cover. Based on this analysis, we are further able to provide some quantitative constraints on the stress magnitudes and expected faulting environment at depth. Finally, we comment on the relationships of stress directions at depth in the craton with those expected from indicators in the overlying platform at this locale and the implications of this study for interpreting stress related data within anisotropic cratonic rock masses.

2. Background

2.1 Prior Studies of Crustal Stress in Cratons and Other Crystalline Terranes

Although stresses related in the craton remain sparse, there are several results from the deep drillings into the craton that have still influenced general understanding of stress conditions in the earth. Of these, the Kola Superdeep Well, drilled to 12.2 km in the Fennoscandian Shield remains the deepest borehole yet drilled. Caliper logs indicated variable amounts of borehole enlargement with extensive core discing but there was insufficient information for quantitative stress analysis. However, although stresses were estimated variously using tectonic modelling (Savchenko & Kozyrev, 2003) or the perfect lateral confinement assumption that employs Poisson's ratio (Kozlovsky, 1987), it is not clear quantitatively how stresses are distributed along this borehole.

Studies in deep boreholes in relatively undeformed cratonic rock remain quite rare, however. Haimson (1978) described stress magnitude determinations to 5.3 km in Precambrian rocks in a deep borehole drilled into the center of the Michigan Basin. Haimson and Doe (1983) found a compressional stress state using hydraulic fracturing to 1.6 km in Precambrian granite in northern Illinois. In Finland, repeated image logs of the Outokumpu borehole, drilled into the Paleoproterozoic Fennoscandian Shield to 2.5 km depth, revealed below 1.8 km breakout and drilling induced tensile fracture orientations, indicating a maximum N-S principal compression (Ask et al., 2016) with more detailed interpretations in progress that employ rock strength (Pierdominici & Ask, 2021). Stork et al. (2018) interpreted clear BOs below 3.3 km covering a short section of Precambrian basement in the Williston Basin, Saskatchewan, with the indicated maximum compression azimuth α_H agreeing with those found in overlying sediments.

Stresses have been also studied in boreholes drilled into sections of Precambrian cratons disrupted by Phanerozoic impact events or more recent tectonics. A number of studies have focused on estimation of the stress states from deep (~7km) Gravberg-1 and Stenberg-1 boreholes drilled into the Devonian Siljan Impact structure (e.g., Juhlin et al., 2012) in the Fennoscandian Shield. Some of these studies exploited the variations in BO azimuths obtained from caliper logs through deviated sections (Qian & Pedersen, 1991; Zajac & Stock, 1997) or supplemented with transient pressure tests (Lund & Zoback, 1999). Huber et al. (1997) interpreted ultrasonic image logs to 4.1 km depth in the Vorotilov borehole drilled in the center of the Mesozoic Puchezh-Katunki Impact Structure lying in the East European Platform. Although they observed mostly consistent orientations for borehole breakouts, this indicator varied by as much as 90° over certain depth sections, which did not appear to correlate with any obvious variations in lithology or physical properties. Most recently, Goswami et al., (2020) analyzed image logs through a nearly 1.8 km of Neoarchean Dharwar craton granites and gneisses underlying a 1.2 km thick package of Cretaceous Deccan basalts. These rocks, however, appear faulted and fractured possibly from the rifting of the Indian subcontinent from the Seychelles and the subsequent Deccan volcanism; and here too BO and DITF directions indicate α_H is generally consistent with the focal mechanisms for local seismicity, although these directions deviate also by as much as 90° in some sections. These shifts in azimuth make the face value interpretations of breakout directions problematic.

There are other projects, too, drilled into more recent crystalline formations that are not formally cratonic but still important to mention. These include the 9.1 km KTB into imbricated metamorphic sections of the Paleozoic Variscan Orogeny in Bavaria (Emmermann & Lauterjung, 1997) from which extensive studies of stresses were made using both image log data (Brudy et al., 1997; Brudy & Zoback, 1999) and pressure tests (Zoback & Harjes, 1997), the COSC-1 borehole into the Paleozoic Scandinavian Caledonides (Wenning et al., 2017), and deeper geothermal studies into crystalline rocks at depth in the Rhine Graben (Azzola et al., 2019; Bérard & Cornet, 2003; Valley & Evans, 2019).

Although not universal, one recurring theme that appears in many of the above studies is that BO azimuths often change along a given borehole. Even though the underlying assumptions employing the Kirsch (1898) equations are widely used in the literature, it has long been known that the drilling induced failure pattern may not reflect true far-field stresses and is complicated by deviations of the borehole from a principal stress direction (Mastin, 1988), geological discontinuities (Lin et al., 2007; Sahara et al., 2014; Shamir & Zoback, 1992; Yale, 2003; Zakharova & Goldberg, 2014), contrasting mechanical properties in different lithology (Agheshlui & Matthai, 2017; Pham et al., 2020), and rock strength anisotropy in the layered sediment or foliated crystalline basement (Setiawan & Zimmerman, 2018; Vernik & Zoback, 1989; W. Wang et al., 2022). Analyses based on the Kirsch (1898) equations have led to interpretations of variable stress states between the sediment and basement, such as a ~30° change in the S_H orientation in Basel and Rittershoffen (Azzola et al., 2019), and a stress state change from normal faulting stress regime in the sediment to strike/thrust faulting stress regime in the basement in Songliao Basin, China (B. Wang et al., 2020).

2.2 Regional Geology and Crustal Stress

The simplified map of Figure 1 shows both shield and platform of a western portion of the North American Craton bounded to the west by allochthonous Intermontane Belt accreted in the early Jurassic. In Figure 1, the craton is presumed to extend as far west as preserved sedimentary rocks are present (Wright et al., 1994). However, the zone from this edge to the limit of Cordilleran Deformation Front (CDF) includes the foothills and mountains of the Canadian Rocky Mountain ranges and the major fault system of the Rocky Mountain trench is highly disrupted, but despite this surface deformation the location of the western edge of the craton itself remains a topic of discussion (Y. Chen et al., 2019; McMechan et al., 2020). The portion of the platform to the east of the CDF hosts a foreland basin formed by flexure of the lithosphere due to late Jurassic to Eocene crustal thickening from collision of allochthonous terranes to western North America. The thickened crust sourced much of the Mesozoic and early Cenozoic sediments deposited in the resulting basin upon the gently bent Paleozoic sediment column. The Phanerozoic sediments lie nonconformally along the Great Unconformity (Peters & Gaines, 2012). The thickness of this sediment wedge ranges from more than 5 km in the west and vanishes 600 km or more to the NE at the exposed Canadian Shield (Price, 1994). The craton in this area is a complex assemblage of Archean and Proterozoic terranes bisected by several Precambrian shear zones (Ardakani & Schmitt, 2016; Burwash et al., 1994; Ross et al., 1991), the complications of which are beyond the necessary scope here.

The dearth of crustal stress indicators over the bulk of the map of Figure 1 is readily apparent. The seismicity lies almost exclusively SW of a zone that begins near the CDF. Notable clusters of seismicity, all of which are related to anthropogenic hydrocarbon extraction or potash mining activities, appear in NE British Columbia, just west of the CDF at 52.5°N in Alberta, and at about 51°N in easternmost Saskatchewan. More detailed discussions of the regional patterns of observed seismicity and possible structural controls may be found in Stork et al. (2018) and Shen et al. (2021), but to reiterate, no significant natural seismicity has historically or instrumentally been detected near the Hunt Well site.

Similarly, the bulk of the stress direction indicators displayed in Figure 1 were obtained from deep boreholes drilled into the thick Phanerozoic sediment packages in the vicinity of the CDF. Some of these results were from the earliest interpretation of borehole elongations in the original developments that linked borehole elongation azimuths to principal stress directions (Bell &

Gough, 1979). Reiter et al. (2014) updated the Canadian database on crustal stress and developed an averaging scheme that shows the NE-SW compression generally near N45°E. Shen et al. (2019, 2021) confirmed these observations from recently completed analyses of borehole image logs, but these data, too, remain concentrated in western Alberta near the CDF. One exception to this comes from extensive DITFs observed in multiple boreholes within Devonian carbonates at a site approximately 100 km SW of the Hunt Well (indicated by the solid blue circle in Figure 1), which agree with the regional NE-SW compression (Morin, 2017).

3. The Hunt Well

3.1 Geology of the Hunt Well

The Hunt well is located immediately west of the city of Fort McMurray (56°45'N, 111°33'W) penetrating 541m of Phanerozoic sediments before intersecting the metamorphic basement. Drilling of the well was finally completed in 2003. To the best of our knowledge, after 2003, aside from proprietary temperature loggings carried out in 2008 by an industrial consortium, the borehole remained untouched until 2010 where it was accessed for a number of studies related to the deeper geothermal potential commencing with a temperature log (Majorowicz et al., 2014), geological analyses of the existing cores (Walsh, 2013), slimline geophysical loggings (Chan, 2013) and a vertical seismic profiling (VSP) to ~1900 m, and reprocessing and collection of new high resolution 2D seismic profiles adjacent to the site (Chan & Schmitt, 2015b). Chan (2013) made some exploratory calculations of the vertical compression S_V using proprietary density logs. From a 2003 proprietary high-resolution electric image log (Schlumberger FMI™), Chan (2013) also made interpretations of possible fractures, BOs, and DITFs although the quality of this log was impaired by the high resistivity of the crystalline rocks. The results reported here, however, are primarily based on completely new data collected in late 2013 including ultrasonic image logs (Schlumberger UBI™) that allow for more detailed assessments of borehole cross-sectional geometry in conjunction, and dipole shear-wave loggings (Schlumberger DSI™) that allow for assessments of anisotropy local to the borehole.

The simplified lithology and final engineering configuration of the Hunt Well were constructed from drilling reports and the earliest geophysical logs from 2003 (Figure 2a), which show that the borehole transects from the surface 94 m of Mesozoic clastics and 430.3 m of Paleozoic carbonates, evaporites, and clastics reaching to the Great Unconformity at 541.3 m. Below this, the borehole intersects meta-igneous rocks of the Proterozoic Taltson Magmatic Zone (TMZ) that is believed to be intrusive complexes of either a plate-boundary or plate-interior origin (e.g., Chacko et al., 2000; McNicoll et al., 2000). Only limited cores from this section were retrieved from depths of 1656.5-1657.8 m and 2347.5-2364.3 m, which Walsh (2013) characterized, respectively, as a hercynite biotite garnet gneiss (Figure 2b) and an othopyroxene granite (Figure 2c) with the latter sample assigned an age of 2400 Ma. The foliations dip steeply in both samples, but the cores are unoriented.

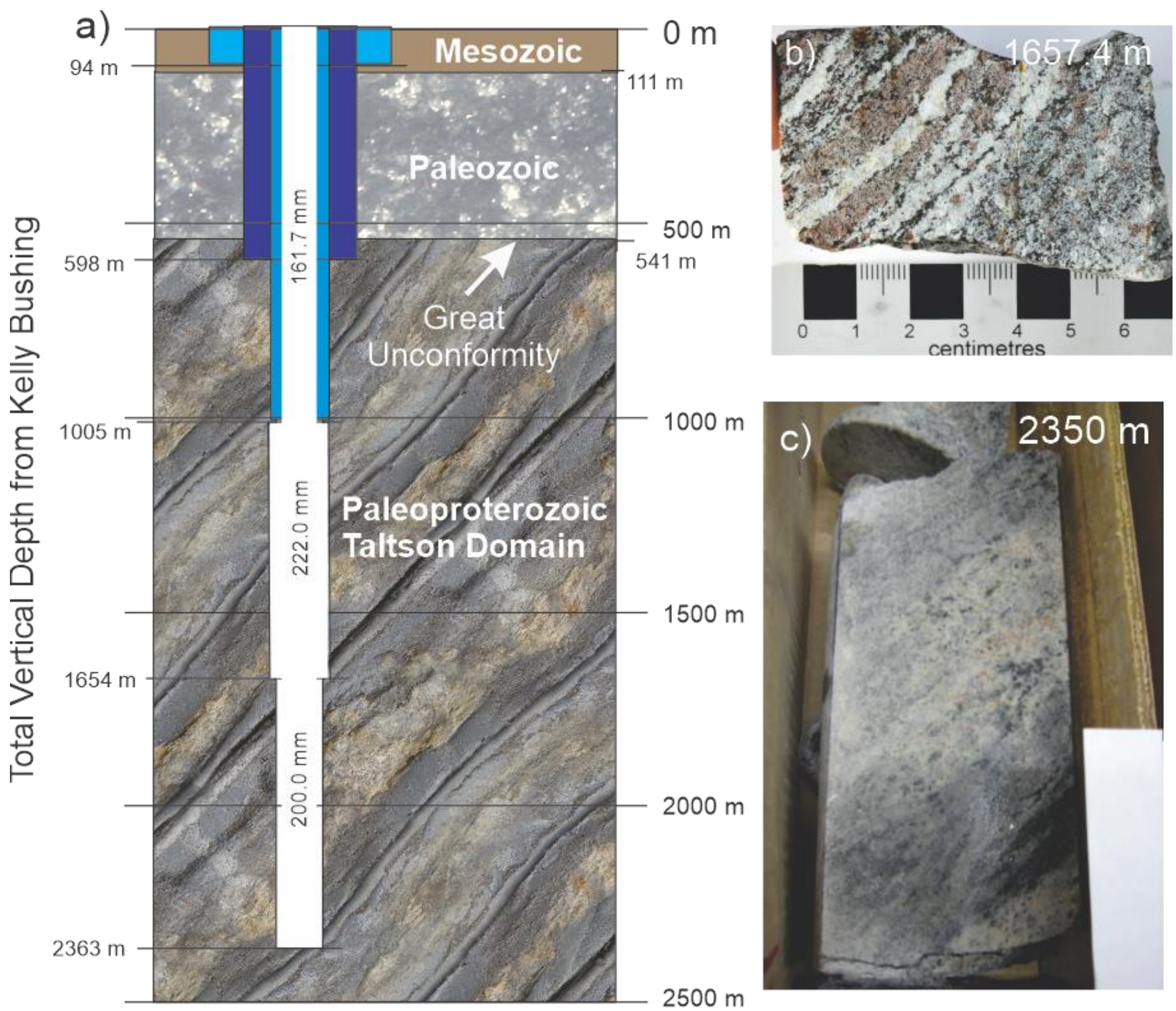

Figure 2. a) final borehole configuration showing the extent of casings (shades of blue) and the open hole with nominal diameters in the center and depths to bottom of each section on the left side. Depths to the base of the Mesozoic and Paleozoic sedimentary sections are shown on right hand side. b) biotite garnet gneiss hand sample from 1657.4 m. c) orthopyroxene metagranite core section from 2350 m. Core photos were from Figure 2-2 of Walsh (2013) used with permission of the author.

Reprocessed 2D seismic profiles, too, reveal reflectors within the basement with apparent dips to the east (Chan, 2013; Chan & Schmitt, 2015b), which are possibly related to the metamorphic textures. Following procedures developed in Schijns et al. (2012) using walk-a-way VSP geometries, Chan (2013) detected the P-wave anisotropy of about 17% over the interval from 797 m to 1777 m interpreted to be caused by the metamorphic texturing of the formation. Thin sections of the rock from the deeper depth show elongated quartz and feldspar bands, indicating the presence of foliation (Chan & Schmitt, 2015a). Laboratory pulse-transmission measurements under the high effective confining pressure on a multi-faceted prism, which was machined in alignment with the foliation on the material from the 2350 m core, display P- and S-wave anisotropies, respectively, of nearly 20% and 10% (Chan & Schmitt, 2015a). The texture of this sample suggest it has transversely isotropic (TI) symmetry, and under this presumption a full set of TI stiffness matrix was measured. The metamorphic textures and anisotropic strength are important to later analyses.

Although not shown, it is worth mentioning that the temperatures along the borehole are modest with peaking at only 47.5°C at 2363 m corresponding to a low average geothermal gradient of 20.4°C/km. The borehole is close to vertical with a maximum deviation less than 7° which is accounted for in later textural analysis.

To the best of our knowledge, no systematic analysis of the variations in the metamorphic lithologies was carried out during drilling, and only the geophysical logs might provide additional information (for convenience, brief descriptions of logging instruments are provided in Text S2). In Figure 3, the natural γ radiation log (GR) used for the depth referencing generally indicates high, but not anomalous, levels of natural radioactivity for granitic compositions. The photoelectric factor P_e (PEFZ) provides a semi-qualitative measure of the elemental composition in the rocks, and this remains relatively uniform within the range of 4-6 barns/electron that likely corresponds to the concentration of hornblende with elevated PEFZ values, but this log does not indicate any significant change in the lithology along the borehole. PEFZ tracks closely the γ-γ mass density ρ (RHOZ), further suggesting that the relatively minor variations seen are likely due to the variations in the Fe content, likely due to changing concentrations of hornblende.

Figure 3 shows additional geophysical logs relevant to the mechanical properties from 2013 including monopole compressional V_P and shear V_S wave speeds, and subsequently calculated

Young's E (YMG) and shear μ (SMG) moduli and Poisson's ratio v (PR) using well known expressions (see Table S1). V_S remains within a small range near 3500 m/s while V_P increases in a narrow range from 5750 m/s to 6000 m/s with minor excursions up to 6500 m/s. These are all well within expected ranges for rocks of granitic composition (e.g., Christensen & Stanley, 2003). These logs, and those derived from them (See Table S1), do not show any strong variations in the apparent calculated isotropic mechanical properties in agreement with the ρ and P_e.

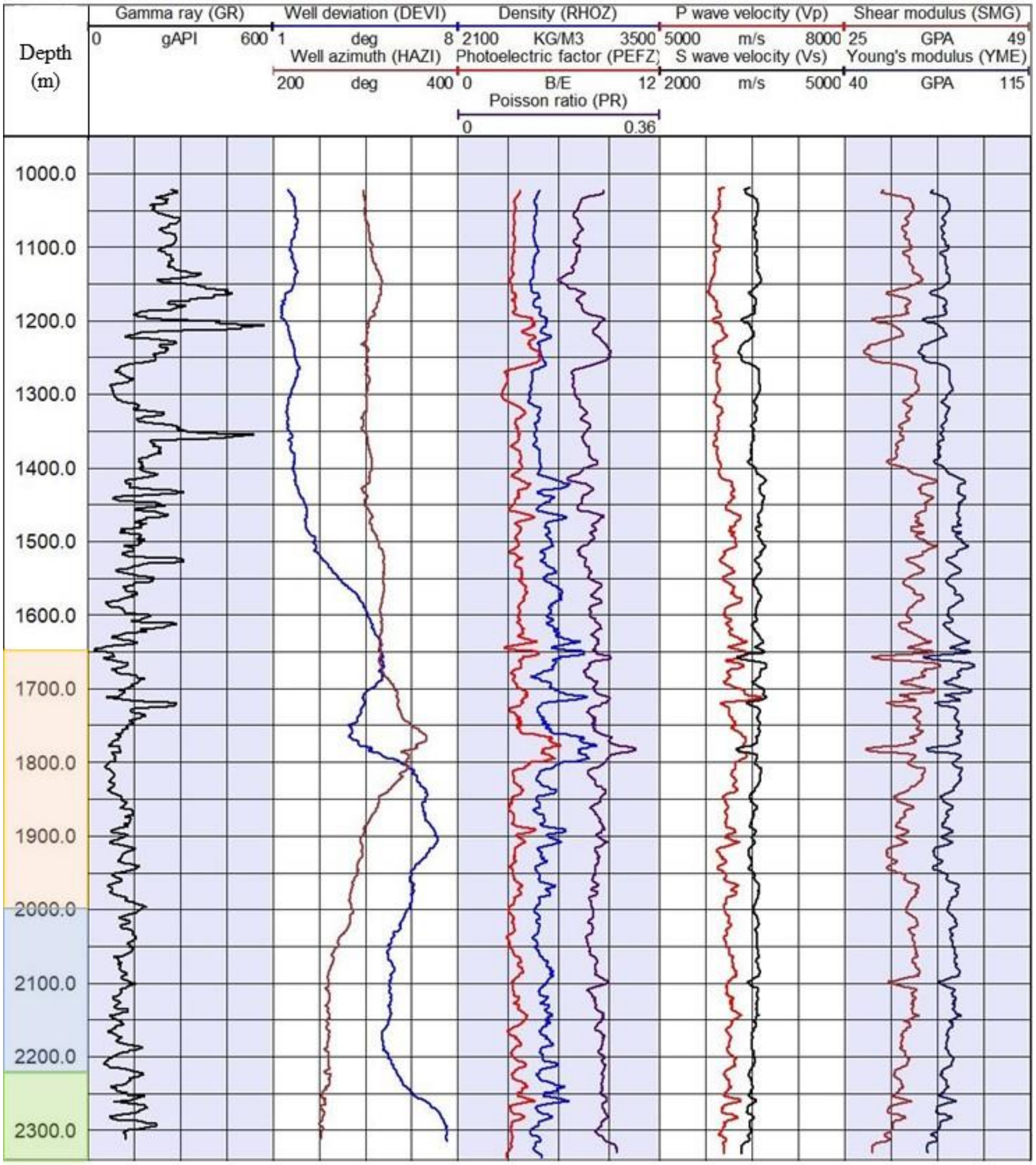

Figure 3. Geophysical logs filtered with a moving average of 50 points. The depth axis is color-coded to represent the three depth intervals where the breakout orientation observed in the study is consistent but varies among different intervals. Wellbore deviation and azimuth are shown in the trace 2, indicating the wellbore is nearly vertical. Physical properties such as density in the trace 3 and elastic moduli in the trace 5 do not show obvious mechanical differences along the wellbore depth. To ensure all geophysical logs are referenced to the same depth acquired in each operation, depth matching was performed based on Gamma Ray (GR) logs referencing to the GR log acquired in the 2013 Ultrasonic Borehole Imager (UBI) run. Summaries of physical principles and operation of the various logging instruments are provided in Text S2.

3.2 Completion of the Hunt Well

The Hunt Well was drilled in two sessions first to 1649.0 m in 1994 with the final completion to 2363.3 m delayed to 2003. The details of this completion are highly unique and cannot be ignored in the geomechanical interpretations. A detailed timeline of the history of the borehole, updated from Chan (2013), is provided in Table S2 but key activities germane to the analyses are summarized here in Table 1.

Table 1 Well History – Abbreviated and Updated from Chan (2013)

Date	Event	Important activities or observations
1994	Initial Drilling Session	• Drilling to 1649.0 m • Geophysical logging to 1649.0 m (FMI-1994)[1] • Casing to 598.2 m
2002-3	Deepening of Borehole	• Open hole straddle packer tests at 873.0 m and 1370.0 m • Continue drilling to 2363.3 m • Installation of the cemented casing to 1005.7 m • Geophysical logging from 1600 to 2351.0 m (FMI-2003)[1] • Installation of the production tubing • Repeated bailing of the well until dry
2010-1	Geothermal Temperature Logging	• Re-entry for temperature logging (Majorowicz et al., 2014) • Borehole air-filled until 2192.0 m • Borehole refilled with water for temperature loggings
2011	Slimline Logging	• Removal of the tubing to allow for the open hole logging • Geophysical logging[2] from 1000 to 1875.0 m (Dip-2011) (Chan, 2013) and VSP (Chan & Schmitt, 2015b) • Partial blockage encountered at 1360.0 m
2013	Commercial Logging	• Removal of blockage • Commercial geophysical logging[1] with ultrasonic image logs and dipole shear sonic wave anisotropy logs. These data are reported here for the first time.

Note. [1.] Commercial logging company Schlumberger. [2.] Operational Support Group of the International Continental Drilling Program.

There are two major points to be summarized from Table 1. First, repeated open-hole logs providing caliper measures of the borehole diameter or elongation were acquired through various sections of the borehole in 1994, 2003, 2011, and 2013. These provide a rare opportunity to examine changes in the borehole with time. Second, although the logging operations all occurred when the borehole was filled with drilling fluid, much of the extent of the borehole below the cemented casing at 1005.7 m remained air-filled for nearly 8 years, from 2003 when the borehole was bailed dry to late 2010 when it had to be filled with water to allow for temperature measurements. This fact indicates both low storativity and permeability along a section of craton nearly 1.4 km in extent, and this is of interest by itself but beyond the scope of this study. From the geomechanical perspective here, however, this means that the stress concentrations near the borehole experienced the complete loss of the radial load from the wellbore fluid pressure P_w once the borehole had been completely drained; and this change is reflected in differences in the extent of BOs between the last observations in 2003 and those of 2011 and 2013.

4. Methods

Oriented calipers, high-resolution electrical image (FMI™) and ultrasonic image (UBI™) logs, and flexural mode dipole shear sonic (DSI™) logs with vintages from 1994 to 2013 are used here to identify borehole elongation magnitudes and directions, foliation plane orientations, and flexural wave fast and slow directions towards an integrated stress analysis. These methods were described in detail elsewhere (Schmitt et al., 2012; Zoback et al., 2003). The differing borehole instruments and the protocols used in the interpretations are briefly described here with more details available in Text S2. The commercially available program WellCAD™ 5.3 (Advanced Logic Technology, Luxembourg) was used for analysis.

4.1 Underlying Principles

Briefly but to avoid ambiguity, we presume an Andersonian (1951) state of stress with one vertically aligned principal compression S_V and maximum and minimum horizontal compressions S_H and S_h, respectively, with S_H directed at azimuth α_H (Figure 4) measured from geographic north following Heidbach et al. (2018). Compressive stresses, pore fluid pressures, mud pressures, and rock strengths have positive signs and tensile stresses have negative signs. Please refer to Text S2 for analytical Kirsch equations (1898) to conventionally interpret the stress field around the wellbore.

The rock surrounding the borehole will fail in compression with BOs or in tension with DITFs if the most and least concentrated hoop stresses exceed the rock's compressive and tensile strengths, respectively (Figure 4a). In isotropic rock masses, the greatest and least compressive concentrated hoop (circumferential) stresses are at azimuths aligning, respectively, with S_h and S_H for vertical wells (Figure 4c). Without the mud pressure P_w to sustain the wellbore stability, the magnitude of the hoop stress becomes larger, increasing the potential of wellbore instability. The mud pressure cannot be too large as well to hydraulically fracture the rock formation. Interpreting BOs and DITFs from geophysical logs will provide information on the in-situ stress state unambiguously if the rock formation is linear elastic, isotropic and free of localized disturbance. The width of the BOs, too, are then often used as an additional constraint on the stress magnitudes. Most analyses of BOs rely almost exclusively on this isotropic paradigm.

However, various factors ranging from metamorphic textures to oriented fracture sets cause both the elasticity and strength of rock masses to be anisotropic. Relative to the isotropic case, elastic anisotropy perturbs the near-borehole stress concentration (see review in Li et al., 2019) and possibly perturbs the directions and magnitudes of gravity-induced horizontal compression of the rock mass itself (Amadei & Pan, 1992). Anisotropic strength, and preferentially oriented planes of weakness due to foliations or beddings, further complicate the analysis of breakouts. Based on Jaeger (1960) single plane of weakness theory, the uniaxial compressive strength of the rock depends on the angle between the normal of weak planes and the applied stress. If they are suitably oriented, the weak plane will slip. Vernik and Zoback (1990) found that there are four sectors around the wellbore that satisfy the failure in the weakness plane. Lee et al. (2012, 2013) indicated that considering the anisotropic rock strength, the breakout width becomes larger, and the breakout orientation rotates. By unwrapping the wellbore around the N direction, in the study, we propose that the crescent moon shape of failures (red region) at the dip direction due to the weak plane slippage (Figure 4d) could be observed. Therefore, the resulting breakout failure due to the weak plane does not follow the S_h direction (Figure 4b), rendering the stress interpretation from image logs erroneous if we solely assume rock isotropy.

The analyses of breakout observations here take into consideration of both the elastic anisotropy of the rock mass and the presence of the plane of weakness upon which slip may occur using a recently developed program ***EASAfail*** . ***EASAfail*** first calculates the stress distribution around the elastic anisotropic rock formation, and then determines the rock failure by taking two sets of rock strength information, one for the intact rock matrix and the other for the weak plane, to account for the strength anisotropy. The algorithm can use a variety of failure models, but here we assume the simple Mohr-Coulomb frictional criterion (e.g., Jaeger et al., 2007) that governs both shear failure of the intact rock and slip on the plane of weakness according to

$$|\tau| > C_i + (\sigma_n - P_P)\mu_i \tag{1}$$

where τ and σ_n are the shear and normal tractions resolved onto the ultimate plane of failure, P_P is the pore fluid pressure, μ_i (= $\tan\phi_i$) is the static coefficient of friction, and C_i is the cohesive strength for either the intact rock ($i = o$) or the weak plane ($i = w$).

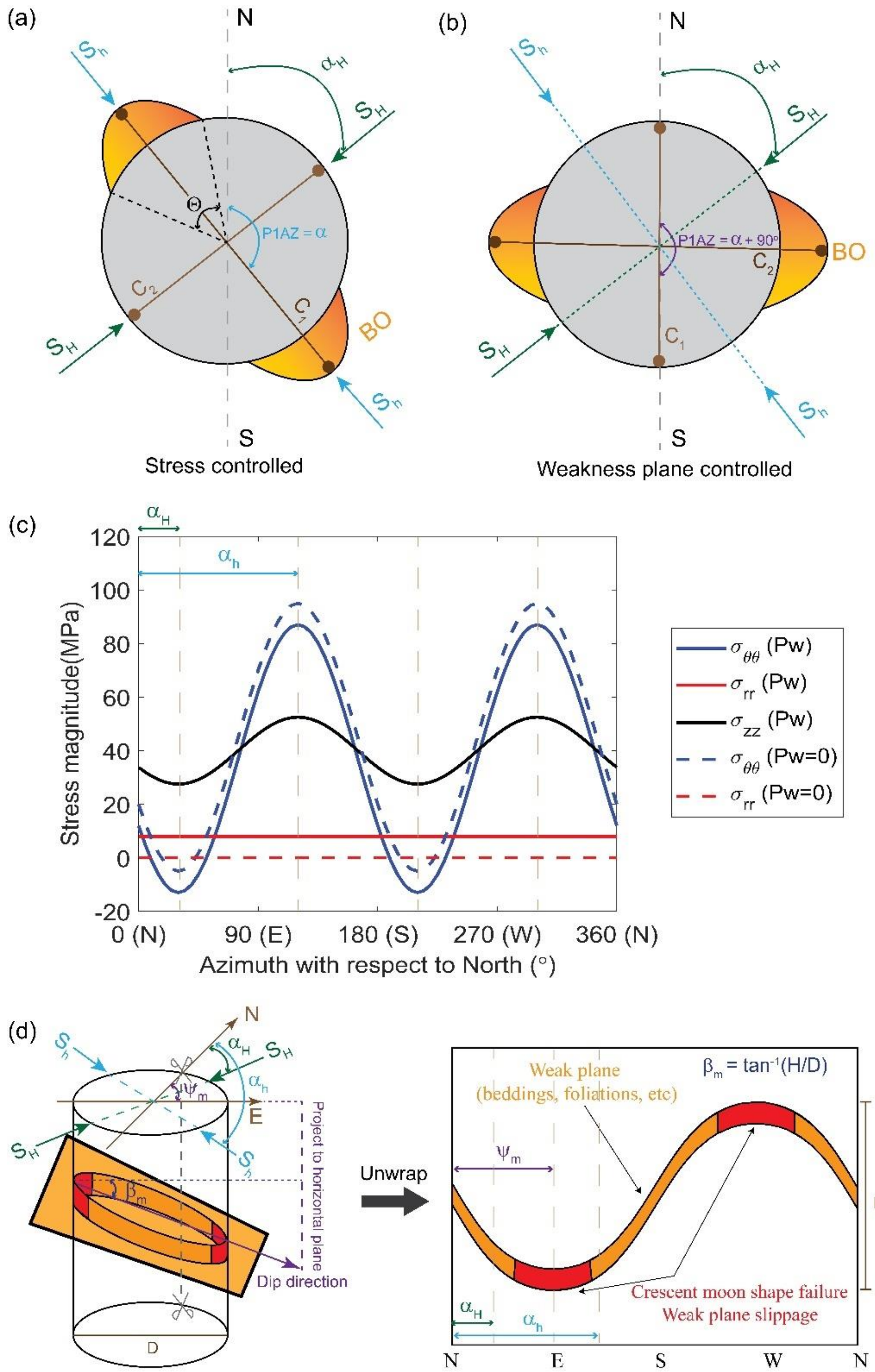

Figure 4. Breakout failure patterns in the intact rock matrix and in the weak plane. (a) Plan view down borehole illustrating azimuths of the normal shear failure induced BO and directions of caliper arms. α and Θ represent the breakout azimuth and width respectively. *C1* and *C2* are two orthogonal caliper measurements. *P1AZ* is the pad 1 azimuth. If *C1* is trapped in the BO, *P1AZ* = α. (b) Plan view down borehole illustrating azimuths of the weak plane slip induced BO and caliper arms. If *C2* is trapped in the BO, *P1AZ* = α + 90°. (c) Stress concentration versus azimuth based on Eq. (S2-S4). σ_{rr}, $\sigma_{\theta\theta}$ and σ_{zz} are the Terzaghi effective radial, hoop (circumferential), and axial stresses. α_H and α_h are the azimuth of the maximum and minimum horizontal stresses respectively.

For illustration, S_H, S_h, S_v, and P_p are set at 35 MPa, 10 MPa, 40 MPa and 0MPa respectively. Solid and dashed lines represent the cases for the mud pressure (P_w) equal to 8 MPa and 0 MPa respectively. Poisson's ratio equals to 0.25. (d) 3D view of the weak plane slippage failure. The orange plane with ribbon represents the weak plane with a certain aperture. Failures at the dip direction will form a crescent moon shape (red region). ψ_m and β_m are the strike and dip angles of the weak plane. *D* is the diameter of the wellbore and *H* is the amplitude of the sinusoid (peak-to-trough).

4.2 Caliper Logs

The oriented caliper tools have four arms that expand to the borehole wall to provide two orthogonally direct measurements of the borehole diameter, referred to here as *C1* and *C2*, along with the azimuth of the *C1* (*P1AZ*). Here, five sets of oriented caliper logs are available from consecutive logging operations of the Hunt Well using a variety of instruments and it is important to note that the difference in their configurations might affect the values of *C1* and *C2*. The *FMI-1994* and *FMI-2003* diameters were from the extension of the arms for the opened electrode pads in the FMI^{TM} tool. The *DIP-2011* was provided from a slim-hole 4-arm dipmeter tool (DIP tool, Operational Support Group, GFZ), limited to a maximum diameter of only 250 mm. The *PPC-2013* diameters were provided from the Powered Positioning Caliper (Schlumberger PPC^{TM}) which was used for centralization during each of the ultrasonic imaging and dipole sonic log runs. See Text S2 for additional technical details on these instruments and breakout interpretation criteria.

4.3 Image Logs

Two different types of imaging logs, electrical image (FMI^{TM}) and ultrasonic image (UBI^{TM}) logs, were used. Interpretations of image logs are based on the physical characteristics of drilling induced failures. In FMI logs, if BOs and DITFs exist, the intrusion of drilling mud into the broken wellbore rocks will lead to a pair of lower resistivity failure zones separated by 180° with BOs being wide and DITFs being narrow. While in UBI logs, the bigger radius caused by the wellbore failure results in a pair of failure zones with smaller amplitude and longer travel time of the reflected echo compared to the original wellbore radius.

Drilling induced features were interpreted in two ways. One was through manually analyzing physical features every 20 cm vertically without overlapping and the breakout azimuth at each 20 cm-depth interval was selected to be the median in the commercial software. The other was through a Matlab-based function ***BOAPFIL*** to automatically detect BO locations that are manifested by the amplitude troughs and radius peaks from analyses of each 360° scan of the transducer (W. Wang & Schmitt, 2020, 2022). Details of the processing of these image data and of the criteria employed in declaring, orienting, and width determination for the BOs in image logs are provided in Text S2.

In addition, obvious sinusoidal features in these image logs, due to planar features such as fractures or foliation planes that intersect the cylindrical borehole, the amplitude and phase of which depend on the borehole diameter, a given plane's strike and dip (Figure 4d), could also be detected. Here, the sinuous patterns in the amplitude image are mostly indicative of the foliations (Massiot et al., 2018) and not fractures as they have no obvious corresponding response in the travel time image (Schmitt, 1993). It is also important to note, particularly in the travel time image of Figure 8, that the breakout azimuths preferentially appear at the peaks and valleys of the sinusoids, suggesting that the metamorphic foliation strongly influences the breakout occurrence.

4.4 Dipole Shear Sonic Logs

The dipole sonic tool (Schlumberger Dipole Shear Sonic Imager – DSI^{TM}) is comprised of one monopole transmitter and two sets of orthogonal dipole transmitter-receiver pairs (S. T. Chen, 1988). This instrument is sensitive to variations in the rock elastic properties around the borehole indicative of either intrinsic material anisotropy (e.g., Boness & Zoback, 2006; Sinha et al., 1994) or stress induced circumferential variations in the elastic formations (e.g., Winkler, 1997). Dispersive flexural wave modes are excited by two orthogonally mounted sets of dipole transmitter-receiver pairs oriented perpendicular to the borehole axis. Processing of the received waveforms allows the fast V_{SF} and the slow V_{SS} shear wave speeds and their polarization azimuths for propagation parallel to the borehole axis to be obtained; and since these are orthogonal to one another, only the fast shear wave polarization azimuth χ_F is often reported. It is important to note that V_{SF} and V_{SS} are the speeds for the lowest frequencies, ostensibly sensing the formation properties outside of the near borehole disturbances, although care may need to be taken in some cases to associate them with corresponding material speeds (He et al., 2010).

These waveforms contain substantial information about the formation (Ellefsen et al., 1991; Sinha et al., 1994) and they are useful to consider the situations that might be encountered in a homogeneous anisotropic rock mass absent of any near borehole stress dependent complications.

Consider the rock mass to be intrinsically transversely isotropic (TI) with a rotational axis of symmetry ζ perpendicular to an isotropic plane. The orientation of this TI material is often designated (Figure 5) by the degree to which ζ deviates from the vertical, which is identically the foliation dip angle β_m, and is called as vertical (VTI) $\beta_m = 0°$, horizontal (HTI) $\beta_m = 90°$, or tilted (TTI) $0° < \beta_m < 90°$ materials.

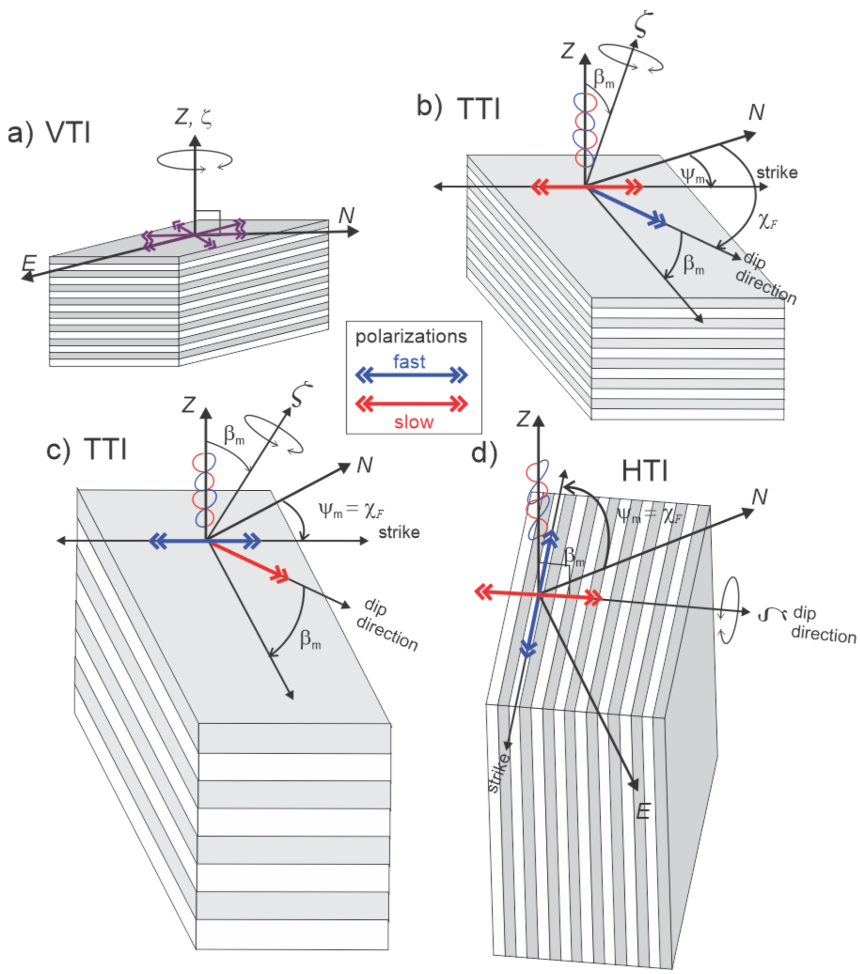

Figure 5. Geometric relationships for: a) vertical transversely isotropic rock mass (VTI) with degenerate polarization directions, b) gently dipping tilted transversely isotropic rock mass (TTI) with the polarizations $V_{SS} \parallel$ strike (ψ_m) and $V_{SF} \parallel$ dip direction ($\psi_m + 90°$), c) steeply dipping TTI rock mass with the polarizations $V_{SS} \parallel$ dip direction ($\psi_m + 90°$) and $V_{SF} \parallel$ strike (ψ_m), and d) horizontally transversely isotropic rock mass (HTI) with the polarizations $V_{SS} \parallel$ dip direction ($\psi_m + 90°$) and $V_{SF} \parallel$ strike (ψ_m). Z, N, and E are the vertical, North, and East directions. ζ is the axis of the rotational symmetry of the TI media. ψ_m, β_m and χ_F are the foliation or weakness plane's strike (as measured clockwise from N), the plane's dip, and the azimuth of the fast polarization angles, respectively.

Generally, in any direction through TI materials, two orthogonally polarized “split” shear waves propagate at different speeds with polarizations either parallel or perpendicular to the foliation plane. The speeds of both polarizations change with the direction the waves propagate through the material which, for the case here, can be referenced with respect to the dip β_m. However, which of these polarizations is the fastest at any given β_m depends on the material elasticity, and consequently χ_F may point either in the dip or the strike directions (Figure 5) with this behavior illustrated for two foliated metamorphic rocks. Figure 6 illustrates the evolution of V_P, V_{SF}, and V_{SS} with the tilt β_m.

i) Through a VTI formation the tool measures $V_{SF} = V_{SS}$ and these equal the speed of a vertically propagating, degenerately horizontally polarized shear waves (Figure 5a). For this case, χ_F is arbitrary as is often observed in stiff shale formations (Ong et al., 2016).

ii) For an HTI medium $V_{SF} > V_{SS}$ (Figure 5d) with these speeds now equaling, respectively, the vertically propagating fast shear wave polarized horizontally parallel to the strike of the foliation plane and the slow shear wave polarized horizontally parallel to the material's rotational symmetry axis (Sinha et al., 1994).

iii) For the TTI case depending on the amount of tilt and the nature of the rock's anisotropy itself, χ_F may be either parallel or perpendicular to the foliation strike as first noted by Ellefsen et al., (1991). Examples of this behavior calculated from measured TI elastic stiffnesses on two metamorphic rocks are shown in Figure 6 only for the purpose of illustrating the switch in fast and slow polarization directions with dip.

The situations here presume that the intrinsic TI anisotropy dominates any stress dependent nonlinear elastic effects in the rapidly varying concentrated stress field near the borehole. Such effects can result in complex patterns of the two flexural wave dispersion curves but as our observed curves to be provided shortly are controlled by the intrinsic anisotropy. We do not overview this aspect here but direct the readers to Text S2 or Schmitt et al. (2012) for additional information.

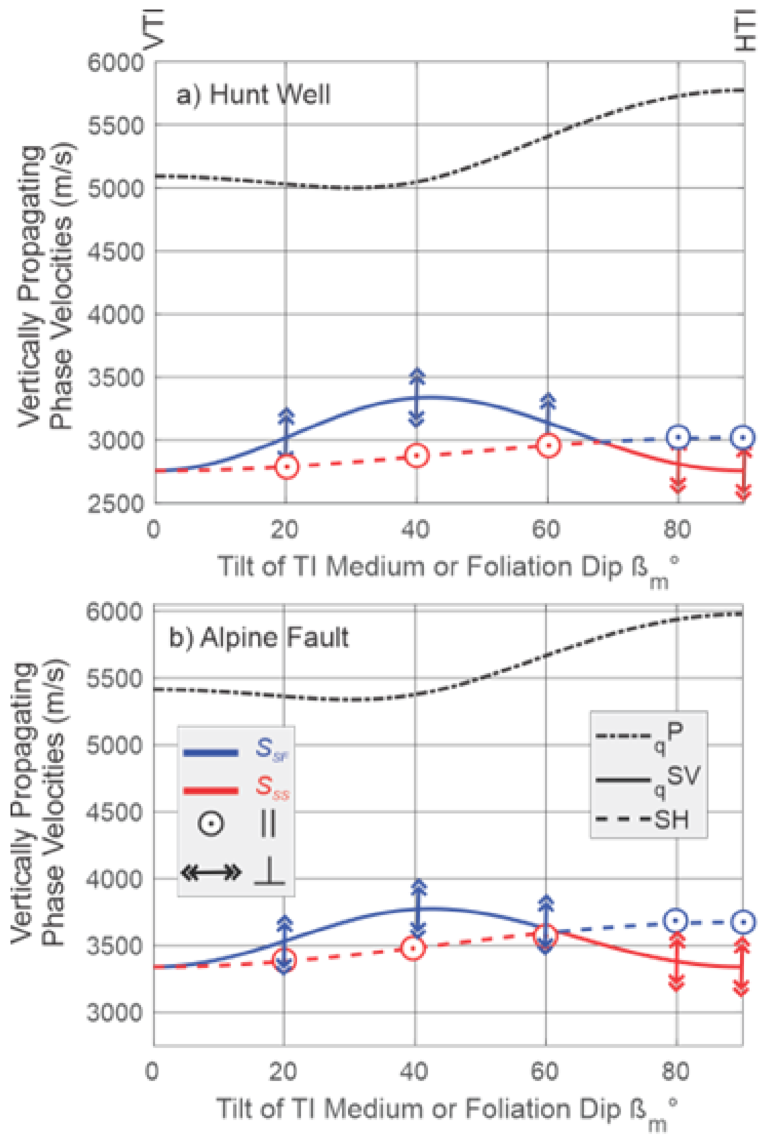

Figure 6. Illustration of the relationships between the variations in the V_P, V_{SV} polarized in the plane perpendicular to the foliation strike as indicated by the double-headed arrow, and V_{SH} polarized parallel to the foliation strike as indicated by the out-of-plane arrow, as observed from a vertical borehole drilled through the foliated TTI rock mass dipping at β_m. The waves speeds were calculated using measured TI stiffnesses for a) the core sample from the Hunt Well with $\delta = -0.30$ (updated from Chan & Schmitt, 2015a) and for comparison on b) a mylonite from the Alpine fault with $\delta = -0.10$ (unpublished data). Blue and red lines represent the fast and slow shear waves, respectively. See Text S3 for additional information.

5. Results

5.1 Caliper Log Observations

The observed *C1* and *C2* caliper diameters (Figure 7) highlight the evolution of breakouts from 1994 to 2013. The first *FMI-1994* caliper radii down to 1659 m display sectors over which $C1 \neq C2$ that may indicate breakouts (Figure 7a). However, in both these and later measurements through this same section, both diameters significantly exceed the bit size; and consequently, they should not formally be interpreted as breakouts as they may likely be washouts or key-seats (Plumb & Hickman, 1985), supported by the ultrasonic image logs described shortly. Further, differences in the radii between *FMI-1994* and *PPC-2013* may also result from the inability of the wide, open FMI pads to fully extend to the rugous borehole wall.

There was little evidence for breakouts from the *FMI-2003* caliper measurements acquired in the freshly drilled section of the borehole below 1659 m depth (Figure 7b) while stronger evidence for breakouts exists in the *Dipmeter-2011 and PPC-2013* (Figure 7cd). More specifically, the *FMI-2003* calipers show the borehole to be largely in gage from 1659 m to 2363 m. In contrast, *PPC-2013* caliper runs (Figure 7d) show numerous segments where the minor axis remains in gage while the length of the major axis is significantly greater, a situation indicative of breakouts (Plumb & Hickman, 1985). One could interpret this as being due to the time dependent breakout development (e.g., Martin et al., 1997). However, it must also be kept in mind that the radial P_w loading of the borehole wall, which normally would assist in stabilizing the borehole, vanished once the borehole was completely bailed dry in 2003 facilitating failure and this correspondingly influences the magnitudes of both the concentrated $\sigma_{\theta\theta}$ and σ_{rr} (Figure 4c).

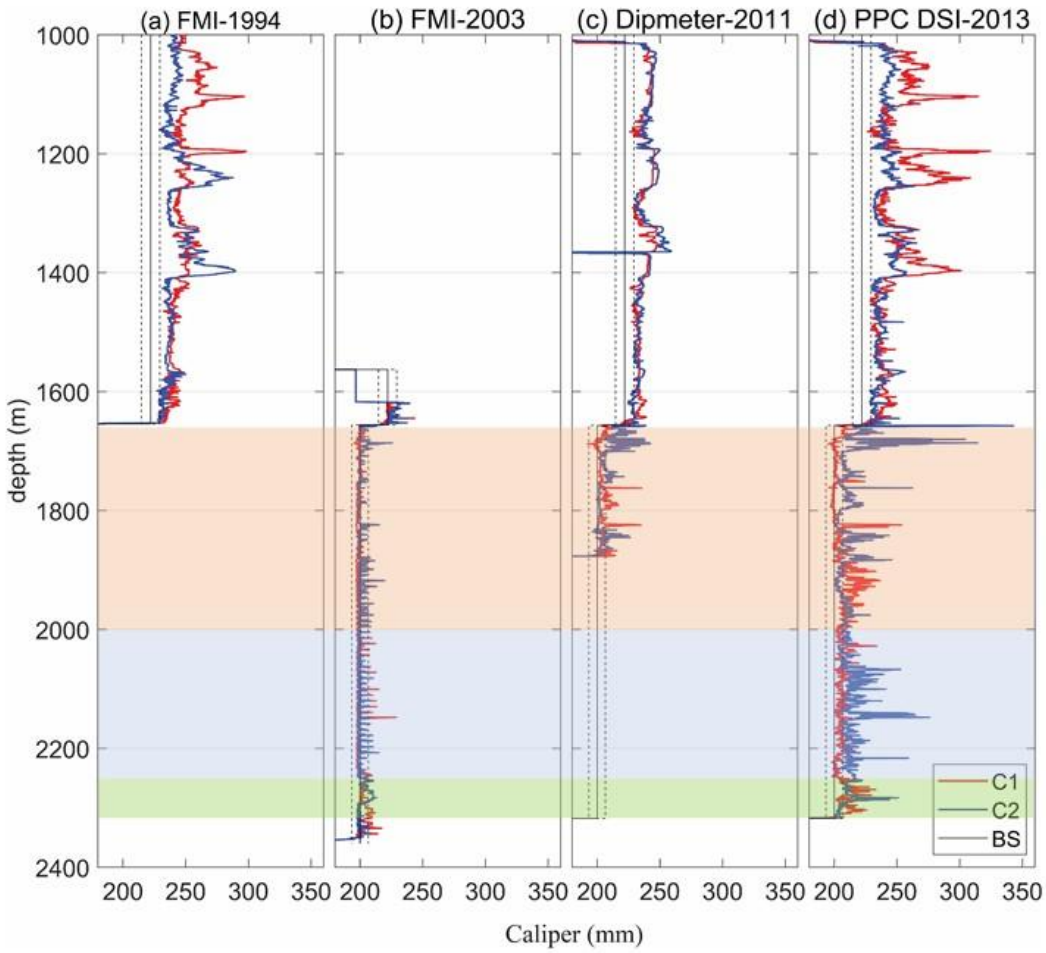

Figure 7. Diameters from oriented 4-arm caliper logs obtained from the *FMI-1994* and *FMI-2003* runs, the *Dipmeter-2011* run, and the *PPC DSI-2013* run indicating the existence of borehole breakouts. The calipers from the *PPC UBI-2013* run are omitted here since they give the similar values as those from the *PPC DSI-2013* run. Red and blue curves represent two orthogonal caliper measurements. The solid and dashed grey curves represent the nominal bit size ± 5%. The maximum diameter allowed for the *Dipmeter-2011* log is 250 mm. Note that the borehole had been emptied of fluid shortly after *FMI-2003* was obtained and the borehole was not refilled until 2010. See Figure S2 for the corresponding P1AZ of each run.

5.2 Image Log Interpretations

5.2.1 Breakout Azimuths and Widths

No clear evidence of drilling induced breakouts was observed in the FMI image logs acquired in 1994 to 1649 m depth or from 1600 to 2351 m in 2003 (Figure 8b), which agrees with the interpretations from the associated caliper measurements (Figure 7). Distinct BOs are also not seen in the 2013 ultrasonic UBI image logs in the upper section despite the large borehole diameters encounter there, again supporting the contention that this zone was damaged by washouts or key seats. In contrast, BOs are common in the ultrasonic images along the lower sections (Figure 8b) and extend a total length of 252 m along the borehole. The occurrence of BOs in the *UBI-2013* images is consistent with changes in the calipers from *FMI-2003* to *PPC-2013* mentioned above (Figure 7). No clear DITFs were observed in either FMI or UBI logs.

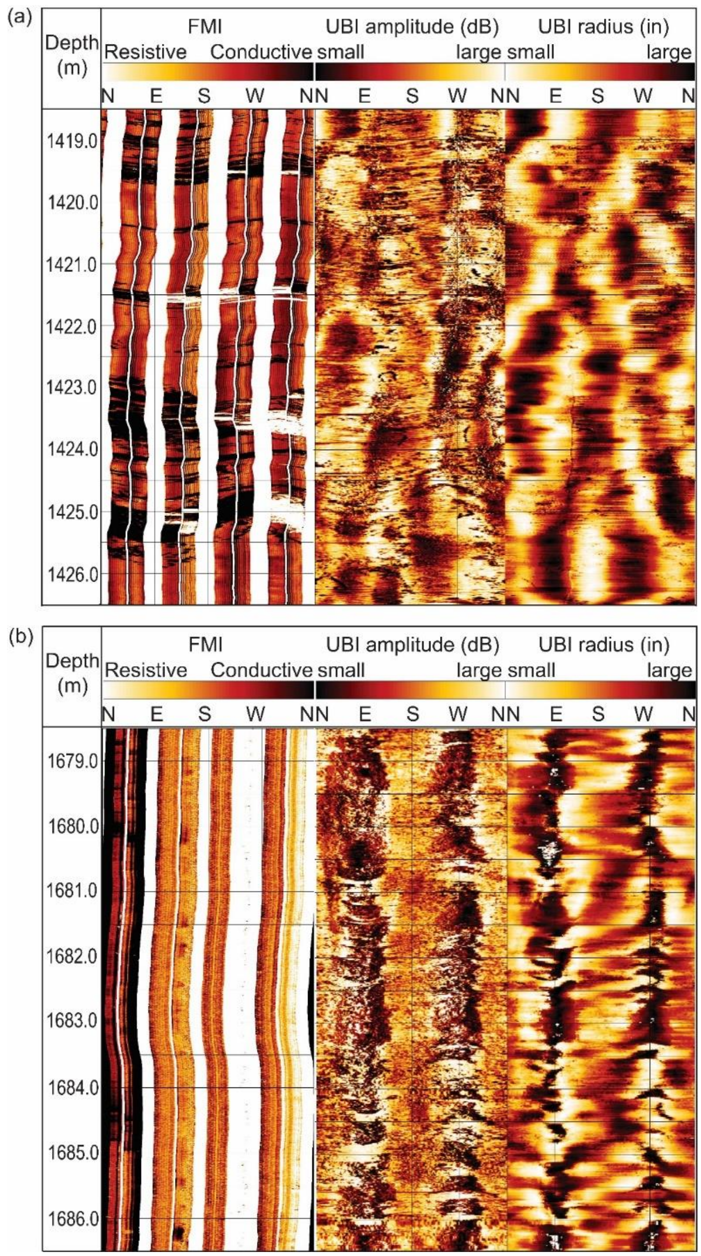

Figure 8. Comparison of image logs. a) *FMI-1994* image (left panel) relative to *UBI-2013* amplitude (center panel) and transit time (right panel) images. The amplitude panel highlights the metamorphic foliations. b) *FMI-2003* image (left panel) relative to *UBI-2013* amplitude (center

panel) and transit time (right panel) images. There is no evidence for breakouts in the FMI image whereas foliation-controlled breakouts (crescent moon shape) are clearly visible in the UBI images.

During interpretations, the azimuths of BOs were identified in ultrasonic images both manually and automatically, and individual selected BOs according to each method are compared in Figure 9a. These orientations also agree well with those derived from the caliper *P1AZ* measures (Figure S3). For ease of illustration, these orientations are further summarized in rose diagrams of Figure 9b that show the uniform clusters of the BO azimuths over three recognizable depth ranges. From the manual picking over 1650 − 2000 m, the breakouts with a total extent of 130 m share a BO azimuth at N100°E ± 21° (Figure 9b). From 2000 to 2210 m, this azimuth abruptly rotates ~73° centering at 173° ± 20°. The azimuth yet again shifts to N145°E ± 24° at the bottom of the borehole from 2210 − 2315 m covering a total depth of 66 m.

BO widths from the manual picking at these three uniform azimuth clusters seem to become narrower, ranging from 56° ± 18° over 1650 − 2000m, to 46° ± 14° over 2000 − 2210m, and to 42° ± 13° over 2210 − 2315m (Figure 9c). Narrower BO width at the lower depth is counterintuitive since it is normally believed that the in-situ stresses are larger with increasing depth. Correspondingly, if the rock strength stays constant along the depth, the BO width should be wider at the lower depth. Therefore, the observed decrease of the BO width might suggest a larger rock strength. Only the BO width from the manual picking, instead of the automatic picking, is shown in Figure 9c since we found that the low-pass filter applied to the original signal smooths and broadens the signal, leading to larger BO widths picked automatically compared with those picked manually (W. Wang & Schmitt, 2020).

There is another key observation with regards to the BO shapes that must be mentioned. Usually, standard breakouts produced by shear failure at the borehole wall appear in the images as long, parallel vertical stripes. Here, however, the BOs observed appear as opposing convex and concave crescents with many good examples seen the UBI log of Figure 8b. This geometry is consistent with BOs associated with the preferred slip on weak planes before shear failure of the intact rock (Figure 4d).

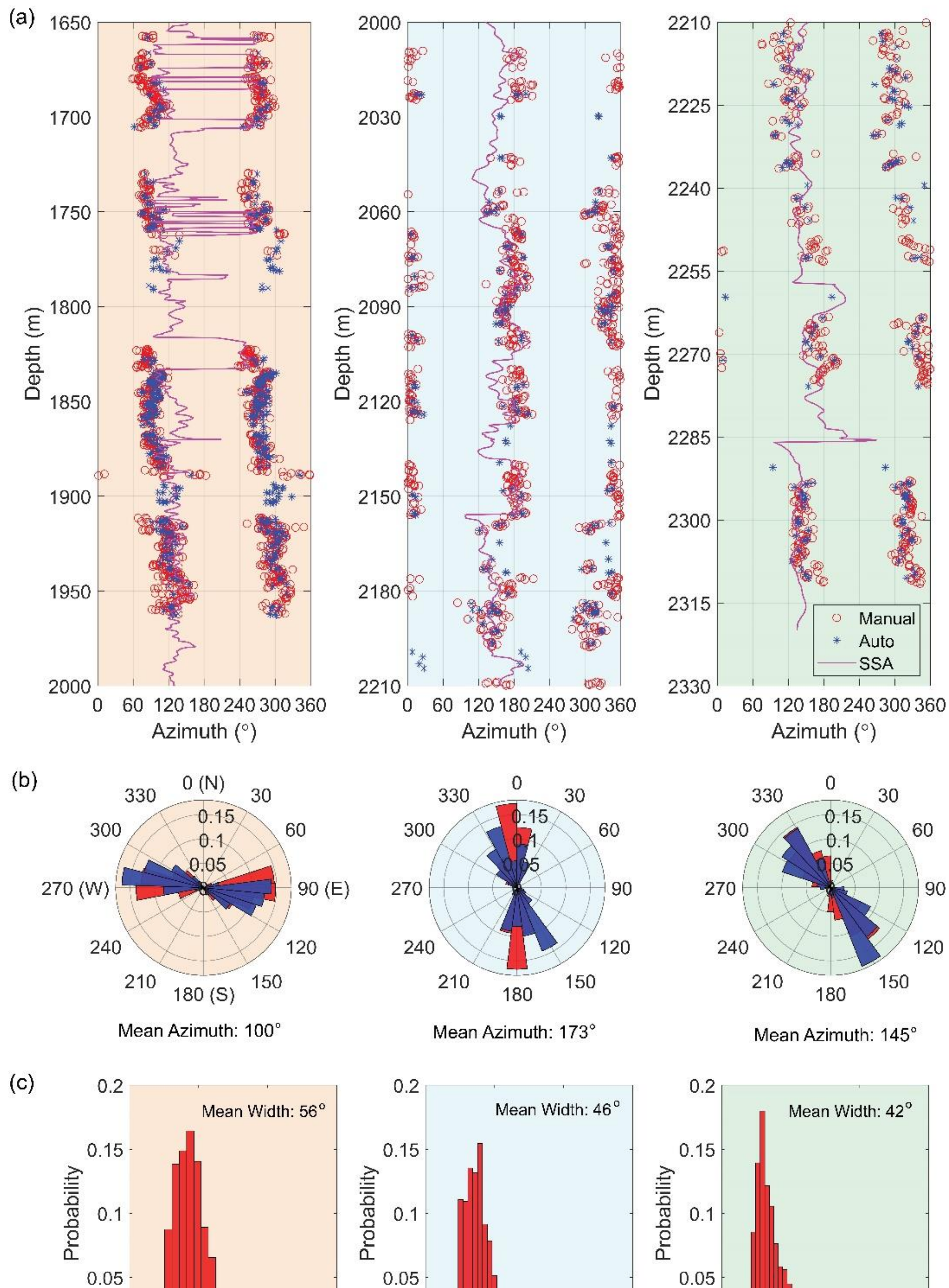

Figure 9 (a) Breakout azimuths from UBI image logs. The red circles and blue asterisks represent, respectively, the breakout azimuths α declared from the manual or automatic picking. The magenta curve represents the Slow Shear Azimuth ($\chi_F + 90°$) from DSI logs. (b) From left to right, the rose histograms represent the BO azimuth α distribution at 1650-2000 m, 2000-2210 m, and 2210-2320 m respectively. The red and blue color represent breakouts from manual and automatic picks. (c) From left to right, the histograms represent the BO width distribution at 1650-2000 m, 2000-2210 m, and 2210-2320 m respectively from manual picks.

5.2.2 Foliations and Fractures

Ultrasonic image logs have recently been used to map foliation orientations in mylonites near the Alpine Fault in New Zealand (Massiot et al., 2018). Here, changes in mineralogic compositions in the metamorphic gneissic layers, as seen in the core samples in Figure 2, provide sufficient variations in elastic impedance (i.e., product of velocity and density) for individual gneissic bands to be clearly visible in both the ultrasonic UBI image logs and electrical FMI image logs (Figure 8a), allowing the strike and dip of the contacts to be measured. Each individual measurement was accomplished by the manual fitting of a sinusoid to each contact as illustrated by Figure 4d. Planar features are obvious in FMI and amplitude UBI image logs, suggesting the relative variation in the resistivity and the acoustic impedance of different mineralogy. However, these same planar features cannot be obviously seen in the travel time UBI image log as this measure is not sensitive to the rock impedance, indicating a lack of change in the shape of the wellbore. Since fractures are normally assumed to cause variations in both the shape and diameter of the wellbore (e.g., Schmitt, 1993), we interpreted these planar features to be foliations instead of fractures. The apparent dip direction and dip angle of the foliations have been converted to the true dip direction and dip angle based on the local wellbore deviation.

The orientations of the foliation planes cluster in three depth-delineated groups that correlate well with the shifts in the breakout orientations. These three orientation distributions (Figure 10, see details in Figure S4) are shown via Kamb contours of the foliation plane poles in a stereographic projection (Allmendinger et al., 2012) and further by comparisons using histograms of the frequencies of azimuths for the breakout, the foliation dip direction, and the slow shear wave polarization (Figure 11). The observed shifts in the foliation orientations of Figure 10 with depth are not unexpected in deformed metamorphic rock masses. The complete geological history of these rocks is not known but given their ages, it is likely they could have experienced multiple periods of deformation. Cleavage refraction, i.e., a change in the metamorphic cleavage orientation, is well known to occur at this scale dependent on the deforming rock’s rheological properties and the variations in mineralogy.

Surprisingly, there are not many continuous fractures observed in the image log (only a very small amount in Table S3). There is further no depth correlation of the vicinity of fractures with the breakout rotations in three depth zones. The lack of fractures might suggest that fractures are either not fully developed in the craton or have been healed. Crosscuts between foliations and fractures in Figure S5 are present while no discernable offsets caused by the potential fracture slippage are observed, indicating the stability of fractures.

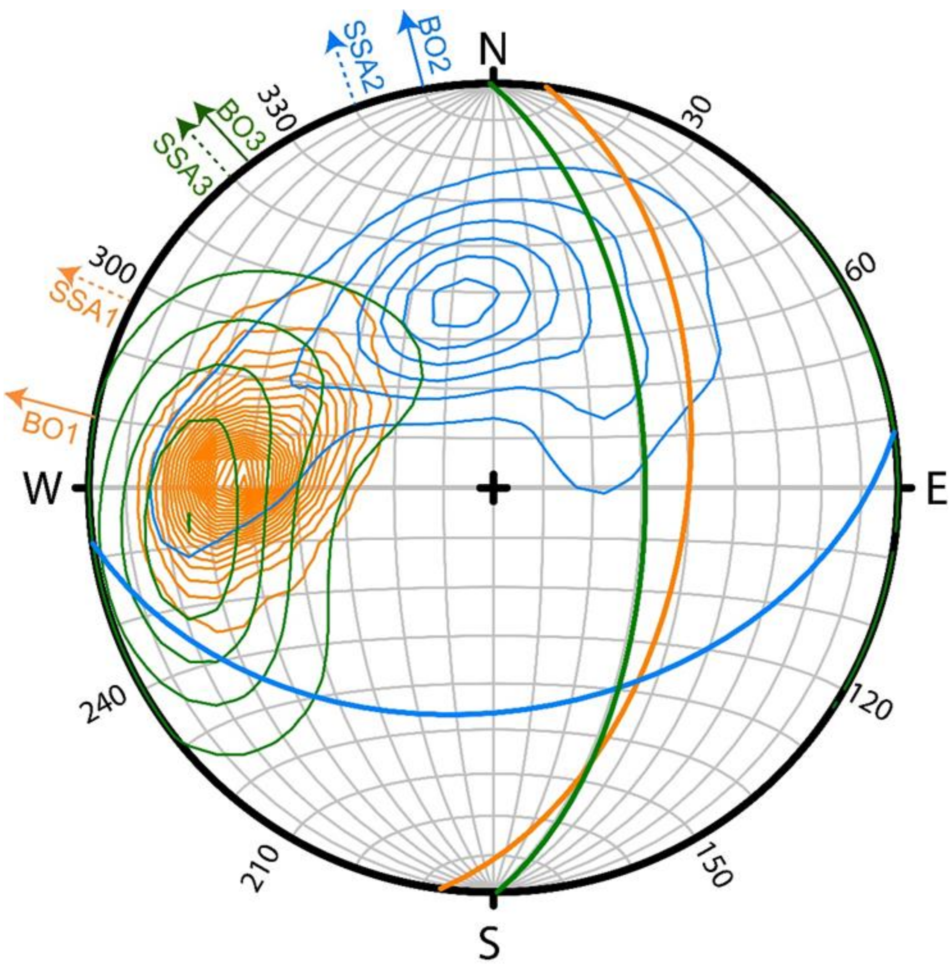

Figure 10. Lower-hemisphere, equal-area stereographic representation of the poles to the foliation planes identified from UBI and FMI logs. Orange, blue, and green contours represent the Kamb contours at the depth of 1000-2000 m, 2000-2210 m, and 2210-2330 m respectively (using Stereonet 11 from Allmendinger et al., 2012). Solid great circles represent the corresponding average foliation plane orientations at these three depth intervals. The average foliation dip direction (ψ_m + 90°) and dip angle β_m for these three depth intervals are: (97.5°, 50.3°), (172.1°, 43.9°), and (89.5°, 59.2°). The arrows at the edge of the circle denote the breakout azimuth (BO1, BO2, BO3) and the slow shear polarization azimuth (SSA1, SSA2, SSA3) respectively at the depth of 1000-2000 m, 2000-2210 m, and 2210-2330 m.

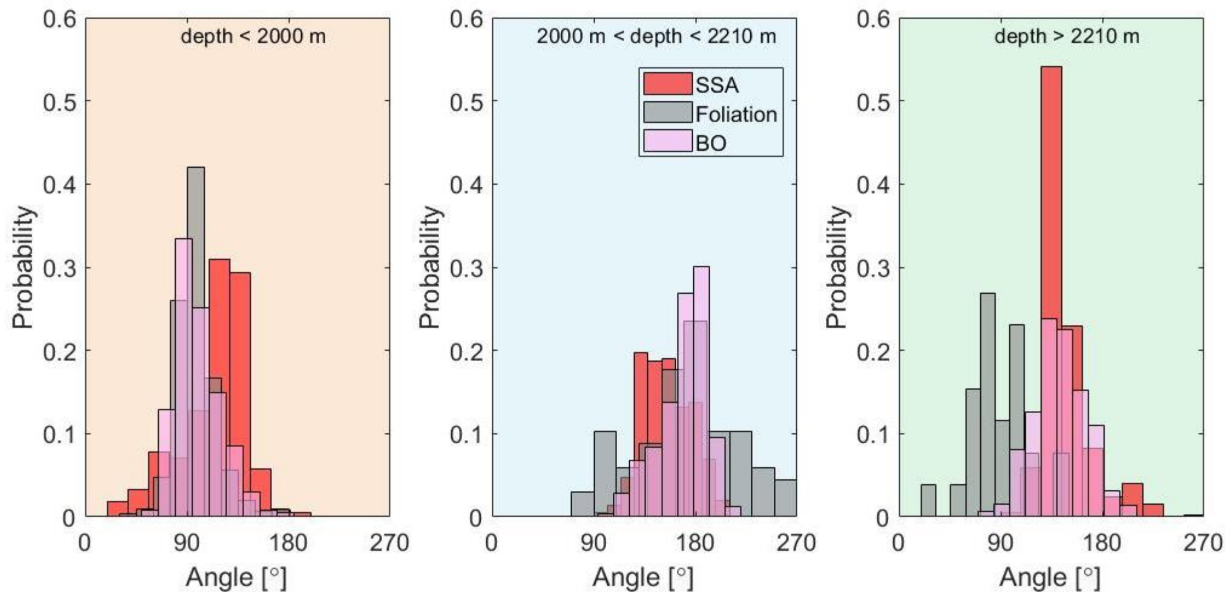

Figure 11. Histograms for breakout azimuth α (grey) from manual picks, slow shear azimuth (red) (χ_F + 90°), and foliation dip direction (purple) (ψ_m + 90°) for three depth sections. Overlaps between these three histograms are obvious at two shallower depth sections (depth < 2000 m and 2000 m < depth < 2210 m), suggesting the foliation-controlled breakouts. However, at the lowest depth section (depth > 2210 m), the foliation dip direction does not correlate with breakout azimuths since minerals are not strongly oriented (Figure 2c).

5.3 Dipole Shear Sonic Log and Rock Continuum Anisotropy

V_{SF} and V_{SS} (Figure 12a) remain distinct from one another along the entire extent of the borehole with the apparent shear slowness anisotropy (*SLOANI*), defined as 100%×(V_{SF} - V_{SS})/V_{SF}, ranging between 3% to 7%. More advanced slowness dispersion of the flexural mode waveforms (Figure 12b) further shows that V_{SF} and V_{SS} are consistently offset from each other across the frequency band. Crossovers of these two dispersion curves, which would indicate the stress-dependent elastic effects dominated near the borehole (see Figure S1), were possibly observed in only one instance at 1642 m. All of these observations taken together indicate that the dipole anisotropy measurement is primarily controlled by the intrinsic anisotropy of the rock mass and not by the stress dependent nonlinear rock behavior near the borehole. This observation is also qualitatively consistent with other anisotropic indictors including the dipping foliations (Figure 8a) and the laboratory wave speed anisotropy measurements (Chan & Schmitt, 2015a).

The fast shear wave polarization azimuth χ_F is another attribute extracted from these logs (Figure 12a). The apparent jumps in the curve are not discontinuities but simply reflect 180° shift in the choice of azimuth by the instrument's algorithm; and this plot shows that this azimuth varies along the borehole. These same azimuths were also plotted with the image log breakout directions in Figure 9a, showing that these agree well with one another. The averages of these azimuths over three different depth ranges are also compared with the foliation plane orientations in Figure 10. These correlations further suggest that the dipole sonic log reflects the intrinsic anisotropy of the rock mass. As noted above, the χ_F will change depending on the dip of the foliation and the anisotropy of the medium. Here, given that the rock mass appears to be TI and that the foliation planes dip steeply (Figure 2 and Figure 10), the χ_F follows the pattern in Figure 5c.

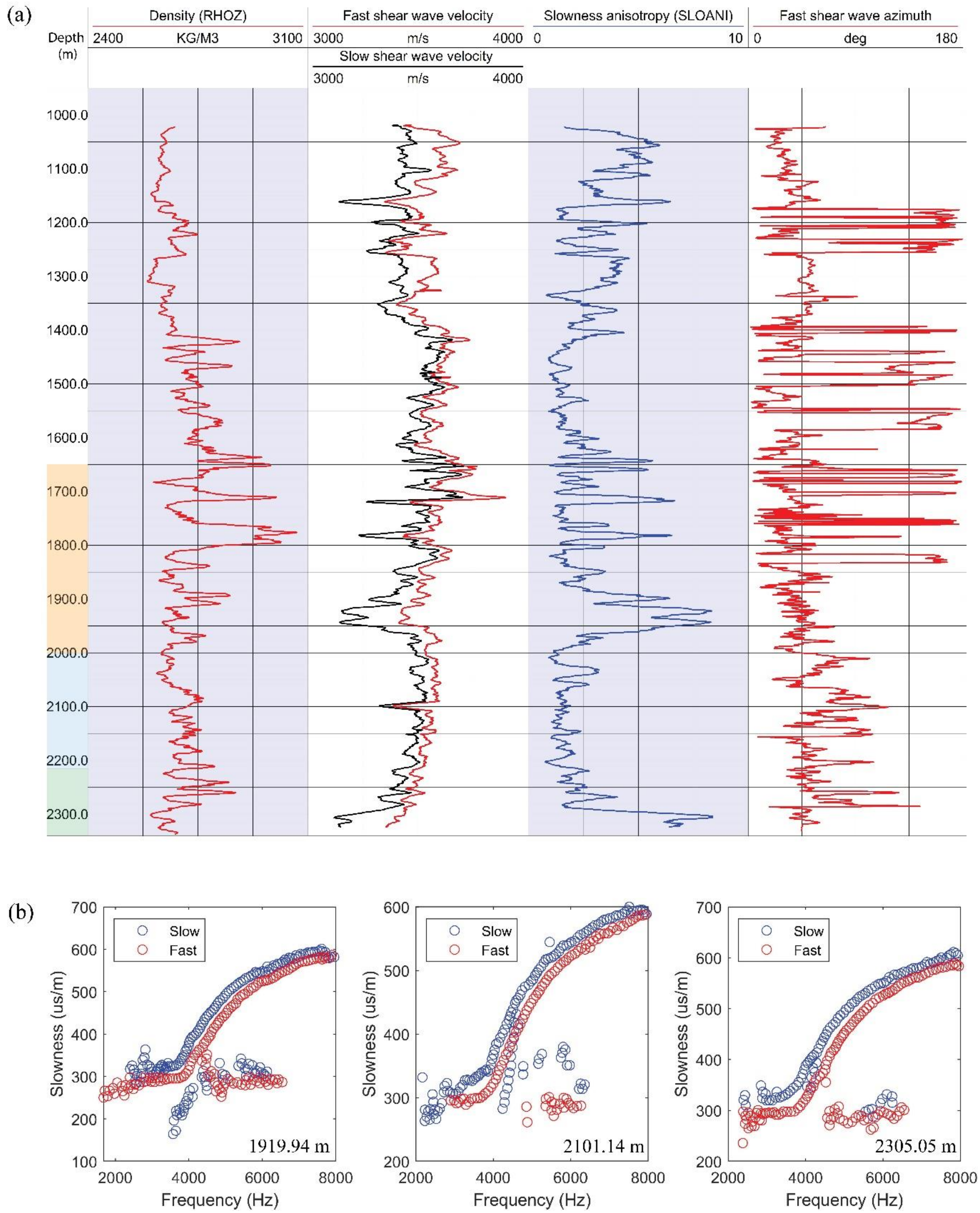

Figure 12. (a) Dipole shear sonic logs. Panel 1: Density shown for reference; Panel 2: Fast V_{SF} and slow V_{SS} shear wave speeds; Panel 3: Slowness anisotropy; Panel 4: Fast shear wave azimuth χ_F (b) Examples of dispersion curves representing the slowness of dipole flexural waves with respect to frequency at three depths. Dispersion curves for fast and slow shear waves are separated, suggesting the material anisotropy.

6. Discussions

6.1 Relations between Metamorphic Texture, Anisotropy, and Breakouts

Before continuing into the discussions, it is worth summarizing the rich set of complementary observations:

1. Crescent-shaped breakouts are observed (Figure 8b) in ultrasonic image logs below 1650 m to nearly the terminal depth (TD). Their azimuths α correlate with those for borehole elongations found from the caliper logs obtained after 2010 (Figure S3).

2. The breakout azimuths α vary with depth, with three distinct sections identified over which the orientations are uniform (Figure 9).

3. Over most of the borehole, these α further correlate with both the dip direction of the foliation planes ($\psi_m + 90^\circ$) and the slow shear wave polarization ($\chi_F + 90^\circ$) (Figure 11), except for the lowest section where α and ($\psi_m + 90^\circ$) deviate by more than 50°. Later we will attribute the observed discrepancy to the foliation-controlled breakouts in the upper two sections and the matrix-controlled breakouts in the lowest section.

4. The dipole shear log dispersion curves almost exclusively indicate that the formation is intrinsically anisotropic. Further, over most of the extent of the borehole, the flexural waves are polarized in directions expected in a steeply dipping TTI foliated metamorphic rock mass (Figure 5c).

Taken together, these observations as summarized in Figure 11 suggest that the directions of the breakouts in the Hunt Well are strongly controlled by the metamorphic texture, as indicated by foliation planes' orientations and wave speed anisotropy directions, via slip on weak foliation planes in the two upper sections. Below we further test this hypothesis, in contrast with workers who usually would assume that the borehole elongation is controlled solely by defined stress concentrations from Kirsch (1898) and would simply average the observed variations to arrive at a final stress direction.

6.2 Stress Field Interpretations

The shift in the breakout directions can be interpreted two ways. In the first and novel interpretation here, the greatest horizontal compression remains NE-SW, consistent with the remarkably uniform regional stress direction (Figure 1), but with variations in the breakout directions instead controlled by the rock's elastic and strength anisotropy due to foliations. The second and conventional interpretation does not take the effect of rock anisotropy on the breakout orientation into consideration but replies on the isotropic rock assumption. In this case the changes in the breakout azimuths can only be accommodated by imposing a heterogenous stress field.

Many similar observations of breakout rotations appear in the literature (e.g., Barton & Zoback, 1994; Brudy et al., 1997; Goswami et al., 2019, 2020; Huber et al., 1997; Lund & Zoback, 1999; Pierdominici et al., 2011; Rajabi et al., 2016; Schoenball & Davatzes, 2017; Shamir & Zoback, 1992; Wu et al., 2007), but, contrary to the case here, these rotations are primarily attributed to perturbations of faults and fractures, and are often confined to the immediate vicinity of the discontinuity. This explanation cannot easily be applied here due to the lack of any obvious correlated fractures or other rock mass discontinuities; and it may require relying on other unproven mechanisms such as residual stresses.

Below we contrast individual analyses of the data under both the weak-plane anisotropic (WeakBO) paradigm (that does not require stress field rotation) and the conventional isotropic (Kirsch) paradigm (which requires stress field rotation with depth) for purposes of comparison. We show that these two will give significantly different estimates of stress conditions.

6.2.1 WeakBO Paradigm: Foliation Controlled Breakouts under Constant Stress Field Orientation

We used Monte Carlo simulations to model the range of feasible stress fields that are consistent with the breakouts being formed by failure along weak planes controlled by various oriented foliations but within a uniformly direct stress field. Considering the elastic anisotropy, the input stiffness matrix of the rock (Text S3) was assumed to be transverse isotropic and was measured on a core sample from the bottom of the Hunt well by Chan and Schmitt (2015a). In addition, we added the weak plane strength anisotropy to test whether strength anisotropy explains the changing breakout azimuths using the algorithm ***EASAfail***. ***EASAfail*** first calculates the normal $\sigma_n(r,\theta)$ and shear $\tau(r,\theta)$ tractions (Eq. 1) on the weak plane by rotating the local r-θ dependent concentrated stresses from the input Andersonian [S_H, S_h, S_V] principal stresses using the Lekhnitskij-Amadei formulation (Amadei, 1983; Lekhnitskij, 1963). The algorithm then determines whether the rock remains stable or experiences intact or slip plane failure (or both) leading to the breakout formation (W. Wang et al., 2021, 2022).

The model presumed α_H = N50°E prevailing along the borehole (Morin, 2017) and the vertical stress S_V was calculated by the integration of the density log (Table 2). Both the borehole mud P_W and pore P_P fluid pressures were omitted as expected for the air-filled borehole after it was bailed dry in 2003. We assumed further that in each zone the weak slip planes are parallel to the foliation planes given by the average orientations at three depth sections, and the two horizontal stresses were allowed to randomly vary over the ranges with respect to S_V as indicated in Table 2.

As indicated above, values of C_o and ϕ_o for the intact rock and C_w and ϕ_w for the weak foliation plane are also necessary for the modelling, but these are highly uncertain. There are numerous experimental rock failure measurements described in the literature that show clearly the variation of compressive strength with tilt, demonstrating strength minimums at ~*35° to 55°* (e.g., Acosta & Violay, 2020; Attewell & Sandford, 1974; Bai & Young, 2020; Berčáková et al., 2020; Cho et al., 2012; Condon et al., 2020; Donath, 1961; McCabe & Koerner, 1975; Nasseri et al., 2003). Obtaining values from the literature can be difficult as the results often only obtain unconfined compressive strengths that cannot provide information on the friction. However, McCabe and Koerner (1975) reported the failure of weaker foliation planes in a mica schist suggesting $\phi_w = 19°$ (μ = 0.34) and C_w = 19.3 MPa by taking the lowest value while ϕ_o = 28° (μ = 0.53) and C_o = 41.4 MPa by taking the highest value. Recently, Alejano et al. (2021) fit an extensive series of failure tests on a slate to the weak plane model obtaining $\phi_w = 17.8°$ (μ = 0.32), C_w = 10.8 MPa, ϕ_o = 47.2 (μ = 1.07) and C_o = 25.1 MPa. In order to account for different reported strength parameters, we used the averaged strength of the above two exemplars for the intact rock strength: ϕ_o = 37.6° (μ = 0.77) and C_o = 33.3 MPa (Table 2). The weakness plane strength parameters (ϕ_w, C_w) were assumed unknown and allowed to randomly vary over the ranges with respect to the intact matrix strength parameters (ϕ_o, C_o) indicated in Table 2. Again, under the assumption, the resulting pattern of breakouts formed was calculated in either failure in the rock matrix (ϕ_o, C_o) or failure in the weakness plane (ϕ_w, C_w).

Table 2 Input Parameters of the WeakBO and Kirsch Paradigm

Parameters		Depth zone		
Zone	/	1	2	3
Depth	m	1650	2000	2210
Measured parameters				
Elastic properties	C_m (GPa)	TI stiffness matrix given in Text S3		
Foliation orientations (Figure 10)	Strike ψ_m (°) Dip direction (°) Dip β_m (°)	7 97 50	82 172 44	0 90 59
Breakout observations (Figure 9)	Width Θ (°)	56 ± 18	46 ± 14	42 ± 13
	Azimuth α (°)	100 ± 21	173± 20	145 ± 24
Vertical stress	S_V (MPa)	43	52	58
WeakBO paradigm: S_H azimuth[1]	α_H (°)	N50°E		
Kirsch paradigm: S_H azimuth[2]	α_H (°)	010°	083°	055°
Values from literature or assumed ranges				
Stress magnitude ranges	S_H/S_V	[0.1, 2.0]		
	S_h/S_V	$[0.1, 2.0] \leq S_H/S_V$		
Averaged intact strength[3,4]	C_o (MPa)	33.3		
	ϕ_o (°) - μ	37.6° - 0.77		
WeakBO paradigm: weak plane strength ranges	C_W/C_o	[0.3, 0.8]		
	ϕ_W/ϕ_0	[0.3, 0.8]		
Kirsch paradigm: weak plane strength ranges	C_W/C_o	1		
	ϕ_W/ϕ_0	1		

Note: [1]Morin (2017); [2]Perpendicular to α; [3]McCabe and Koerner (1975); [4]Alejano et al (2021).

The Monte Carlo simulation carried out 10^6 realizations for each of the three depths in Table 2. Therefore, there are in total 3 independent simulation sets for the WeakBO paradigm. In each realization, firstly, four random numbers were drawn for S_H, S_h, C_W and ϕ_W in the given ranges respectively. If the randomly drawn S_h is larger than S_H, S_h and S_H will be drawn randomly for another arounds until the resulting $S_h \leq S_H$. Secondly, fixed parameters in Table 2 along with these four random parameters were fed into the recently developed program ***EASAfail*** to calculate the modelled breakout width and azimuth. Therefore, after 10^6 realizations, we had a corresponding $10^6 \times 2$ matrix that stores modelled breakout width and azimuth for each combination of four random parameters [S_H, S_h, C_W, ϕ_W]. Finally, feasible combinations of parameters were screened from the matrix where the modelled breakout geometry (azimuth and width) is within one standard deviation of the observed breakout geometry.

The result for the simulation set at 1650 m is shown in Figure 13a where each instance of weakness plane controlled breakouts appears as a point in the S_H-S_h-C_W space colored according to the associated ϕ_w. The data cloud of Figure 13a illustrates broad ranges of horizontal stress magnitudes (S_H = [0,60 MPa] and S_h = [0,40 MPa]) that satisfy the failure criterion. However, when shown in the 2D S_H-S_h space (Figure 13b), the feasible solutions cluster with the maximum probability indicated by the white hexagram at S_h = 20.0 MPa and S_H = 32.6 MPa. These values were used to calculate the expected breakout development that is consistent with slip on the weak foliation plane (Figure 13c), resulting in the observed breakout azimuth deviating from the conventionally expected S_h azimuth ($\alpha_H + 90° = 140°$).

Please refer to Figure S6-S7 for results of other depth sections. The modelled failure patterns indicate that the breakouts are foliation controlled for the upper two depth zones 1 and 2. In contrast, in the lowest zone 3 (2210-2315m), both matrix shear failures and weak-plane slip failures exist (see the enlarged inset in Figure S7c for the tiny failure in the intact rock matrix), producing breakouts near the expected S_h direction. The less dominating effect of foliations on the breakout azimuth in the lowest zone 3 is reasonable considering the poorly developed foliations shown in Figure 2c compared with the strongly foliations in the shallower depth (Figure 2b).

To summarize, these modelling results suggest that the shifts in the observed breakout azimuths (Figure 9) can be explained by foliation-controlled slip failure within a rock mass subjected to the same principal stress orientations.

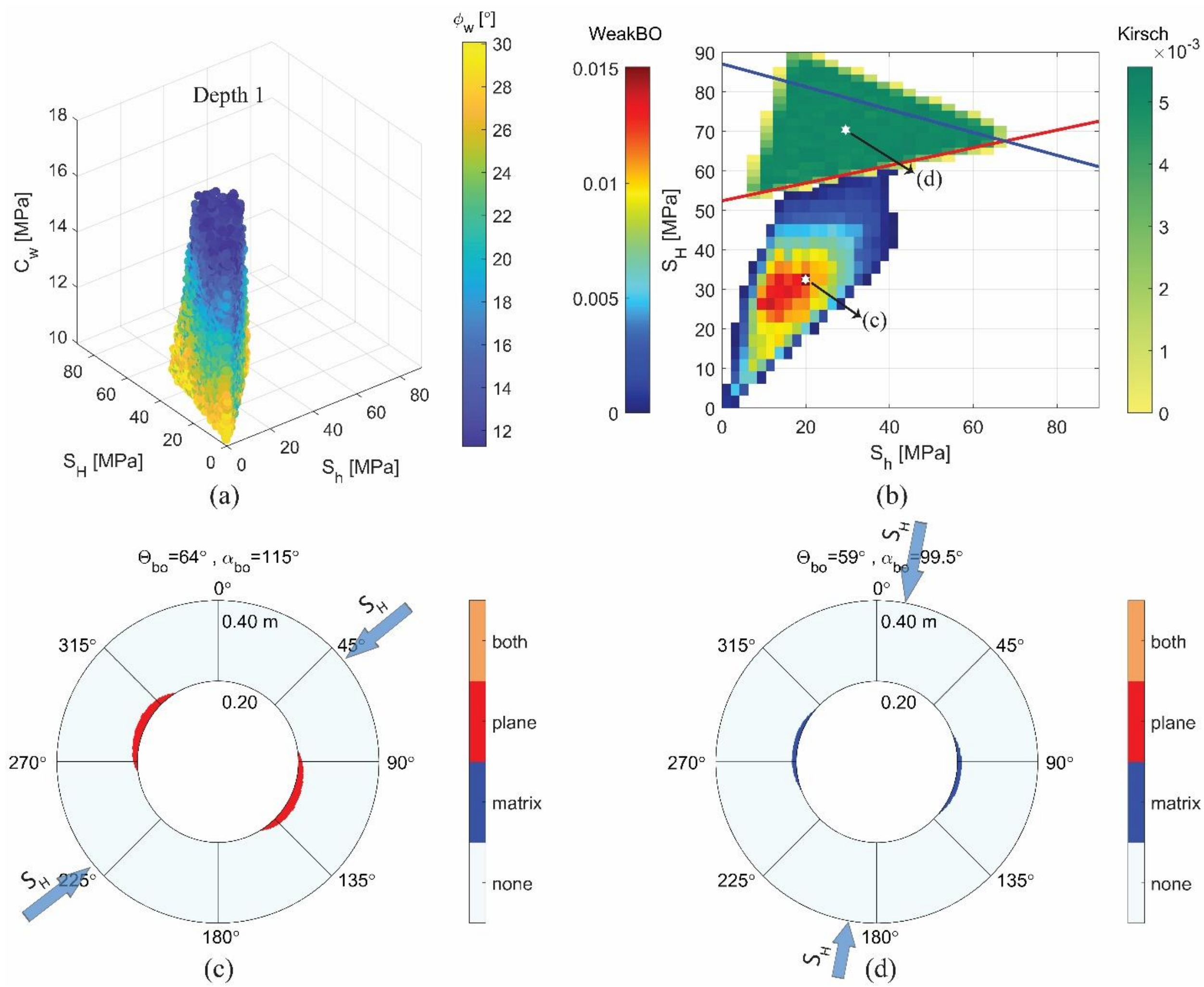

Figure 13. Feasible stress magnitudes and modelled failure patterns at the depth zone 1 (1650 m). (a) Suitable stress magnitudes and weakness plane strengths with a constant S_H azimuth (N50° E) in elastic and strength anisotropic formations (WeakBO). Markers are color-coded by the weakness plane internal frictional angle ϕ_w. (b) Superimposed feasible stress magnitudes for the WeakBO paradigm and for the Kirsch paradigm with a rotated S_H azimuth (N10° E) in strength isotropic but elastic anisotropic formations. The colorbar represents the probability for each combination of horizontal stress magnitudes with the highest probability in the WeakBO paradigm and the median in the Kirsch paradigm denoted by the white hexagrams. The solid blue and red lines are bounds using Barton et al.'s equations (1988) with the breakout width equal to 74° and 38° respectively. (cd) Modelled failure patterns using the stress magnitudes denoted by the white hexagrams in (b) for the WeakBO and Kirsch paradigms respectively. Blue arrows are the input maximum horizontal stress azimuth. Light blue, dark blue, red, and orange areas represent four cases respectively: no failure, failure in the rock matrix, failure in the weak plane, and failure in both the rock matrix and the weak plane. Two numbers at the top of each subfigure represent the modelled breakout width Θ_{bo} and azimuth α_{bo} respectively. Parameters [C_w, ϕ_w, S_H, S_h] used to generate (c) and (d) are [13.5 MPa, 16.9°, 32.6 MPa, 20.0 MPa] and [C_o, ϕ_o, 70.4 MPa, 29.5 MPa].

6.2.2 Kirsch Paradigm: Conventional Strength Isotropic Analysis Requiring Stress Field Rotation

Under the conventional isotropic breakout interpretation, varying breakout azimuths require the horizontal stress directions change along the borehole. Again, three sets of simulations (one for each depth) were carried out under the Kirsch paradigm. Most of the parameters of Table 2 remained the same except that now the far-field S_H azimuth $\boldsymbol{\alpha_H}$ for each depth was set perpendicular to the observed breakout azimuth α and the strength anisotropy was effectively omitted by equating $\phi_W = \phi_o$ and $C_W = C_o$. As for the Kirsch paradigm, 10^6 Monte Carlo realizations were again carried out for different combinations of S_H and S_h to satisfy the observed breakout geometry, the results of which were included in Figure 13b for comparisons.

In this paradigm, the realizations leading to breakouts fall with essentially equal probability (as indicated by the uniform green color in Figure 13b) across a triangular zone; and the satisfactory ranges of S_H and S_h are broader than those for the WeakBO paradigm. This extensive modelling results highlight the large uncertainties inherent to breakout width analyses in general. Perhaps expectedly, this zone is somewhat contained by the delimiting lines using a popular formula to estimate S_H from the breakout width Θ (Barton et al., 1988):

$$S_H = \frac{UCS - S_h(1 - 2\cos\Theta)}{1 + 2\cos\Theta} \tag{2}$$

where within the Mohr-Coulomb criterion (Eq. 1) the uniaxial compressive strength $UCS = 2C_o \cos\phi_o/(1 - \sin\phi_o)$. Further exploration of Eq. (2) shows its insensitivity to the breakout width Θ and this helps to explain the breadth of possible ranges (see Text S4). A slight mismatch between the modelled feasible zones (green triangle) and the bounded region from analytical lines (blue and red solid lines) is due to the fact that the simulation takes the elastic anisotropy into account whereas the analytical lines ignore it.

Detailed results for other depths of WeakBO and Kirsch paradigms are provided in Figure S6-S7, but the stress ranges determined are summarized in Figure 14. For the upper two depth zones of the crystalline basement (1650-2210 m), feasible stress regions in the Kirsch paradigm are well above those in the WeakBO paradigm with the WeakBO paradigm failing in the weakness plane and the Kirsch paradigm failing in the intact rock matrix (Figure 13 and Figure S6). A lower far-field stress magnitude is enough to generate failure in the weakness plane whereas a higher far-field stress magnitude is required to fail in the intact rock matrix. In contrast, at the lowest depth zone 3 (2210-2315 m), rocks fail both in the intact rock matrix and in the weakness plane under the WeakBO paradigm (Figure S7); therefore, the resulting feasible stress fields from two paradigms overlap with one another.

To sum up, considering formation isotropy with no other structural disturbances, observed heterogenous breakout azimuth needs to be explained by a heterogenous stress field with a rotated $\boldsymbol{\alpha_H}$ along the depth. If the heterogenous stress field is truly the underlying reason for the observed breakout azimuth rotation, the stress field in the Canadian Shield is far more complicated and is inconsistent with the uniform NE-SW compression in the overlying sedimentary basin.

6.3 Stress Field along the Borehole

Wide feasible horizontal stress magnitudes from Monte Carlo simulations at three depth zones for both the WeakBO and Kirsch paradigms cannot yield accurate quantitative stress information; however, qualitative comparisons could be conducted. Two packer tests were conducted that provide lower bounds on the S_h magnitude. Instantaneous Shut-In Pressure (ISIP) was 7 MPa at 873.0 m and at 1370 m, the packer was pressurized at 11.5 MPa and held the pressure for a long time without pressure dropping. Since the pressures from the test were measured at the surface, head pressure needs to be added. However, the trustworthiness of the pressure from packer tests is doubtful since the rock never breaks in the field packer tests.

The interquartile range (IQR: third quartile minus first quartile) of S_h magnitude for the WeakBO and Kirsch paradigms overlap (Figure 14b) whereas the IQR of S_H magnitude (Figure 14a) are almost separatable. The overestimation of S_H magnitude in the Kirsch paradigm is reasonable since larger far-field stresses are necessary for the intact rock failure than the weakness plane failure given that the intact rock strength is stronger than the weakness plane strength. The IQRs of S_h and S_H magnitude in the WeakBO paradigm are both smaller than the vertical stress integrated from density logs; therefore, the craton is in the normal faulting regime and close to the strike-slip faulting regime at the bottom. However, in the Kirsch paradigm, the depths of interest are all in the strike-slip faulting regime due to the overestimation of S_H magnitude.

Reiter and Heidbach (2014) numerically modelled the stress field in the Alberta basin. The model extended to 80 km depth, including upper mantle, metamorphic crustal basement, and foreland sedimentary basin, which was constrained by various geophysical data and the extensive knowledge of sedimentary geological structure from thousands of boreholes over a 700 km × 1200 km rectangular area oriented largely to the CDF. The model was iteratively constrained using borehole measures of S_V, α_H, and S_h as well as a few estimates of S_H. Their model (superimposed in Figure 14) has a crossover of S_H and S_v at the first depth section considered in the study; therefore, for the depth where breakouts were observed in the current study (>1650m), S_V is slightly larger than S_H, suggesting the craton is in the normal faulting regime. Faulting regimes inferred from their model are similar as those inferred from the WeakBO paradigm, favoring the first interpretation of a constant S_H azimuth (N50° E) in strength anisotropic formations.

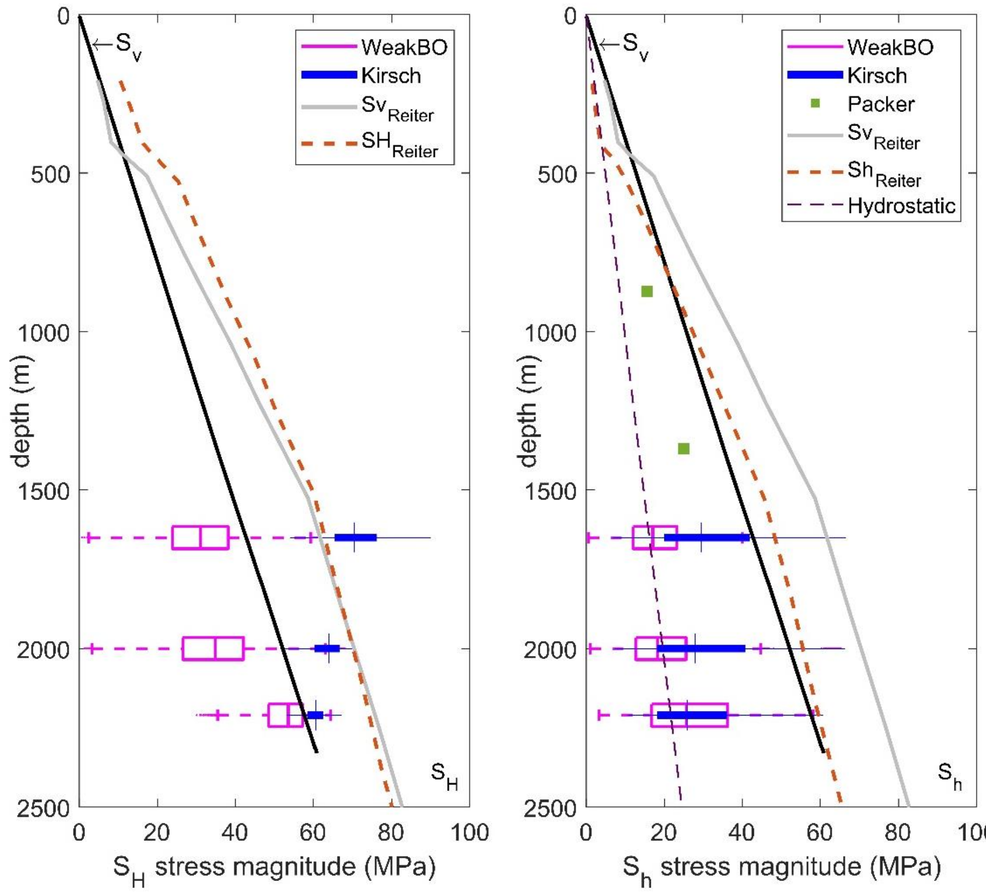

Figure 14. Feasible stress magnitudes. The solid black line represents the vertical stress magnitude calculated from the density logs. (a) Magenta and blue boxplots are feasible S_H magnitude for the WeakBO and Kirsch paradigms respectively. Solid gray and dashed brown lines represent the vertical and S_H magnitude from Reiter and Heidbach (2014). (b) Magenta and blue boxplots are feasible S_h magnitude for the WeakBO and Kirsch case. Solid gray and dashed brown lines represent the vertical and S_h magnitude from Reiter and Heidbach (2014). The dashed purple line represents the hydrostatic pressure (ρ = 1000 kg/m^3). Green markers represent two packer tests conducted at 873 and 1370 m (Note: have added head pressure to the measured value).

6.4 Stability Analyses for Shear Failures

Stability analyses were conducted to examine the present-day shear failure potential using far-field stresses interpretated from Figure 14. Since there are wide ranges of feasible stress states, we took a set of horizontal stress magnitudes with the highest probability as a representative for the WeakBO paradigm and took the median as a representative for the Kirsch paradigm (denoted by hexagrams in Figure 13b). One thing to reiterate is that the Kirsch paradigm has a nearly equal probability and the minor differences only reflect random variations. Therefore, the median of the stress magnitude is considered as an appropriate representative value for the Kirsch paradigm. Using the rock matrix strength (C_o, ϕ_o) in Table 2 and the calculated feasible weakness plane strength (C_w, ϕ_w), it is obvious that the craton is rather stable and far from the critical frictional failure equilibrium in Figure 15. Moreover, even using $C_o = 0$ and $\mu = 1$ as researchers commonly assume, the same conclusion of stability could again be drawn. If $C_o = 0$ and $\mu = 0.6$, however, the failure envelop touches the Mohr circle of the WeakBO paradigm at the lower two depth sections, indicating the potential slippage failure of the perfectly oriented open fractures. More comprehensive field investigations are highly required for safe subsurface applications (e.g., geothermal exploration, wastewater disposal) in the crystalline basement to prevent potential seismicity.

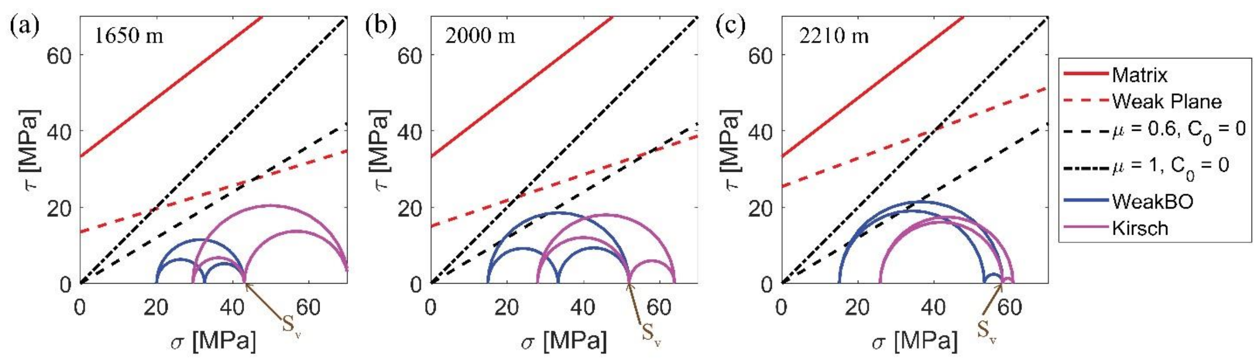

Figure 15. Mohr circles for three depth zones (a: 1650 m, b: 2000 m, c: 2210 m). Pore pressure is assumed to be zero. S_H and S_h magnitudes drawing the Mohr circles are those having the highest probability for the WeakBO paradigm and the median for the Kirsch paradigm (denoted by the white hexagrams in Figure 13b). Blue and magenta Mohr circles represent the far-field stresses inferred from the WeakBO and Kirsch paradigms respectively. Solid and dashed red lines are respective failure envelops for the rock matrix (C_o, ϕ_o) and weakness plane (C_w, ϕ_w). Dashed and dashdot black lines represent two standard assumptions of the rock strength: 1. C_o=0, μ=0.6; 2. C_o=0, μ=1.

7 Conclusions

The Hunt Well in NE Alberta provides a rare access to study the state of stress into a stable and historically aseismic portion of the North American Craton. Stresses within these cratons have largely been ignored, but such knowledge becomes increasingly important as societal needs to extract energy and deposit wastes accelerate. We observed stress dependent borehole breakouts along this borehole that can provide some constraints on crustal stress states. However, the orientations of the breakouts rotate by as much as 73° across different zones, and if analyzed under the usual isotropic Kirsch assumptions, the principal stress directions along the borehole would have to also change. The breakout rotations, however, correlate also with shifts in the metamorphic foliations as seen in image logs and principal anisotropic axes deduced from the dipole shear logging; and this suggests that the breakout orientations are controlled in this case by the rock anisotropy. Models of the breakouts that incorporate a weak failure plane coincident with the foliation validate that breakouts with rotated azimuths can all form under the same uniform principal stress directions. This suggests that care needs to be taken when interpreting breakout orientations in foliated metamorphic terranes and, by extension, other anisotropic formations such as fissile shales with weak bedding planes.

The state of stress was constrained by the Monte Carlo modelling of the observed breakout widths and directions using both a conventional strength isotropic Kirsch-based paradigm and a more recently developed model that incorporates rock elastic and strength anisotropy. The anisotropic model suggests lower stress magnitudes and the crust may not be critically stressed in this area, which are consistent with the stable aseismic character of the craton. However, the Monte Carlo modelling also illustrates that stress magnitude estimates made using such breakout analyses are quite insensitive and allow for a wide range of possible stress states. Additional quantitative stress measurements, particularly hydraulic fracturing tests, are necessary to more properly characterize the stress state at depth.

Attention must be paid when conducting stress analysis based on drilling induced features since the study stressed that breakout azimuth cannot represent the minimum principal stress direction if strength anisotropy exists. However, without additional information we also cannot rule out the possibility that the stress field is indeed heterogeneous at different depths with varying maximum horizontal principal stress azimuth. The stress field in the crystalline basement might be overprinted by the remnant residual stresses, causing stress variations along depths. More geophysical investigations need to be conducted for future research to confidently answer whether the observed heterogenous breakout azimuth is ascribed to the failure along the weak foliation plane or the heterogenous far-field stress in the Canadian Shield.

Acknowledgements

Field studies of the Hunt Well were funded as a part of the Geothermal Resources component of the Helmholtz-Alberta Initiative, the Canada Research Chairs program, and the Natural Sciences and Engineering Research Council of Canada. W. Wang was supported in part by the Ross Fellowship and the Graduate School Summer Research Grant from Purdue University. Recognition goes to G. Nieuwenhuis for logistics associated with organizing the field campaigns and the GFZ Operational Support Group overseen by J. Kueck for logging services. We acknowledge the use of Stereonet 11 from R. Allmendinger for the stereographic projection.

Open research

Data Availability Statement

The raw and processed logging data, along with the Matlab code to generate figures in the study are publicly available in Schmitt et al. (2022) on the Canadian Dataverse Repository, following the citation: Schmitt, D. R., Wang, W., & Chan, J. (2022). Geophysical Logging and Image Data from the Hunt Well, NE Alberta [Dataset]. Borealis. https://doi.org/10.5683/SP3/YYNVW8

Two programs used in the study (***EASAfail***, ***BOAPFIL***) are available on the Purdue University Research Repository (PURR). ***EASAfail*** can be downloaded from the following citation: Wang, W., Schmitt, D. R., Li, W. (2021). Failure pattern around the borehole in elastic and strength anisotropic rock formations [Software]. Purdue University Research Repository. doi:10.4231/0NWT-5Y39. ***BOAPFIL*** can be accessed at: Wang, W., Schmitt, D. R. (2022). BreakOut Automatic Picking From Image Logs (BOAPFIL) [Software]. Purdue University Research Repository. doi:10.4231/RTAW-JW77.

References

Acosta, M., & Violay, M. (2020). Mechanical and hydraulic transport properties of transverse-isotropic Gneiss deformed under deep reservoir stress and pressure conditions. *International Journal of Rock Mechanics and Mining Sciences*, *130*, 104235.

https://doi.org/10.1016/j.ijrmms.2020.104235

Agheshlui, H., & Matthai, S. (2017). Uncertainties in the estimation of in situ stresses: effects of heterogeneity and thermal perturbation. *Geomechanics and Geophysics for Geo-Energy and Geo-Resources*, *3*(4), 415–438. https://doi.org/10.1007/s40948-017-0069-z

Alejano, L. R., González-Fernández, M. A., Estévez-Ventosa, X., Song, F., Delgado-Martín, J., Muñoz-Ibáñez, A., et al. (2021). Anisotropic deformability and strength of slate from NW-Spain. *International Journal of Rock Mechanics and Mining Sciences*, *148*, 104923. https://doi.org/10.1016/j.ijrmms.2021.104923

Allmendinger, R. W., Cardozo, N., & Fisher, D. (2012). *Structural geology algorithms: vectors and tensors*. Cambridge: Cambridge University Press. https://doi.org/10.1017/CBO9780511920202

Amadei, B. (1983). *Rock anisotropy and the theory of stress measurements*. Berlin: Springer-Verlag. https://doi.org/10.1007/978-3-642-82040-3

Amadei, B., & Pan, E. (1992). Gravitational stresses in anisotropic rock masses with inclined strata. *International Journal of Rock Mechanics and Mining Sciences & Geomechanics Abstracts*, *29*(3), 225–236. https://doi.org/10.1016/0148-9062(92)93657-6

Anderson, E. M. (1951). *The dynamics of faulting and dyke formation with applications to Britain*. Edinburgh: Oliver and Boyd.

Ardakani, E. P., & Schmitt, D. R. (2016). Geothermal energy potential of sedimentary formations in the Athabasca region, northeast Alberta, Canada. *Interpretation*, *4*(4), SR19–SR33. https://doi.org/10.1190/INT-2016-0031.1

Ask, M., Kukkonen, I., Pierdominici, S., & Kueck, J. (2016). Determination of stress orientation in the Outokumpu deep drill hole, Finland. *EGU General Assembly*, *18*, EGU2016-12881.

Attewell, P. B., & Sandford, M. R. (1974). Intrinsic shear strength of a brittle, anisotropic rock—I: experimental and mechanical interpretation. *International Journal of Rock Mechanics and Mining Sciences & Geomechanics Abstracts*, *11*(11), 423–430. https://doi.org/10.1016/0148-9062(74)90453-7

Azzola, J., Valley, B., Schmittbuhl, J., & Genter, A. (2019). Stress characterization and temporal evolution of borehole failure at the Rittershoffen geothermal project. *Solid Earth*, *10*(4), 1155–1180. https://doi.org/10.5194/se-10-1155-2019

Bai, Q., & Young, R. P. (2020). Numerical investigation of the mechanical and damage behaviors of veined gneiss during true-triaxial stress path loading by simulation of in situ conditions. *Rock Mechanics and Rock Engineering*, *53*(1), 133–151. https://doi.org/10.1007/s00603-019-01898-2

Barton, C. A., & Zoback, M. D. (1994). Stress perturbations associated with active faults penetrated by boreholes: possible evidence for near-complete stress drop and a new technique for stress magnitude measurement. *Journal of Geophysical Research: Solid Earth*, *99*(B5), 9373–9390. https://doi.org/10.1029/93JB03359

Barton, C. A., Zoback, M. D., & Burns, K. L. (1988). In-situ stress orientation and magnitude at the Fenton Geothermal Site, New Mexico, determined from wellbore breakouts. *Geophysical Research Letters*, *15*(5), 467–470. https://doi.org/10.1029/GL015i005p00467

Bauer, R. A., Carney, M., & Finley, R. J. (2016). Overview of microseismic response to CO2 injection into the Mt. Simon saline reservoir at the Illinois Basin-Decatur Project. *International Journal of Greenhouse Gas Control*, *54*, 378–388. https://doi.org/10.1016/j.ijggc.2015.12.015

Bell, J. S., & Gough, D. I. (1979). Northeast-southwest compressive stress in Alberta evidence from oil wells. *Earth and Planetary Science Letters*, *45*(2), 475–482. https://doi.org/10.1016/0012-821X(79)90146-8

Bérard, T., & Cornet, F. H. (2003). Evidence of thermally induced borehole elongation: a case study at Soultz, France. *International Journal of Rock Mechanics and Mining Sciences*, *40*(7–8), 1121–1140. https://doi.org/10.1016/S1365-1609(03)00118-7

Berčáková, A., Melichar, R., & Souček, K. (2020). Mechanical properties and failure patterns of migmatized gneiss with metamorphic foliation under UCS test. *Rock Mechanics and Rock Engineering*, *53*(4), 2007–2013. https://doi.org/10.1007/s00603-019-02012-2

Bondarenko, N., Williams-Stroud, S., Freiburg, J., & Makhnenko, R. (2021). Geomechanical aspects of induced microseismicity during CO2 injection in Illinois Basin. *The Leading Edge*, *40*(11), 823–830. https://doi.org/10.1190/tle40110823.1

Boness, N. L., & Zoback, M. D. (2006). A multiscale study of the mechanisms controlling shear velocity anisotropy in the San Andreas Fault Observatory at depth. *Geophysics*, *71*(5), F131–F146. https://doi.org/10.1190/1.2231107

Brudy, M., & Zoback, M. D. (1999). Drilling-induced tensile wall-fractures: Implications for determination of in-situ stress orientation and magnitude. *International Journal of Rock Mechanics and Mining Sciences*, *36*(2), 191–215. https://doi.org/10.1016/S0148-9062(98)00182-X

Brudy, M., Zoback, M. D., Fuchs, K., Rummel, F., & Baumgärtner, J. (1997). Estimation of the complete stress tensor to 8 km depth in the KTB scientific drill holes: Implications for crustal strength. *Journal of Geophysical Research: Solid Earth*, *102*(B8), 18453–18475. https://doi.org/10.1029/96JB02942

Burwash, R. A., McGregor, C. R., & Wilson, J. A. (1994). Precambrian basement beneath the Western Canada Sedimentary Basin. In G. D. Mossop & I. Shetsen (Eds.), *Geological atlas of the Western Canada sedimentary basin* (pp. 49–56). Canadian Society of Petroleum Geologists and Alberta Research Council. Retrieved from https://ags.aer.ca/atlas-the-western-canada-sedimentary-basin/chapter-5-precambrian-basement

Chacko, T., De, S. K., Creaser, R. A., & Muehlenbachs, K. (2000). Tectonic setting of the Taltson magmatic zone at 1.9-2.0 Ga: a granitoid-based perspective. *Canadian Journal of Earth Sciences*, *37*(11), 1597–1609. https://doi.org/10.1139/e00-029

Chan, J. (2013). *Subsurface geophysical characterization of the crystalline Canadian Shield in Northeastern Alberta: implications for geothermal development*. *Master thesis*. Edmonton: University of Alberta. https://doi.org/10.7939/R3BR8MQ6B

Chan, J., & Schmitt, D. R. (2015a). Elastic anisotropy of a metamorphic rock sample of the Canadian Shield in Northeastern Alberta. *Rock Mechanics and Rock Engineering*, *48*(4), 1369–1385. https://doi.org/10.1007/s00603-014-0664-z

Chan, J., & Schmitt, D. R. (2015b). Initial seismic observations from a deep borehole drilled into the Canadian Shield in northeast Alberta. *International Journal of Earth Sciences*, *104*(6), 1549–1562. https://doi.org/10.1007/s00531-014-1110-x

Chen, S. T. (1988). Shear-wave logging with dipole sources. *Geophysics*, *53*(5), 659–667. https://doi.org/10.1190/1.1442500

Chen, Y., Gu, Y. J., Currie, C. A., Johnston, S. T., Hung, S. H., Schaeffer, A. J., & Audet, P. (2019). Seismic evidence for a mantle suture and implications for the origin of the Canadian Cordillera. *Nature Communications*, *10*(1), 1–10. https://doi.org/10.1038/s41467-019-09804-8

Cho, J. W., Kim, H., Jeon, S., & Min, K. B. (2012). Deformation and strength anisotropy of Asan gneiss, Boryeong shale, and Yeoncheon schist. *International Journal of Rock Mechanics and Mining Sciences*, *50*, 158–169. https://doi.org/10.1016/j.ijrmms.2011.12.004

Christensen, N. I., & Stanley, D. (2003). Seismic velocities and densities of rocks. In W. H. K. Lee, H. Kanamori, P. C. Jennings, & C. Kisslinger (Eds.), *International Geophysics* (Vol. 81B, pp. 1587–1594). Academic Press. https://doi.org/10.1016/S0074-6142(03)80278-4

Condon, K. J., Sone, H., Wang, H. F., Ajo-Franklin, J., Baumgartner, T., Beckers, K., et al. (2020). Low static shear modulus along foliation and its influence on the elastic and strength anisotropy of Poorman Schist Rocks, Homestake Mine, South Dakota. *Rock Mechanics and Rock Engineering*, *53*(11), 5257–5281. https://doi.org/10.1007/s00603-020-02182-4

Donath, F. A. (1961). Experimental study of shear failure in ansitropic rocks. *Geological Society of America Bulletin*, *72*(6), 985–989. https://doi.org/10.1130/0016-7606(1961)72[985:ESOSFI]2.0.CO;2

Droessler, M., & de Pencier, J. (2020). *Preliminary assessment of enhanced geothermal systems for Oil Sands mining operations*. Edmonton: Canada's Oil Sands Innovation Alliance. Retrieved from https://cosia.ca/sites/default/files/attachments/C528 Final Report_06APR2020_FINAL.pdf

Ellefsen, K. J., Cheng, C. H., & Toksöz, M. N. (1991). Effects of anisotropy upon the normal modes in a borehole. *The Journal of the Acoustical Society of America*, *89*(6), 2597–2616. https://doi.org/10.1121/1.400699

Ellsworth, W. L., Llenos, A. L., McGarr, A. F., Michael, A. J., Rubinstein, J. L., Mueller, C. S., et al. (2015). Increasing seismicity in the U. S. midcontinent: Implications for earthquake hazard. *The Leading Edge*, *34*(6), 618–626. https://doi.org/10.1190/tle34060618.1

Emmermann, R., & Lauterjung, J. (1997). The German continental deep drilling program KTB: overview and major results. *Journal of Geophysical Research: Solid Earth*, *102*(B8), 18179–18201. https://doi.org/10.1029/96JB03945

Fordjor, C. K., Bell, J. S., & Gough, D. I. (1983). Breakouts in Alberta and stress in the North American plate. *Canadian Journal of Earth Sciences*, *20*(9), 1445–1455.

https://doi.org/10.1139/e83-130

Goertz-Allmann, B. P., Gibbons, S. J., Oye, V., Bauer, R., & Will, R. (2017). Characterization of induced seismicity patterns derived from internal structure in event clusters. *Journal of Geophysical Research: Solid Earth*, *122*(5), 3875–3894. https://doi.org/10.1002/2016JB013731

Goswami, D., Roy, S., & Akkiraju, V. V. (2019). Delineation of damage zones from 3 km downhole geophysical logs in the Koyna Seismogenic Zone , Western India. *Journal of Geophysical Research: Solid Earth*, *124*(6), 6101–6120. https://doi.org/10.1029/2018JB017257

Goswami, D., Hazarika, P., & Roy, S. (2020). In situ stress orientation from 3 km borehole image logs in the Koyna Seismogenic Zone, western India: implications for transitional faulting environment. *Tectonics*, *39*(1), e2019TC005647. https://doi.org/10.1029/2019TC005647

Grobe, M. (2000). *Distribution and thickness of salt within the devonian Elk Point group, Western Canada Sedimentary Basin*. Edmonton: Alberta Energy and Utilities Board. Retrieved from https://static.ags.aer.ca/files/document/ESR/ESR_2000_02.pdf

Guglielmi, Y., Cook, P., Soom, F., Schoenball, M., Dobson, P., & Kneafsey, T. (2021). In situ continuous monitoring of borehole displacements induced by stimulated hydrofracture growth. *Geophysical Research Letters*, *48*(4), e2020GL090782. https://doi.org/10.1029/2020GL090782

Haimson, B. C. (1978). Crustal stress in the Michigan Basin. *Journal of Geophysical Research*, *83*(B12), 5857–5863. https://doi.org/10.1029/JB083iB12p05857

Haimson, B. C., & Doe, T. W. (1983). State of stress, permeability, and fractures in the Precambrian granite of northern Illinois. *Journal of Geophysical Research*, *88*(B9), 7355–7371. https://doi.org/10.1029/JB088iB09p07355

Harvey, S., O'Brien, S., Minisini, S., Oates, S., & Braim, M. (2021). Quest CCS facility: microseismic system monitoring and observations. Paper presented at *15th International Conference on Greenhouse Gas Control Technologies*. Abu Dhabi, UAE.

He, X., Hu, H., & Guan, W. (2010). Fast and slow flexural waves in a deviated borehole in homogeneous and layered anisotropic formations. *Geophysical Journal International*, *181*(1), 417–426. https://doi.org/10.1111/j.1365-246X.2010.04503.x

Healy, J. H., Rubey, W. W., Griggs, D. T., & Raleigh, C. B. (1968). The Denver earthquakes. *Science*, *161*(3848), 1301–1310. https://doi.org/10.1126/science.161.3848.1301

Heidbach, O., Rajabi, M., Cui, X., Fuchs, K., Müller, B., Reinecker, J., et al. (2018). The world stress map database release 2016: crustal stress pattern across scales. *Tectonophysics*, *744*, 484–498. https://doi.org/10.1016/j.tecto.2018.07.007

Huber, K., Fuchs, K., Palmer, J., Roth, F., Khakhaev, B. N., Van-Kin, L. E., et al. (1997). Analysis of borehole televiewer measurements in the Vorotilov drillhole, Russia - first results. *Tectonophysics*, *275*(1–3), 261–272. https://doi.org/10.1016/S0040-1951(97)00031-0

Jaeger, J. C. (1960). Shear failure of anistropic rocks. *Geological Magazine*, *97*(1), 65–72.

https://doi.org/10.1017/S0016756800061100

Jaeger, J. C., Cook, N. G., & Zimmerman, R. W. (2007). *Fundamentals of rock mechanics*. *Blackwell publishing* (4th ed.). Blackwell publishing.

Jordan, T., Fulton, P., Tester, J., Bruhn, D., Asanuma, H., Harms, U., et al. (2020). Borehole research in New York State can advance utilization of low-enthalpy geothermal energy, management of potential risks, and understanding of deep sedimentary and crystalline geologic systems. *Scientific Drilling*, *28*, 75–91. https://doi.org/10.5194/sd-28-75-2020

Juhlin, C., Sturkell, E., Ebbestad, J. O. R., Lehnert, O., Högström, A. E. S., & Meinhold, G. (2012). A new interpretation of the sedimentary cover in the western Siljan Ring area, central Sweden, based on seismic data. *Tectonophysics*, *580*, 88–99. https://doi.org/10.1016/j.tecto.2012.08.040

Keranen, K. M., Weingarten, M., Abers, G. A., Bekins, B. A., & Ge, S. (2014). Sharp increase in central Oklahoma seismicity since 2008 induced by massive wastewater injection. *Science*, *345*(6195), 448–451. https://doi.org/10.1126/science.1255802

Kirsch, E. G. (1898). Die theorie der elastizitat und die bedurfnisse der festigkeitslehre. *Zeitschrift Des Vereines Deutscher Ingenieure*, *42*(29), 797–807.

Kolawole, F., Johnston, C. S., Morgan, C. B., Chang, J. C., Marfurt, K. J., Lockner, D. A., et al. (2019). The susceptibility of Oklahoma's basement to seismic reactivation. *Nature Geoscience*, *12*(10), 839–844. https://doi.org/10.1038/s41561-019-0440-5

Kozlovsky, Y. A. (1987). *The superdeep well of the Kola Peninsula*. Berlin: Springer-Verlag. https://doi.org/10.1007/978-3-642-71137-4

Kreemer, C., Blewitt, G., & Klein, E. C. (2014). A geodetic plate motion and global strain rate model. *Geochemistry, Geophysics, Geosystems*, *15*(10), 3849–3889. https://doi.org/10.1002/2014GC005407

Lee, H., Ong, S. H., Azeemuddin, M., & Goodman, H. (2012). A wellbore stability model for formations with anisotropic rock strengths. *Journal of Petroleum Science and Engineering*, *96–97*, 109–119. https://doi.org/10.1016/j.petrol.2012.08.010

Lee, H., Chang, C., Ong, S. H., & Song, I. (2013). Effect of anisotropic borehole wall failures when estimating in situ stresses: a case study in the Nankai accretionary wedge. *Marine and Petroleum Geology*, *48*, 411–422. https://doi.org/10.1016/j.marpetgeo.2013.09.004

Lekhnitskij, S. G. (1963). *Theory of the elasticity of anisotropic body*. San Francisco: Holden-Day.

Li, W., Schmitt, D. R., Tibbo, M., & Zou, C. (2019). A program to calculate the state of stress in the vicinity of an inclined borehole through an anisotropic rock formation. *Geophysics, 84*(5), F103–F118. https://doi.org/10.1190/geo2018-0097.1

Lin, W., Yeh, E.-C., Ito, H., Hung, J.-H., Hirono, T., Soh, W., et al. (2007). Current stress state and principal stress rotations in the vicinity of the Chelungpu fault induced by the 1999 Chi-Chi, Taiwan, earthquake. *Geophysical Research Letters*, *34*(16), L16307. https://doi.org/10.1029/2007GL030515

Lund, B., & Zoback, M. D. (1999). Orientation and magnitude of in situ stress to 6.5 km depth in the Baltic Shield. *International Journal of Rock Mechanics and Mining Sciences*, *36*(2), 169–190. https://doi.org/10.1016/S0148-9062(98)00183-1

Majorowicz, J., Chan, J., Crowell, J., Gosnold, W., Heaman, L. M., Kück, J., et al. (2014). The first deep heat flow determination in crystalline basement rocks beneath the Western Canadian Sedimentary Basin. *Geophysical Journal International*, *197*(2), 731–747. https://doi.org/10.1093/gji/ggu065

Marcia, K., & Scott, J. (2021). Horizontal drilling for geothermal power generation in the Williston Basin (Canada). Paper presented at *Geoconvention*. Virtual.

Marshak, S., Domrois, S., Abert, C., Larson, T., Pavlis, G., Hamburger, M., et al. (2017). The basement revealed: Tectonic insight from a digital elevation model of the Great Unconformity, USA cratonic platform. *Geology*, *45*(5), 391–394. https://doi.org/10.1130/G38875.1

Martin, C. D., Read, R. S., & Martino, J. B. (1997). Observations of brittle failure around a circular test tunnel. *International Journal of Rock Mechanics and Mining Sciences*, *34*(7), 1065–1073. https://doi.org/10.1016/S1365-1609(97)90200-8

Massiot, C., Célérier, B., Doan, M. L., Little, T. A., Townend, J., McNamara, D. D., et al. (2018). The Alpine fault hangingwall viewed from within: structural analysis of ultrasonic image logs in the DFDP-2B borehole, New Zealand. *Geochemistry, Geophysics, Geosystems*, *19*(8), 2492–2515. https://doi.org/10.1029/2017GC007368

Mastin, L. (1988). Effect of borehole deviation on breakout orientations. *Journal of Geophysical Research: Solid Earth*, *93*(B8), 9187–9195. https://doi.org/10.1029/JB093iB08p09187

McCabe, W. M., & Koerner, R. M. (1975). High pressure shear strength investigation of an anisotropic mica schist rock. *International Journal of Rock Mechanics and Mining Sciences and & Geomechanics Abstracts*, *12*(8), 219–228. https://doi.org/10.1016/0148-9062(75)91402-3

McMechan, M. E., Root, K. G., Simony, P. S., & Pattison, D. R. M. (2020). Nailed to the craton: stratigraphic continuity across the southeastern Canadian Cordillera with tectonic implications for ribbon continent models. *Geology*, *49*(1), 101–105. https://doi.org/10.1130/G48060.1

McNicoll, V. J., Thériault, R. J., & McDonough, M. R. (2000). Taltson basement gneissic rocks: U-Pb and Nd isotopic constraints on the basement to the Paleoproterozoic Taltson magmatic zone, northeastern Alberta. *Canadian Journal of Earth Sciences*, *37*(11), 1575–1596. https://doi.org/10.1139/e00-034

Moeck, I., Kwiatek, G., & Zimmermann, G. (2009). Slip tendency analysis, fault reactivation potential and induced seismicity in a deep geothermal reservoir. *Journal of Structural Geology*, *31*(10), 1174–1182. https://doi.org/10.1016/j.jsg.2009.06.012

Morin, M. L. (2017). *Natural and drilling induced fractures in the Grosmont Formation, Alberta: implications for the state of stress*. *Master thesis*. Edmonton: University of Alberta. https://doi.org/10.7939/R3B56DJ60

Nasseri, M. H. B., Rao, K. S., & Ramamurthy, T. (2003). Anisotropic strength and deformation behavior of Himalayan schists. *International Journal of Rock Mechanics and Mining Sciences*, *40*(1), 3–23. https://doi.org/10.1016/S1365-1609(02)00103-X

Ong, O. N., Schmitt, D. R., Kofman, R. S., & Haug, K. (2016). Static and dynamic pressure sensitivity anisotropy of a calcareous shale. *Geophysical Prospecting*, *64*(4), 875–897. https://doi.org/10.1111/1365-2478.12403

Peters, S. E., & Gaines, R. R. (2012). Formation of the "Great Unconformity" as a trigger for the Cambrian explosion. *Nature*, *484*(7394), 363–366. https://doi.org/10.1038/nature10969

Pham, C., Chang, C., Jang, Y., Kutty, A., & Jeong, J. (2020). Effect of faults and rock physical properties on in situ stress within highly heterogeneous carbonate reservoirs. *Journal of Petroleum Science and Engineering*, *185*, 106601. https://doi.org/10.1016/j.petrol.2019.106601

Pierdominici, S., & Ask, M. (2021). Rock strength and time dependent deformation of borehole breakouts in the ICDP Outokumpu deep borehole. *EGU General Assembly*, EGU21-6259. https://doi.org/10.5194/egusphere-egu21-6259

Pierdominici, S., Mariucci, M. T., & Montone, P. (2011). A study to constrain the geometry of an active fault in southern Italy through borehole breakouts and downhole logs. *Journal of Geodynamics*, *52*(3–4), 279–289. https://doi.org/10.1016/j.jog.2011.02.006

Plumb, R. A., & Hickman, S. H. (1985). Stress-induced borehole elongation: a comparison between the four-arm dipmeter and the borehole televiewer in the Auburn Geothermal Well. *Journal of Geophysical Research: Solid Earth*, *90*(B7), 5513–5521. https://doi.org/10.1029/JB090iB07p05513

Price, R. A. (1994). Cordilleran tectonics and the evolution of the Western Canada Sedimentary Basin. In G. D. Mossop & I. Shetsen (Eds.), *Geological atlas of the Western Canada sedimentary basin* (pp. 13–24). Canadian Society of Petroleum Geologists and Alberta Research Council. Retrieved from https://ags.aer.ca/atlas-the-western-canada-sedimentary-basin/chapter-2-cordilleran-tectonics

Qian, W., & Pedersen, L. B. (1991). Inversion of borehole breakout orientation data. *Journal of Geophysical Research: Solid Earth*, *96*(B12), 20093–20107. https://doi.org/10.1029/91JB01627

Rajabi, M., Tingay, M., & Heidbach, O. (2016). The present-day stress field of New South Wales, Australia. *Australian Journal of Earth Sciences*, *63*(1), 1–21. https://doi.org/10.1080/08120099.2016.1135821

Reiter, K., & Heidbach, O. (2014). 3-D geomechanical-numerical model of the contemporary crustal stress state in the Alberta Basin (Canada). *Solid Earth*, *5*(2), 1123–1149. https://doi.org/10.5194/se-5-1123-2014

Reiter, K., Heidbach, O., Schmitt, D., Haug, K., Ziegler, M., & Moeck, I. (2014). A revised crustal stress orientation database for Canada. *Tectonophysics*, *636*, 111–124. https://doi.org/10.1016/j.tecto.2014.08.006

Röckel, T., & Lempp, C. (2003). Der spannungszustand im Norddeutschen Becken. *Erdoel Erdgas Kohle*, *119*(2), 73–80.

Ross, G. M., Parrish, R. R., Villeneuve, M. E., & Bowring, S. A. (1991). Geophysics and geochronology of the crystalline basement of the Alberta Basin, western Canada. *Canadian Journal of Earth Sciences*, *28*(4), 512–522. https://doi.org/10.1139/e91-045

Sahara, D. P., Schoenball, M., Kohl, T., & Müller, B. I. R. (2014). Impact of fracture networks on borehole breakout heterogeneities in crystalline rock. *International Journal of Rock Mechanics and Mining Sciences*, *71*, 301–309. https://doi.org/10.1016/j.ijrmms.2014.07.001

Savchenko, S. N., & Kozyrev, A. A. (2003). Current stresses in the rock mass near the Kola superdeep borehole (SG-3). *International Journal of Rock Mechanics and Mining Sciences*, *40*, 1271–1276. https://doi.org/10.1016/j.ijrmms.2003.07.008

Schijns, H., Schmitt, D. R., Heikkinen, P. J., & Kukkonen, I. T. (2012). Seismic anisotropy in the crystalline upper crust: observations and modelling from the Outokumpu scientific borehole, Finland. *Geophysical Journal International*, *189*(1), 541–553. https://doi.org/10.1111/j.1365-246X.2012.05358.x

Schmitt, D. R. (1993). Fracture statistics derived from digital ultrasonic televiewer logging. *The Journal of Canadian Petroleum Technology*, *32*(02), 34–43. https://doi.org/10.2118/93-02-02

Schmitt, D. R., Currie, C. A., & Zhang, L. (2012). Crustal stress determination from boreholes and rock cores: fundamental principles. *Tectonophysics*, *580*, 1–26. https://doi.org/10.1016/j.tecto.2012.08.029

Schmitt, D. R., Wang, W., & Chan, J. (2022). Geophysical Logging and Image Data from the Hunt Well, NE Alberta [Dataset]. *Borealis*. https://doi.org/10.5683/SP3/YYNVW8

Schoenball, M., & Davatzes, N. C. (2017). Quantifying the heterogeneity of the tectonic stress field using borehole data. *Journal of Geophysical Research: Solid Earth*, *122*(8), 6737–6756. https://doi.org/10.1002/2017JB014370

Setiawan, N. B., & Zimmerman, R. W. (2018). Wellbore breakout prediction in transversely isotropic rocks using true-triaxial failure criteria. *International Journal of Rock Mechanics and Mining Sciences*, *112*, 313–322. https://doi.org/10.1016/j.ijrmms.2018.10.033

Shamir, G., & Zoback, M. D. (1992). Stress orientation profile to 3.5 km depth near the San Andreas Fault at Cajon Pass, California. *Journal of Geophysical Research: Solid Earth*, *97*(B4), 5059–5080. https://doi.org/10.1029/91JB02959

Shen, L. W., Schmitt, D. R., & Haug, K. (2019). Quantitative constraints to the complete state of stress from the combined borehole and focal mechanism inversions: Fox Creek, Alberta. *Tectonophysics*, *764*, 110–123. https://doi.org/10.1016/j.tecto.2019.04.023

Shen, L. W., Schmitt, D. R., Wang, R., & Hauck, T. E. (2021). States of in situ stress in the Duvernay East Shale Basin and Willesden Green of Alberta, Canada: variable in situ stress states effect fault stability. *Journal of Geophysical Research: Solid Earth*, *126*(6), e2020JB021221. https://doi.org/10.1029/2020JB021221

Sinha, B. K., Norris, A. N., & Chang, S.-K. (1994). Borehole flexural modes in anisotropic formations. *Geophysics*, *59*(7), 1037–1052. https://doi.org/10.1190/1.1443660

Stork, A. L., Nixon, C. G., Hawkes, C. D., Birnie, C., White, D. J., Schmitt, D. R., & Roberts, B. (2018). Is CO2 injection at Aquistore aseismic? A combined seismological and geomechanical study of early injection operations. *International Journal of Greenhouse Gas Control*, *75*, 107–124. https://doi.org/10.1016/j.ijggc.2018.05.016

Valley, B., & Evans, K. F. (2019). Stress magnitudes in the Basel enhanced geothermal system. *International Journal of Rock Mechanics and Mining Sciences*, *118*, 1–20. https://doi.org/10.1016/j.ijrmms.2019.03.008

Vernik, L., & Zoback, M. D. (1989). Effects of rock elastic and strength properties in estimation of the state of stress at depth. Paper presented at *ISRM International Symposium* (pp. 1033–1040). Pau, France.

Vernik, L., & Zoback, M. D. (1990). Strength anisotropy in crystalline rock: implications for assessment of in situ stresses from wellbore breakouts. Paper presented at *The 31st U.S. Symposium on Rock Mechanics (USRMS)* (pp. 841–848). Golden, Colorado.

Walsh III, F. R., & Zoback, M. D. (2015). Oklahoma's recent earthquakes and saltwater disposal. *Science Advances*, *1*(5), e1500195. https://doi.org/10.1126/sciadv.1500195

Walsh, N. J. (2013). *Geochemistry and geochronology of the Precambrian basement domains in the vicinity of Fort McMurray, Alberta: a geothermal perspective*. *Master thesis*. https://doi.org/10.7939/R3ZG71

Wang, B., Sun, D., Chen, Q., Lin, W., Li, A., & Cao, H. (2020). Stress-state differences between sedimentary cover and basement of the Songliao Basin, NE China : In-situ stress measurements at 6 – 7 km depth of an ICDP Scientific Drilling borehole (SK-II). *Tectonophysics*, *777*, 228337. https://doi.org/10.1016/j.tecto.2020.228337

Wang, W., & Schmitt, D. R. (2020). Automated borehole breakout interpretation from ultrasonic imaging: application to a deep borehole drilled into the crystalline crust. Paper presented at *54th US Rock Mechanics/Geomechanics Symposium*. physical event cancelled.

Wang, W., & Schmitt, D. R. (2022). BreakOut Automatic Picking From Image Logs (BOAPFIL) [Software]. *Purdue University Research Repository*. https://doi.org/10.4231/RTAW-JW77

Wang, W., Schmitt, D. R., & Li, W. (2021). Failure pattern around the borehole in elastic and strength anisotropic rock formations [Software]. *Purdue University Research Repository*. https://doi.org/10.4231/0NWT-5Y39

Wang, W., Schmitt, D. R., & Li, W. (2022). A program to forward model the failure pattern around the wellbore in elastic and strength anisotropic rock formations. *International Journal of Rock Mechanics and Mining Sciences*, *151*, 105035. https://doi.org/10.1016/j.ijrmms.2022.105035

Weides, S. N., Moeck, I. S., Schmitt, D. R., & Majorowicz, J. A. (2014). An integrative geothermal resource assessment study for the siliciclastic Granite Wash Unit, northwestern Alberta (Canada). *Environmental Earth Sciences*, *72*(10), 4141–4154. https://doi.org/10.1007/s12665-014-3309-3

Weingarten, M., Ge, S., Godt, J. W., Bekins, B. A., & Rubinstein, J. L. (2015). High-rate injection is associated with the increase in U.S. mid-continent seismicity. *Science*, *348*(6241), 1336–1340. https://doi.org/10.1126/science.aab1345

Wenning, Q. C., Berthet, T., Ask, M., Zappone, A., Rosberg, J. E., & Almqvist, B. S. G. (2017). Image log analysis of in situ stress orientation, breakout growth, and natural geologic structures to 2.5 km depth in central Scandinavian Caledonides: Results from the COSC-1 borehole. *Journal of Geophysical Research: Solid Earth*, *122*(5), 3999–4019. https://doi.org/10.1002/2016JB013776

Williams-Stroud, S., Bauer, R., Leetaru, H., Oye, V., Stanek, F., Greenberg, S., & Langet, N. (2020). Analysis of microseismicity and reactivated fault size to assess the potential for felt events by CO2 injection in the Illinois Basin. *Bulletin of the Seismological Society of America*, *110*(5), 2188–2204. https://doi.org/10.1785/0120200112

Winkler, K. W. (1997). Acoustic evidence of mechanical damage surrounding stressed boreholes. *Geophysics*, *62*(1), 16–22. https://doi.org/10.1190/1.1444116

Wright, G. N., McMechan, M. E., Potter, D. E. G., & Holter, M. E. (1994). Structure and architecture of the Western Canada sedimentary basin. In G. D. Mossop & I. Shetsen (Eds.), *Geological atlas of the Western Canada sedimentary basin* (Vol. 4, pp. 25–40). Canadian Society of Petroleum Geologists and Alberta Research Council. Retrieved from https://ags.aer.ca/atlas-the-western-canada-sedimentary-basin/chapter-3-structure-and-architecture

Wu, H.-Y., Ma, K.-F., Zoback, M. D., Boness, N., Ito, H., Hung, J.-H., & Hickman, S. (2007). Stress orientations of Taiwan Chelungpu-Fault Drilling Project (TCDP) hole-A as observed from geophysical logs. *Geophysical Research Letters*, *34*(1), L01303. https://doi.org/10.1029/2006GL028050

Yale, D. P. (2003). Fault and stress magnitude controls on variations in the orientation of in situ stress. *Geological Society Special Publication*, *209*(1), 55–64. https://doi.org/10.1144/GSL.SP.2003.209.01.06

Zajac, B. J., & Stock, J. M. (1997). Using borehole breakouts to constrain the complete stress tensor: Results from the Sijan Deep Drilling Project and offshore Santa Maria Basin , California. *Journal of Geophysical Research: Solid Earth*, *102*(B5), 10083–10100. https://doi.org/10.1029/96JB03914

Zakharova, N. V., & Goldberg, D. S. (2014). In situ stress analysis in the northern Newark Basin: Implications for induced seismicity from CO2 injection. *Journal of Geophysical Research: Solid Earth*, *119*(3), 2362–2374. https://doi.org/10.1002/2013JB010492

Zoback, M. D., & Gorelick, S. M. (2012). Earthquake triggering and large-scale geologic storage of carbon dioxide. *Proceedings of the National Academy of Sciences of the United States of America*, *109*(26), 10164–10168. https://doi.org/10.1073/pnas.1202473109

Zoback, M. D., & Harjes, H. P. (1997). Injection-induced earthquakes and crustal stress at 9 km depth at the KTB deep drilling site, Germany. *Journal of Geophysical Research: Solid Earth*, *102*(B8), 18477–18491. https://doi.org/10.1029/96JB02814

Zoback, M. D., Barton, C. A., Brudy, M., Castillo, D. A., Finkbeiner, T., Grollimund, B. R., et al. (2003). Determination of stress orientation and magnitude in deep wells. *International Journal of Rock Mechanics and Mining Sciences*, *40*(7–8), 1049–1076. https://doi.org/10.1016/j.ijrmms.2003.07.001

References from Supporting Information

Amadei, B. (1983). *Rock anisotropy and the theory of stress measurements*. Berlin: Springer-Verlag. https://doi.org/10.1007/978-3-642-82040-3

Azzola, J., Valley, B., Schmittbuhl, J., & Genter, A. (2019). Stress characterization and temporal evolution of borehole failure at the Rittershoffen geothermal project. *Solid Earth*, *10*(4), 1155–1180. https://doi.org/10.5194/se-10-1155-2019

Bell, J. S., & Gough, D. I. (1979). Northeast-southwest compressive stress in Alberta evidence from oil wells. *Earth and Planetary Science Letters*, *45*(2), 475–482. https://doi.org/10.1016/0012-821X(79)90146-8

Boness, N. L., & Zoback, M. D. (2004). Stress-induced seismic velocity anisotropy and physical properties in the SAFOD Pilot Hole in Parkfield, CA. *Geophysical Research Letters*, *31*(15), L15S17. https://doi.org/10.1029/2003GL019020

Boness, N. L., & Zoback, M. D. (2006). A multiscale study of the mechanisms controlling shear velocity anisotropy in the San Andreas Fault Observatory at depth. *Geophysics*, *71*(5), F131–F146. https://doi.org/10.1190/1.2231107

Brudy, M., & Zoback, M. D. (1999). Drilling-induced tensile wall-fractures: Implications for determination of in-situ stress orientation and magnitude. *International Journal of Rock Mechanics and Mining Sciences*, *36*(2), 191–215. https://doi.org/10.1016/S0148-9062(98)00182-X

Chan, J. (2013). *Subsurface geophysical characterization of the crystalline Canadian Shield in Northeastern Alberta: implications for geothermal development*. *Master thesis*. Edmonton: University of Alberta. https://doi.org/10.7939/R3BR8MQ6B

Chan, J., & Schmitt, D. R. (2015). Initial seismic observations from a deep borehole drilled into the Canadian Shield in northeast Alberta. *International Journal of Earth Sciences*, *104*(6), 1549–1562. https://doi.org/10.1007/s00531-014-1110-x

Fang, X., Cheng, A., & Fehler, M. C. (2015). Investigation of borehole cross-dipole flexural dispersion crossover through numerical modeling. *Geophysics*, *80*(1), D75–D88. https://doi.org/10.1190/geo2014-0196.1

Goswami, D., Roy, S., & Akkiraju, V. V. (2019). Delineation of damage zones from 3 km downhole geophysical logs in the Koyna Seismogenic Zone , Western India. *Journal of Geophysical Research: Solid Earth*, *124*(6), 6101–6120. https://doi.org/10.1029/2018JB017257

Goswami, D., Hazarika, P., & Roy, S. (2020). In situ stress orientation from 3 km borehole image logs in the Koyna Seismogenic Zone, western India: implications for transitional faulting environment. *Tectonics*, *39*(1), e2019TC005647. https://doi.org/10.1029/2019TC005647

Gough, D. I., & Bell, J. S. (1982). Stress orientations from borehole wall fractures with examples from Colorado, east Texas, and northern Canada. *Canadian Journal of Earth Sciences*, *19*(7), 1358–1370. https://doi.org/10.1139/e82-118

Hiramatsu, Y., & Oka, Y. (1962). Analysis of stress around a circular shaft or drift excavated in ground in a three dimensional stress state. *Journal of Mining and Metallurgy Institute of Japan*, *78*, 93–98.

Iturrino, G. J., Goldberg, D., Glassman, H., Patterson, D., Sun, Y. F., Guerin, G., & Haggas, S. (2005). Shear-wave anisotropy from dipole shear logs in oceanic crustal environments. *Geological Society Special Publication*, *240*, 117–131. https://doi.org/10.1144/GSL.SP.2005.240.01.10

Kerkela, S., & Stock, J. M. (1996). Compression directions north of the San Fernando Valley determined from borehole breakouts. *Geophysical Research Letters*, *23*(23), 3365–3368. https://doi.org/10.1029/96GL03054

Kirsch, E. G. (1898). Die theorie der elastizitat und die bedurfnisse der festigkeitslehre. *Zeitschrift Des Vereines Deutscher Ingenieure*, *42*(29), 797–807.

Majorowicz, J., Chan, J., Crowell, J., Gosnold, W., Heaman, L. M., Kück, J., et al. (2014). The first deep heat flow determination in crystalline basement rocks beneath the Western Canadian Sedimentary Basin. *Geophysical Journal International*, *197*(2), 731–747. https://doi.org/10.1093/gji/ggu065

Morin, M. L. (2017). *Natural and drilling induced fractures in the Grosmont Formation, Alberta: implications for the state of stress*. *Master thesis*. Edmonton: University of Alberta. https://doi.org/10.7939/R3B56DJ60

Schmitt, D. R., Currie, C. A., & Zhang, L. (2012). Crustal stress determination from boreholes and rock cores: fundamental principles. *Tectonophysics*, *580*, 1–26. https://doi.org/10.1016/j.tecto.2012.08.029

Sinha, B. K., Norris, A. N., & Chang, S.-K. (1994). Borehole flexural modes in anisotropic formations. *Geophysics*, *59*(7), 1037–1052. https://doi.org/10.1190/1.1443660

Stork, A. L., Nixon, C. G., Hawkes, C. D., Birnie, C., White, D. J., Schmitt, D. R., & Roberts, B. (2018). Is CO2 injection at Aquistore aseismic? A combined seismological and geomechanical study of early injection operations. *International Journal of Greenhouse Gas Control*, *75*, 107–124. https://doi.org/10.1016/j.ijggc.2018.05.016

Thomsen, L. (1986). Weak elastic anisotropy. *Geophysics*, *51*(10), 1954–1966. https://doi.org/https://doi.org/10.1190/1.1442051

Winkler, K. W. (1997). Acoustic evidence of mechanical damage surrounding stressed boreholes. *Geophysics*, *62*(1), 16–22. https://doi.org/10.1190/1.1444116

Wu, H.-Y., Ma, K.-F., Zoback, M. D., Boness, N., Ito, H., Hung, J.-H., & Hickman, S. (2007). Stress orientations of Taiwan Chelungpu-Fault Drilling Project (TCDP) hole-A as observed from geophysical logs. *Geophysical Research Letters*, *34*(1), L01303. https://doi.org/10.1029/2006GL028050

Wu, Y.-H., Yeh, E.-C., Dong, J.-J., Kuo, L.-W., Hsu, J.-Y., & Hung, J.-H. (2008). Core-log integration studies in hole-A of Taiwan Chelungpu-fault Drilling Project. *Geophysical Journal International*, *174*(3), 949–965. https://doi.org/10.1111/j.1365-246X.2008.03841.x

Zoback, M. D., Barton, C. A., Brudy, M., Castillo, D. A., Finkbeiner, T., Grollimund, B. R., et al. (2003). Determination of stress orientation and magnitude in deep wells. *International Journal of Rock Mechanics and Mining Sciences*, *40*(7–8), 1049–1076. https://doi.org/10.1016/j.ijrmms.2003.07.001

Journal of Geophysical Research: Solid Earth

Supporting Information for

Heterogeneity versus Anisotropy and the State of Stress in Stable Cratons: Observations from a Deep Borehole of Opportunity in Northeastern Alberta, Canada

Wenjing Wang[1*], Douglas R. Schmitt[1,3], Judith Chan[2,3]

[1] Earth, Atmospheric, and Planetary Sciences Department, Purdue University, West Lafayette, Indiana, USA, 47907

[2] Earth Signal Processing Ltd., Calgary, Alberta, Canada, T2P 2X6

[3] Formerly, Department of Physics, University of Alberta, Edmonton, Alberta, Canada, T6G 2E1

* Corresponding author: Wenjing Wang (wang4084@purdue.edu)

Contents of this file

Text S1 to S4
Figures S1 to S8
Tables S1 to S3

Introduction

This supporting information provides details on materials introduced in the main text.

Text S1. Data Sources for Figure 1

A variety of data sources were used to construct Figure 1.

1.1 World Stress Map Data: These were obtained from a limited search at http://www.world-stress-map.org/casmo/ over latitudes from 58°N to 61°N and longitudes from -95°E to -121°E with the data saved as the text option on November 21, 2021. Stress directions provided by breakouts (BO) or drilling induced tensile fractures (DITF) were included in the map.

1.2 Saleski Pilot Project: An average of the directions of DITFs observed in an ensemble of vertical boreholes drilled into the Devonian Grosmont Formation for hydrocarbon production at depths between 300m and 400m were reported by Morin (2017). The center of the ~15 km X 15 km industrial site, referred to as the Saleski Pilot Project, is at 56.370403°N, -112.942834°W and it lies 91 km WSW of the Hunt Well at 56.75955°N, -111.55472°W.

1.3 Aquistore CO_2 Sequestration Project: Interpretations of the Aquistore Observation Well image logs at 49.023°N, -103.085°W were described in Stork et al. (2018).

1.4 Earthquake Epicenters: Epicentral locations were downloaded from the USGS *(https://earthquake.usgs.gov/earthquakes/search/)* for all events of magnitude > 2.5 M_b with delimited geographical locations over latitudes from 58°N to 61°N and longitudes from -95°E to -121°E, and with dates from 1/1/1980 to 11/20/2021. The data downloaded as text option were selected on November 21, 2021.

1.5 Relative Plate Motions: The relative plate motion was found for the location 55°N, -110°W using the online calculator https://www.unavco.org/software/geodetic-utilities/plate-motion-calculator/plate-motion-calculator.html under the GSRM v2.1 model on 11/20/2021.

Text S2. Descriptions of Logging Instruments and Interpretation Criteria

As many readers are not familiar with the tools and methods of geophysical loggings, and this information can be difficult to find, we provide here a brief overview of the different instruments employed and the procedures used in their interpretations.

2.1 Stress around the Wellbore

S_V can be calculated by integrating the weight of rocks from the surface to the depth of interest, shown in Eq. (S1), where g is the gravitational acceleration constant and ρ(z) is the density at the depth z.

$$S_v = \int_0^z \rho(z) g dz \tag{S1}$$

Analyses of BOs (e.g., Gough & Bell, 1982) or DITFs (e.g., Brudy & Zoback, 1999) from caliper and image logs nominally indicate stress directions. Various models exist to describe the stress concentrations for different levels of complexity starting with Kirsch (1898) solutions for a hole in a thin plate to more elaborated 3D descriptions for arbitrarily aligned boreholes by Hiramatsu and Oka (1962) in isotropic and Amadei (1983) in anisotropic rock masses. Principles of extracting stress information from drilling induced failure patterns typically often rely on the Kirsch equations (1898) that provide analytical solutions for stress distribution around a hole in a linear elastic isotropic infinite 2D plate subjected to far-field stresses. When applied in the drilling of a vertical borehole whose axis is aligned with S_V, the effective stresses immediately at the borehole wall in a cylindrical coordinate system are shown in Eq. (S2-S4):

$$\sigma_{rr} = P_w - P_p \tag{S2}$$

$$\sigma_{\theta\theta} = S_H + S_h - 2(S_H - S_h)cos2\theta - P_w - P_p \tag{S3}$$

$$\sigma_{zz} = S_v - 2\nu(S_H - S_h)cos2\theta - P_p \tag{S4}$$

where σ_{rr}, $\sigma_{\theta\theta}$ and σ_{zz} are the Terzaghi effective radial, hoop (circumferential), and axial stresses governing failure with respect to the borehole; θ is the angle measured from the S_H direction; P_w is the fluid pressure in the borehole (i.e., mud pressure); P_p is the pore pressure in the formation, and υ is Poisson's ratio.

2.2 Caliper Measurements

2.2.1 Fullbore Formation Microimager FMI™ (Schlumberger): This instrument was employed in the 1994 and 2003 surveys. Data from this instrument include both high resolution images based on cm-scale variations in electrical conductivity along the borehole and oriented caliper measurements of the borehole diameter in two directions. Details of the physics of this measurement and the geometry of the tool may be found from Schlumberger brochure SMP-5822 at https://www.slb.com/-/media/files/fe/brochure/fmi-br.ashx (accessed December 11, 2021). The orientation of the tool, referred as P1AZ (Pad 1 Azimuth in Horizontal Plane), is provided by magnetometers by correcting to the true north. At the time of measurements, the caliper values came from the extension radius of the four opened electrode pads. The width of the tool assembly may prevent the determination of the maximum borehole elongation if the pads are larger than the breakout.

2.2.2 ICDP Operational Support Group Dipmeter: This instrument was employed in the 2011 survey from 1000 to 1873 m by the Operational Support Group of the International Continental Scientific Drilling program (ICDP-OSG) from the GeoforshungZentrum (GFZ) Potsdam. It is a standard oriented 4-arm caliper with an electrode-bearing pad (34.5 X 79.5 mm) mounted to each caliper arm. The resolution of the caliper is 1 mm. Borehole enlargements wider than 35 mm can be detected while the maximum reading cannot exceed 250 mm. Mature and wide breakouts will lock a pair of pads inside, stopping the tool rotation that is forced by the torque of the logging cable.

2.2.3 Powered Position Calipers PPC™ (Schlumberger): This tool was employed in conjunction with the ultrasonic imaging and dipole shear sonic runs in the 2013 sessions. This is a 4-arm caliper tool in which the arms actively push against the borehole wall to allow for accurate determinations of the widths of the two borehole axes. The width of the arms on this tool allows for it to extend fully into the breakouts. More information on this instrument may be found at https://www.slb.com/-/media/files/fe/product-sheet/ppc-ps (accessed December 11, 2021).

2.2.4 Breakout Interpretation Criteria: Criteria for determining breakouts from caliper logs are modified from those provided by Kerkela and Stock (1996) as follows:

a) The smaller caliper measurement must be within 95%-105% of the bit size.

b) The difference between two caliper measurements is greater than 10 mm.

c) The Pad 1 azimuth (P1AZ) does not change dramatically, that is, the change should be less than 1° over 1 m and P1AZ must be nearly constant for at least 3 m along the borehole.

The first criterion excludes the possibility of identifying washouts as breakouts. The second and third criteria ensure the breakouts identified are relatively large and long, which prohibit us from mistaking the roughness of the wellbore wall as breakouts. The third criterion ensures the tool is locked in the breakout due to the friction between pads and elongated walls. Further, because the Hunt well is nearly vertical, we did not need to worry about mistaking a key seat as a breakout since the spalling along the low side of the borehole is unlikely.

Along undamaged and in-gage sections of a borehole, the cross section is circular with C1 = C2 = BS: the nominal drill bit diameter. In this situation, the wireline torsion typically forces the tool to rotate as it rises during logging so that P1AZ shows no preferential direction. When present, however, uniformly oriented BO ruts trap one caliper arm pair with P1AZ remaining constant and at the same time, either C1 or C2 remains in gage while the diameter of the other arm exceeds BS (Bell & Gough, 1979), but to find α_H from P1AZ, one must consider which arm pair is most extended.

Breakouts will be identified if caliper logs meet the above criteria. In order to get the breakout azimuth, we rely on the tool direction information provided by P1AZ. Calipers measured by two sets of in line pads, pad 1 - pad 3 and pad 2 - pad 4, are denoted as C1 and C2 respectively. If C2 is larger than C1, because P1AZ refers to the pad 1 azimuth, we need to add 90° to represent the breakout direction (longer caliper direction). Otherwise, P1AZ is the same as the breakout direction, which represents the azimuth of the minimum horizontal stress based on Kirsch (1898) equations.

2.3 Borehole Wall Imaging

2.3.1 Fullbore Formation Micromager FMI™ (Schlumberger): The calipers attached to this instrument were described above. In addition, the image data from this instrument consists of high-resolution images based on cm-scale variations in electrical conductivity along the borehole wall. Essentially, the caliper arms on the tool push 4 pads containing 192 button electrodes against the wall rock with the response from these measured continuously as the tool is pulled up along the borehole. Reorganization of these responses forms an image of the local variations in electrical conductivity that may then be interpreted. The image is only provided beneath the zones that the electrodes cover, and in larger diameter boreholes this coverage is incomplete, leaving gaps between strips with no data as shown, for example, in Figure 8. This image is oriented in conjunction with the calipers using onboard magnetometers and accelerometers. Resistivity contrasts in FMI logs enable us to detect structural features, rock textures and drilling-induced features.

2.3.2 Ultrasonic Borehole Imager UBI™ (Schlumberger): This instrument was employed in 2013. Ultrasonic imaging tools use a rotating ultrasonic transducer that transmits and receives ultrasonic pulses outward to and reflected from the borehole wall rock. The transducer typically sends a pulse every 2° in azimuth as it rotates, collecting at each point the waveform amplitude and transit time; as such it provides a nearly continuous measure of these attributes around the borehole circumference. The waveform amplitude depends on the relative elastic impedance between the rock and the borehole fluid. Alternatively, the ultrasonic pulse may be scattered by rugose sections on the borehole wall and will be weakened or even not be recorded. The transit time can be easily converted to the borehole radius if the fluid sound speed is known. Two image logs, organized according to depth and azimuth, are further oriented from magnetometer and accelerometer sensors. These oriented images with travel time and amplitude contrasts may be used to measure the azimuths of breakouts or drilling induced tensile fractures and the orientations of planar features such as fractures, sedimentary beds, and foliation planes. Specifically, breakouts result in the elongation of the wellbore and therefore, the emitted ultrasonic pulse must travel a longer distance or it may not return to be recorded as the reflected beam may not intersect the borehole wall surface, normally causing increased travel time and decreased or even vanished amplitude. Further technical information on the tool used may be found at https://www.slb.com/-/media/files/fe/brochure/ubi-br.ashx (accessed December 11, 2021) or https://brgvm17.ldeo.columbia.edu/research/technology/schlumberger-wireline-tools/ultrasonic-borehole-imager-ubi/ (accessed December 11, 2021).

Image processing of image logs was performed using the WellCAD™ 5.3 (Advanced Logic Technology, Luxembourg). The preprocessing steps are as follows:

a. Orient image logs to true north using Pad 1 Azimuth in Plane Orthogonal to Tool Axis (P1NO).

b. Apply a despiking filter to image logs with 80% cutoff high and 20% cutoff low in a 3 X 3 points filter window.

c. Dynamic normalization with a 20 cm-height sliding window to enhance the local contrast using a histogram normalization.

Two types of low-quality images were excluded before interpreting drilling induced failures. The first type of low-quality images is caused by the local magnetic field variation. Image logs depend largely on the magnetometers and accelerometers/inclinometers to orient to the true geographic direction. If the magnetic field varies, the correction from P1NO to the true north direction will be erroneous. Therefore, whenever there is a magnetic field inclination or intensity anomaly, the corresponding depth was left out to improve the image quality. The other type of low-quality images is due to the signal loss represented by white patches existing in image logs. The signal loss is mostly caused by a wide wellbore diameter due to large breakouts or major faults (Azzola et al., 2019). The sonic beam energy will be strongly scattered when a wellbore diameter is rather large, and it is difficult to see the reflected echoes in UBI logs.

After excluding the above-mentioned low-quality images, ultrasonic image logs were examined every 20 cm vertically without overlapping to find drilling induced failures. Breakouts are represented by a pair of 180°-separated wide zones with smaller amplitudes and longer travel times of the reflected echo compared to the original wellbore radius whereas drilling induced tensile fractures (DITFs) are narrow. The azimuth of drilling induced failures at each 20 cm-depth interval was selected to be the median and was discarded if drilling induced failures were shorter than 20 cm. Breakout width and azimuth are illustrated in Figure 4. In the image interpretation, the breakout width was marked by the furthest extent of failure zones and the breakout azimuth was represented by the azimuth of the middle point of failure zones. The width determination of DITFs is not necessary since it is narrow.

2.3.3 Dipole Shear Sonic Imager DSI^{TM} (Schlumberger): This tool was run in 2013. It contains one omnidirectional monopole transmitter and two pairs of orthogonally oriented unidirectional dipole transmitters. The pulsed waveforms from these are received by an array of hydrophones, which provides an ensemble of waveforms that are variously processed, yielding the monopole P- or S-wave speeds or the crossed-dipole fast and slow S-wave speeds. Additional details on the operation of this tool may be found at https://brgvm17.ldeo.columbia.edu/research/technology/schlumberger-wireline-tools/dipole-sonic-imager-tool-dsi-2/ (accessed December 11, 2021) or at https://www.slb.com/-/media/files/fe/product-sheet/dsi-ps.ashx (accessed December 11, 2021).

Dispersion curves provide the evidence of formation anisotropy. Slowness of the fast and slow dipole flexural waves overlaps if the formation is isotropic, or the wellbore is aligned with the symmetric axis of the transverse isotropic formation (Figure S1a). In these two cases, there is no shear wave speed difference for all propagation directions. However, slowness of the fast and slow dipole flexural waves separates and runs roughly parallel to each other if the formation is intrinsically anisotropic and the wellbore axis is at an angle to the formation symmetric axis. In this scenario, the polarized shear wave travels faster along the direction parallel to the mineral alignment compared with the direction perpendicular to that (Figure S1b). Lastly, if the anisotropy is stress induced due to the nonlinear response between stress and strain for the rock, then the slowness of the fast and slow dipole flexural waves has a crossover (Sinha et al., 1994; Winkler, 1997), shown in Figure S1c. Lower flexural wave frequencies are more sensitive to the originally far-field stresses while high frequencies are more sensitive to the near-borehole stresses, which are a reverse of the originally far-field stresses due to the stress concentration around the wellbore. Fang et al. (2015), however, discussed some issues with the interpretation of the crossover curve based on the numerical modelling that includes borehole geometry.

Boness and Zoback (2004, 2006) compared shear wave anisotropy and polarizations to the orientations of bedding planes and fractures from high resolution electrical conductivity image logs through fractured granites and tilted sediments in the SAFOD project, concluding that the anisotropy both local and, based on other seismic measurements, more distant from the borehole was controlled by the state of stress. In drilling of the igneous oceanic crust near midocean ridges in the Atlantic and Indian oceans, Iturrino et al. (2005) interpreted variations in the fast shear wave azimuth χ_F to be controlled by either rock mass texture or the directions of regional compression depending on the depth. H.-Y. Wu et al. (2007) and Y.-H. Wu et al. (2008) linked changes in anisotropy and χ_F to the severity of shale bedding dip and fractures in the vicinity of the inferred Chi-Chi earthquake slip zone; and they linked abrupt rotations in χ_F to variations in lithology and structure. Goswami et al. (2019, 2020) carried out an extensive logging campaign through igneous Deccan traps and into granitic basement near Koyna, India. They found correlations between fractures, stress directions inferred from BOs and DITFs, dipole shear wave anisotropy and χ_F. However, to the best of our knowledge, there are scant comparable studies in the literature in which these differing logging methods have been used in a combined analysis in cratonic metamorphic terranes.

2.4 Geophysical Logs

2.4.1 Natural γ-ray Tool: This tool measures the level of natural radioactivity from the rock mass that originates from naturally occurring unstable isotopes of U, Th, and K. The instrument is almost always employed in logging campaigns since the repeatable response is often used as the depth standard, against which various different logging runs may be calibrated. The calibrated instrument reports the level of radioactivity on a relative scale of American Petroleum Institute (API) units.

2.4.2 Photoelectric Factor Tool: The photoelectric factor P_e is a semi-quantitative measure of the elemental composition of the material surrounding the borehole, and is based on the attenuation of soft γ-rays, the absorption of which within the electronic shells of the elements is accommodated by the expulsion of a "photo-electron". Essentially, the P_e depends on the atomic number Z according to $P_e = [Z/10]^{3.6}$ and hence the value is highly sensitive to the elements in the minerals of the rock. One advantage of this measure is that the influence of density is mostly removed and therefore the observation can provide some insights into the composition. Discussions of this tool primarily focus on interpretations in sedimentary environments where the principal minerals may be quartz, calcite, or dolomite. Applications to crystalline environments are not so common, but a listing of P_e values for other minerals appears at http://www-odp.tamu.edu/publications/209_IR/chap_02/chap_02.htm (Accessed December 11, 2021).

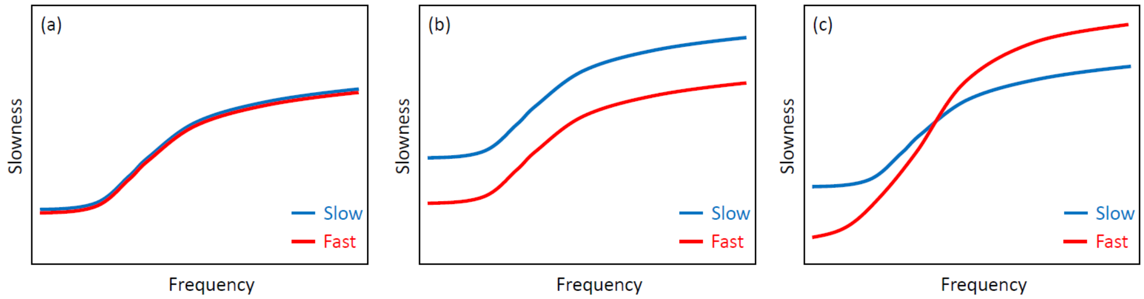

Figure S1. Representative dispersion plots displaying fast (red) and slow (blue) flexural wave slowness as a function of frequency. (a) overlapping pattern in the isotropic case or in the case where the wellbore is aligned with the axial symmetry axis of a transversely isotropic formation (b) separated and parallel pattern in the intrinsic anisotropic case (c) crossover pattern in the stress-induced anisotropic case.

Table S1. Standard Isotropic Equations for Calculating Elastic Moduli

Elastic moduli	Equations
Shear modulus μ (SMG)	$\mu = \rho V_S^2$
Bulk modulus K	$K = \rho\left[V_P^2 - \frac{4}{3}V_S^2\right]$
Young's modulus E (YME)	$E = \frac{9K\mu}{3K+\mu} = 3\rho\frac{\left[V_P^2 - \frac{4}{3}V_S^2\right]V_S^2}{V_P^2 - V_S^2}$
Poisson's ratio ν (PR)	$\nu = \frac{E}{2\mu} - 1 = \frac{1}{2}\frac{V_P^2 - 2V_S^2}{V_P^2 - V_S^2}$

Table S2. Completion History of the Hunt Well – Expanded from Chan (2013)

Event	**Date**	**Remarks**
Drilling Session #1		UWI: 00/07-32-089-10W4/0 Company: Archean Corporation KB: 409.3 m TVD: 1649.0 m Mud Density 1060 kg/m^3 to 1100 kg/m^3
Spud date	Sept. 1, 1994	
Rig on site	Early Sept., 1994	
Drilling began	Early Sept., 1994	
Casing #1	Sept. 1, 1994	Casing liner outside diameter 339.7 mm Shoe set depth: 94 m
Casing #2	Sept. 10, 1994	Casing liner outside diameter: 244.5 mm Shoe set depth: 598.2 m
Drilling completed	Oct. 8, 1994	At 1649.0 m
Service rig released	Oct. 8, 1994	

Rig on site	Oct. 8, 1994	For Schlumberger logging
Logging (Schlumberger)	Oct. 8, 1994	Run #1: DLL, MSFL Run #2: CNL, LDT, NGT Run #3: FMI
Drilling operations suspended temporarily	Oct. 9, 1994	
Rig released	Oct. 10, 1994	
Suspended drilling operations	Nov. 2, 1994	Suspended indefinitely. Bridge plug set at 540 m

Archean Corporation renamed to Anhydride Corporation on June 10, 1996.
Director: Mr. C. Warren Hunt

Drill out permanent bridge plugs and test intervals in granite formation

Rig on site	Sept. 25, 2002	
Drill out cement	Sept. 27, 2002	From 533.55 to 539.59 m
Drill out bridge plug 1	Sept. 27, 2002	At 539.59 m
Drill out bridge plug 2	Sept. 28, 2002	At 596.23 m
Clear tight spots	Sept. 29 – 30, 2002	From 1187.48 to 1216.16 m, and possibly a few other tight spots between 1283.29 to 1640 m
RIH with inflate straddle packer	Oct. 2, 2002	
Swab tests	Oct. 2 – 8, 2002	
Packer test	Oct. 7, 2002	Bottom of top packer at 873.0 m, pressurized at different feed rates. ISIP reported at 7 MPa dropping to 5.5 MPa in 13 minutes
Packer test	Oct. 11, 2002	Bottom of top packer at 1370 m, pressurized at 11.5 MPa, held pressure for long time without dropping
Rig released	Oct. 15, 2002	
Drilling Session #2		UWI: 00/07-32-089-10W4/2 KB: 409.3 m TVD: 2363.3 m Mud Density 1005 kg/m^3 to 1040 kg/m^3
Spud date	Dec. 13, 2002	
Drill out cement and bridge plug	Dec. 16, 2002	

Drilling began	Dec. 17, 2002	Bit size: 222 mm, TVD: 1649 to 1654 m Bit size: 200 mm, TVD: 1656.4 to 2347 m Bit size: 199 mm for coring
Coring #1	Dec. 20, 2002	Recovered 1.22 m core between 1656.4 to 1657.82 m
Coring #2	Jan. 5-6, 2003	Recovered 2.17 m core between 2347.52 to 2350.21 m
Coring #3	Jan. 7, 2003	At 2351 m
Logging (Schlumberger)	Jan. 7, 2003	Run #1: FMI and DSI logs from 2351 to 1600 m Run #2: TLD, CNL, NGT, HRLA, CAL logs from 2351 to 1600 m
Coring #4	Jan. 8-9, 2003	Recovered 11.92 m core from 2351.42 to 2363.34 m
Drilling completed	Jan. 9, 2003	At 2363.3 m
DST #1	Jan. 9-10, 2003	From 1755 to 1800 m
DST #2	Jan. 10-11, 2003	From 2345 to 2363 m
DST #3	Jan. 11-12, 2003	From 1640 to 1664 m, miss run
DST #4	Jan. 12, 2003	From 1645 to 1670 m, miss run
DST #5	Jan. 13, 2003	From 1640 m to 1683 m, bottom hole sample showed ground-up granite and small speckles of metal of unknown source
DST #6	Jan. 13-14, 2003	At 2363 m
Set bridge plug	Jan. 15, 2003	At 590 m
Rig released	Jan. 15, 2003	
Completion and Workover **Drill out permanent bridge plug at 590 m KB, swab and evaluate open hole**		
Rig on site	Jan. 30, 2003	
Production tubing running in hole (RIH)	Feb. 8, 2003	Tubing size: 89 mm Tubing collar: 0.15 m Tubing bottom: 2329.06 m
Hole camera	Feb. 24-25, 2003	Fluid entry found at 632.09 to 640.0 m, 647.94 to 754.81 m, 769.64 to 788.56 m. Possible inflow at 1646 m, 1550 m. No inflow at intervals tested below 1645 m.
Casing #3	Feb. 28, 2003	Casing liner outside diameter: 177.8 mm Shoe set depth: 1005.7 m
Run in production tubing	Mar. 5, 2003	
Rig released	Mar. 14, 2003	

Swab rig in	Mar. 17, 2003	Continued swabbing but little additional fluids produced
Swab tests	Feb. 9 – Mar. 20, 2003	Extensive swabbing, could not recover any additional fluids on last runs, total fluid swabbed is 66.71 m^3 of salt water with no signs of oil or gas
Swab rig out	Mar. 20, 2003	
2004 – 2008: Temperature measurements were made by GeoPos at unknown date. Data is not available.		

Temperature Logging (See Majorowicz et al., 2014)

Temperature logging #1	Dec. 7-9, 2010	Initial run into borehole did not encounter fluid level until 2192 m as indicated by pressure and temperature curves. Casing collar locator (CCL) confirms that production tubing remains in place. Pumped 51-52 m^3 of water into borehole over two days and logged from surface to 2333.7 m Standard logging package included pressure, gamma ccl, temperature and lightning unit including travel time. LSAT Lonkar spectral log Fluid level dropped rapidly. Measured water level at 928 m on Dec. 12, 2010.
Temperature logging #2	Jun. 14-15, 2011	Repeat temperature log to check on the thermal stability of the well. The well was topped up ~2 weeks with municipal water before logging date. Logging as above Fluid level was observed at ~ 65 m.
Remove Production Tubing and Slim Tool Logging		
Rig on site	Jul. 8, 2011	
Removal of production tubing	Jul. 8-9, 2011	248 production tubes removed prior to open hole logging
Rig released	Jul. 9, 2011	
Logging (ICDP-OSG)	Jul. 13-16, 2011	Logging and Vertical Seismic Profiling Carried out by Operational Support Group, GFZ Attempt ultrasonic borehole image log, but centralization springs unable to open

		sufficiently in large diameter below casing. See Chan (2013) for a list of logs and Chan & Schmitt (2015) for descriptions of VSP measurements. Blockage at 1360 m prevents some logs from being run.
Phase 1 Environmental Site Assessment	October 22, 2012	Done by WorleyParsons
Clear Blockage and Commercial Logging		
Service rig on site	November 5, 2013	
Clear blockage	November 7, 2013	Flush well to prepare for logging
Logging	November 8, 2013	Open hole logging from 1005 to 2315 m. New data presented in this manuscript.
Rig released	November 9, 2013	

Note. This material is extracted from the summary of Appendix A of Chan (2013) but updated to include the additional geophysical logging activities described earlier from late November 2013.

Text S3. Calculations for Figure 6

Figure 6 shows how the *P*-, the S_H- and the S_V- wave speeds of vertical propagation change in two examples of foliated metamorphic rocks with the dip angle β_m. We calculated these velocities using both a general program that solves the eigenvalues of the Christoffel equation and the direct analytic solutions for the phase velocities (e.g., Thomsen, 1986):

$$V_{SH}(\beta_m) = \left[\frac{C_{66}\sin^2\beta_m + C_{44}\cos^2\beta_m}{\rho}\right]^{1/2} \quad \text{(S5)}$$

$$V_{SV}(\beta_m) = \left[\frac{(C_{11}+C_{44})\,sin^2\beta_m + (C_{33}+C_{44})\,cos^2\beta_m - D(\beta_m)}{2\rho}\right]^{1/2} \quad \text{(S6)}$$

$$V_P(\theta) = \left[\frac{(C_{11}+C_{44})\,sin^2\beta_m + (C_{33}+C_{44})\,cos^2\beta_m + D(\beta_m)}{2\rho}\right]^{1/2} \quad \text{(S7)}$$

$$D(\beta_m) = \sqrt{[(C_{11}-C_{44})\,sin^2\beta_m - (C_{33}-C_{44})\,cos^2\beta_m]^2 + 4(C_{13}+C_{44})^2\beta_m\,cos^2\beta_m} \quad \text{(S8)}$$

Note that the Thomsen's parameter δ is also given for the two samples in Figure 6. This is a measure of the wave speed surface curvature at angles away from the principal directions of the material (here parallel and perpendicular to the foliation plane), which is given by:

$$\delta = \frac{(C_{13}+C_{44})^2 - (C_{33}-C_{44})^2}{2C_{33}(C_{33}-C_{44})} \quad \text{(S9)}$$

where the C_{ij} is the value of the elastic stiffness (in GPa) of the Voigt reduced notation for a TI medium:

$$C = \begin{bmatrix} C_{11} & C_{11}-2C_{66} & C_{13} & 0 & 0 & 0 \\ C_{11}-2C_{66} & C_{11} & C_{13} & 0 & 0 & 0 \\ C_{13} & C_{13} & C_{33} & 0 & 0 & 0 \\ 0 & 0 & 0 & C_{44} & 0 & 0 \\ 0 & 0 & 0 & 0 & C_{44} & 0 \\ 0 & 0 & 0 & 0 & 0 & C_{66} \end{bmatrix}$$

For the Hunt Well sample with density ρ = 2620 kg/m^3, the values measured at elevated confining pressure by Chan (2013) are:

$$C = \begin{bmatrix} 87.4 & 39.6 & 18.3 & 0 & 0 & 0 \\ 39.6 & 87.4 & 18.3 & 0 & 0 & 0 \\ 18.3 & 18.3 & 68.0 & 0 & 0 & 0 \\ 0 & 0 & 0 & 19.9 & 0 & 0 \\ 0 & 0 & 0 & 0 & 19.9 & 0 \\ 0 & 0 & 0 & 0 & 0 & 23.9 \end{bmatrix}$$

The second sample is from as yet unpublished results on a mylonite sample near the Alpine Fault, New Zealand with density ρ = 2750 kg/m^3 with

$$C = \begin{bmatrix} 98.2 & 24.03 & 10.33 & 0 & 0 & 0 \\ 24.03 & 98.2 & 10.33 & 0 & 0 & 0 \\ 10.33 & 10.33 & 80.61 & 0 & 0 & 0 \\ 0 & 0 & 0 & 30.65 & 0 & 0 \\ 0 & 0 & 0 & 0 & 30.65 & 0 \\ 0 & 0 & 0 & 0 & 0 & 37.09 \end{bmatrix}$$

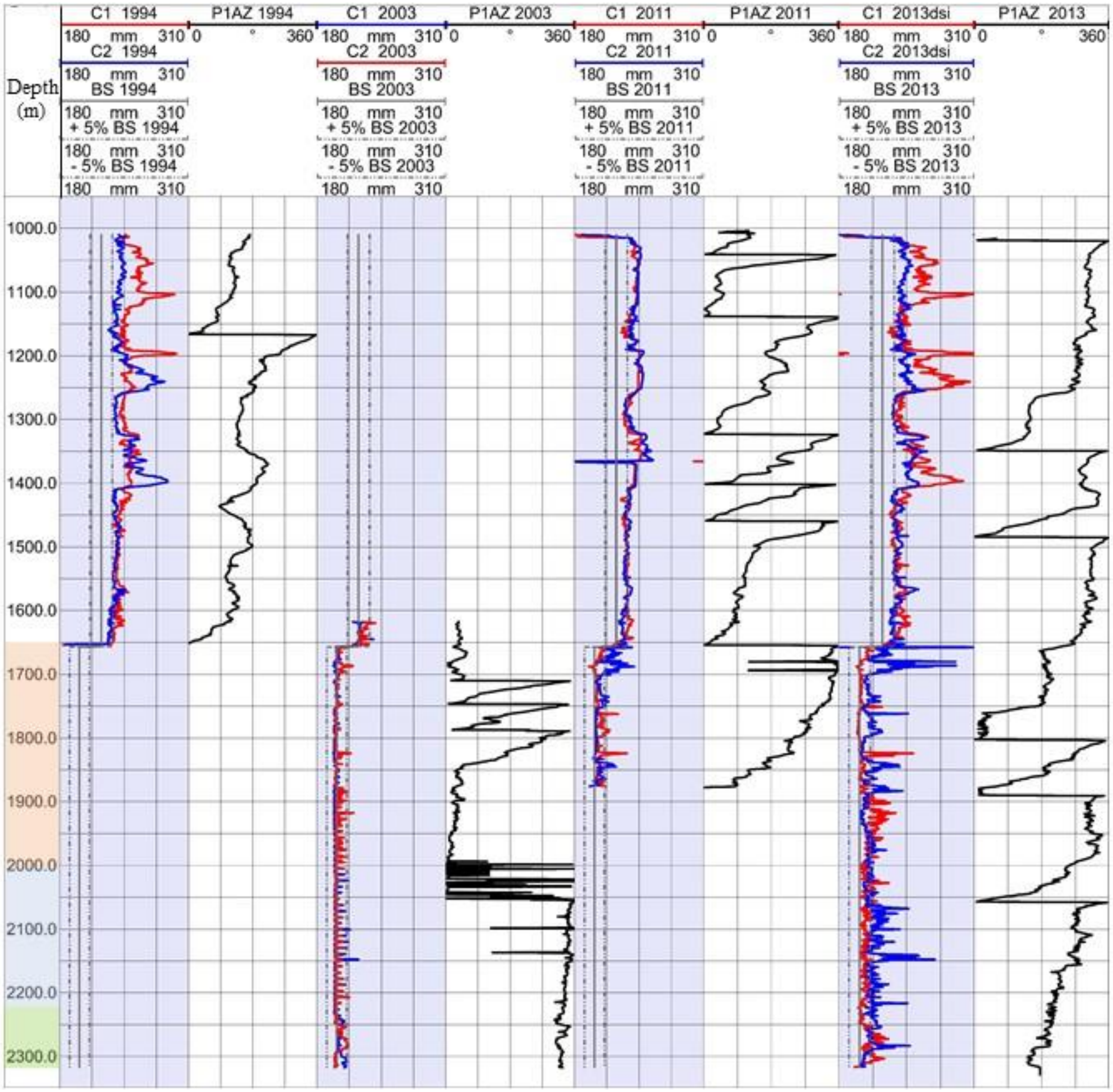

Figure S2. Calipers along with P1AZs from oriented 4-arm caliper logs obtained from the *FMI-1994* and *FMI-2003* runs, the *Dipmeter-2011* run, and the *PPC DSI-2013* run.

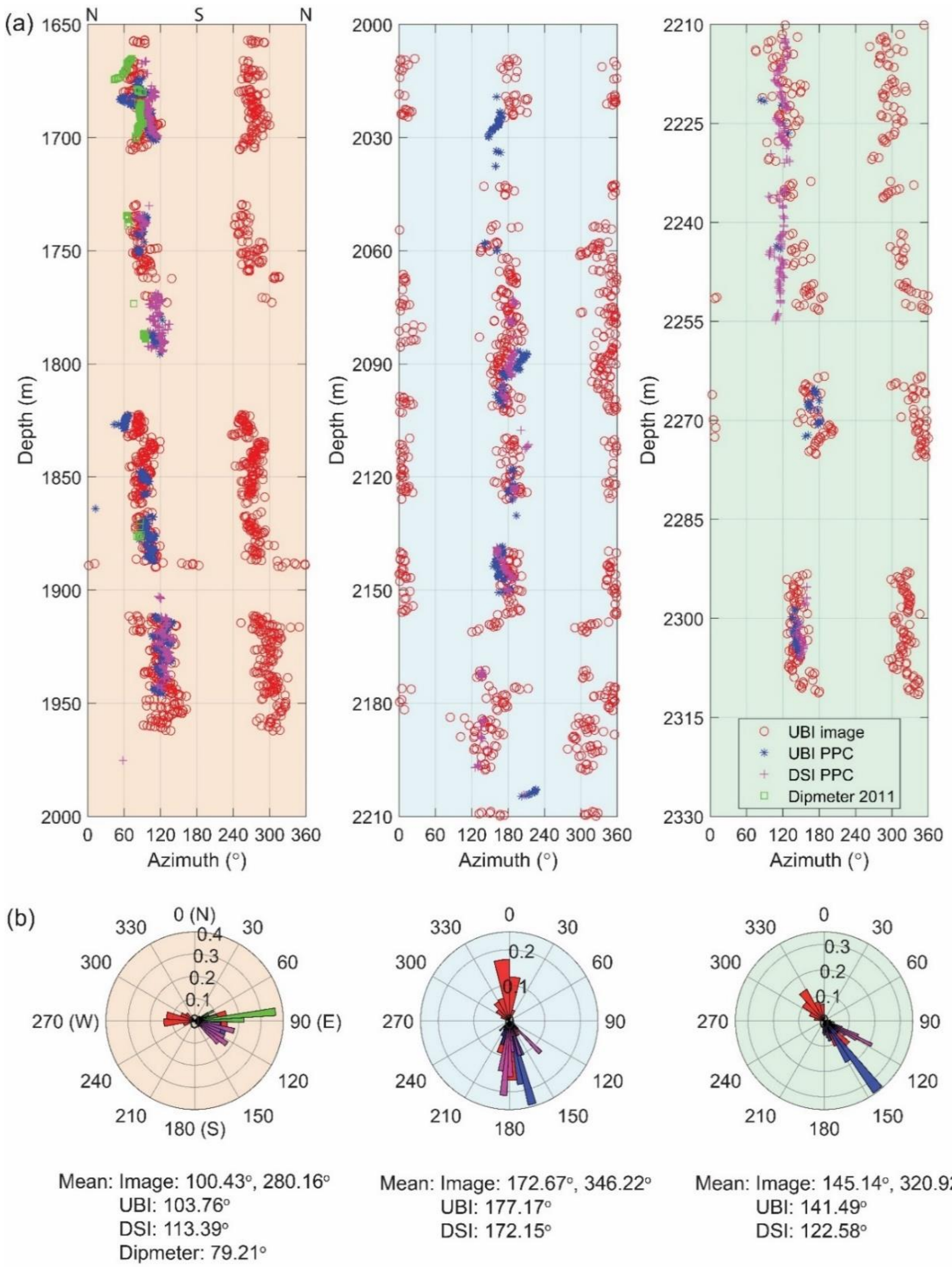

Figure S3. (a) Breakout azimuths from image logs (repeated from Figure 9) and from elongation directions of the consecutive caliper logs. (b) From left to right, the rose histograms represent the BO azimuth distribution at 1650-2000 m, 2000-2210 m, and 2210-2320 m respectively. The color codes follow the color codes in (a).

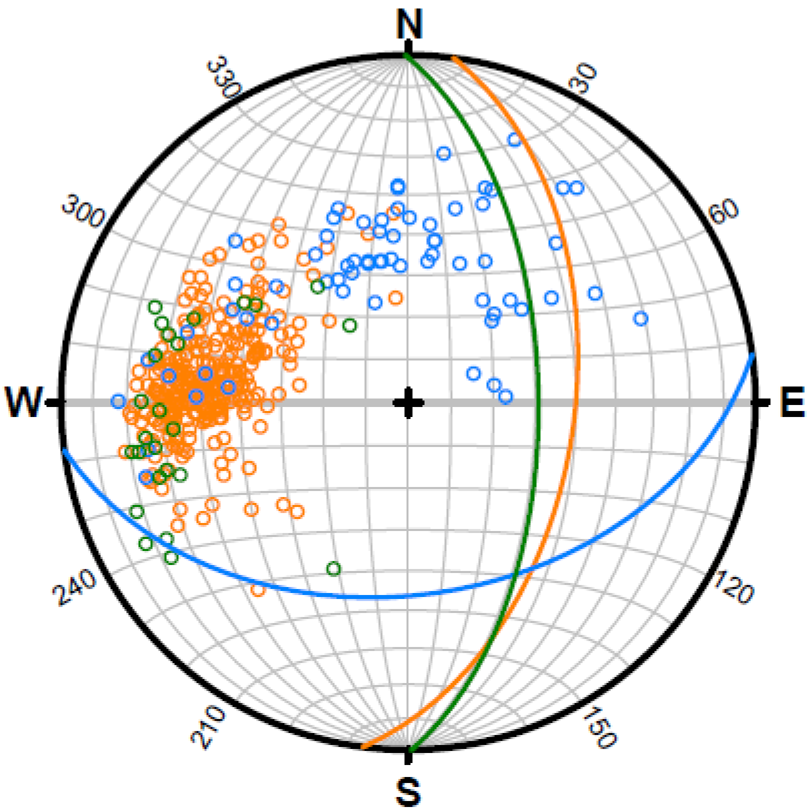

Figure S4. Individual poles used for the calculation of the Kamb contours in Figure 10. Orange, blue, and green hollow circles represent the foliation poles at the depth of 1000-2000 m, 2000-2210 m, and 2210-2330 m respectively. Solid great circles represent the corresponding average foliation orientations at these three depth intervals.

304

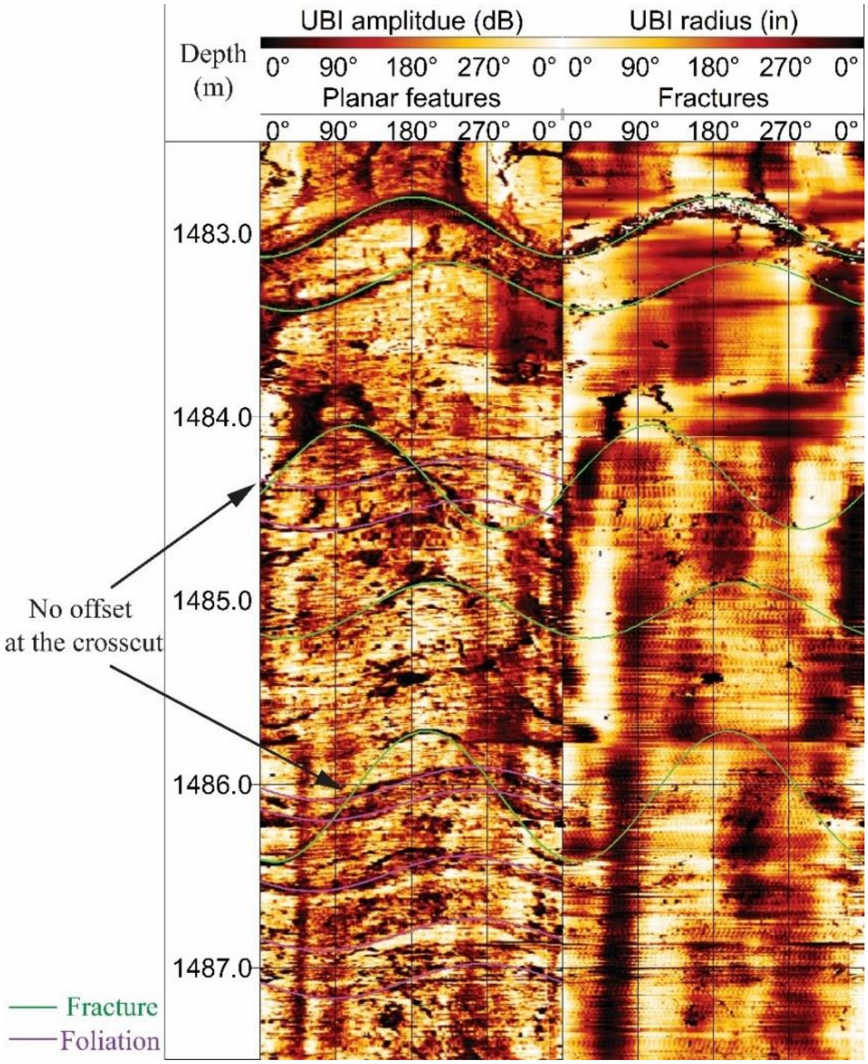

305

306 **Figure S5.** Planar features from UBI amplitude (left panel) and transit time (right panel)
307 images. Green and purple sinusoids represent identified fractures and foliations
308 respectively.

Table S3. Fractures Picked from UBI Image Logs

Depth (m)	Dip azimuth (°)	Dip angle (°)
1153.43	355.68	64.47
1159.22	124.30	75.21
1160.78	112.43	70.24
1481.18	84.75	46.13
1481.53	319.78	66.20
1482.96	3.20	53.05
1483.29	39.71	49.82
1484.33	288.15	66.71
1485.05	33.63	54.05
1486.07	17.85	72.18
1488.83	39.06	78.93
1537.39	351.34	55.79
1543.43	295.28	58.69
1543.58	291.51	57.70
1712.18	90.10	47.08
1712.27	88.42	51.00
1747.10	75.69	48.21
2183.42	58.11	68.51
2289.23	66.57	68.76
2311.59	9.12	65.15

310 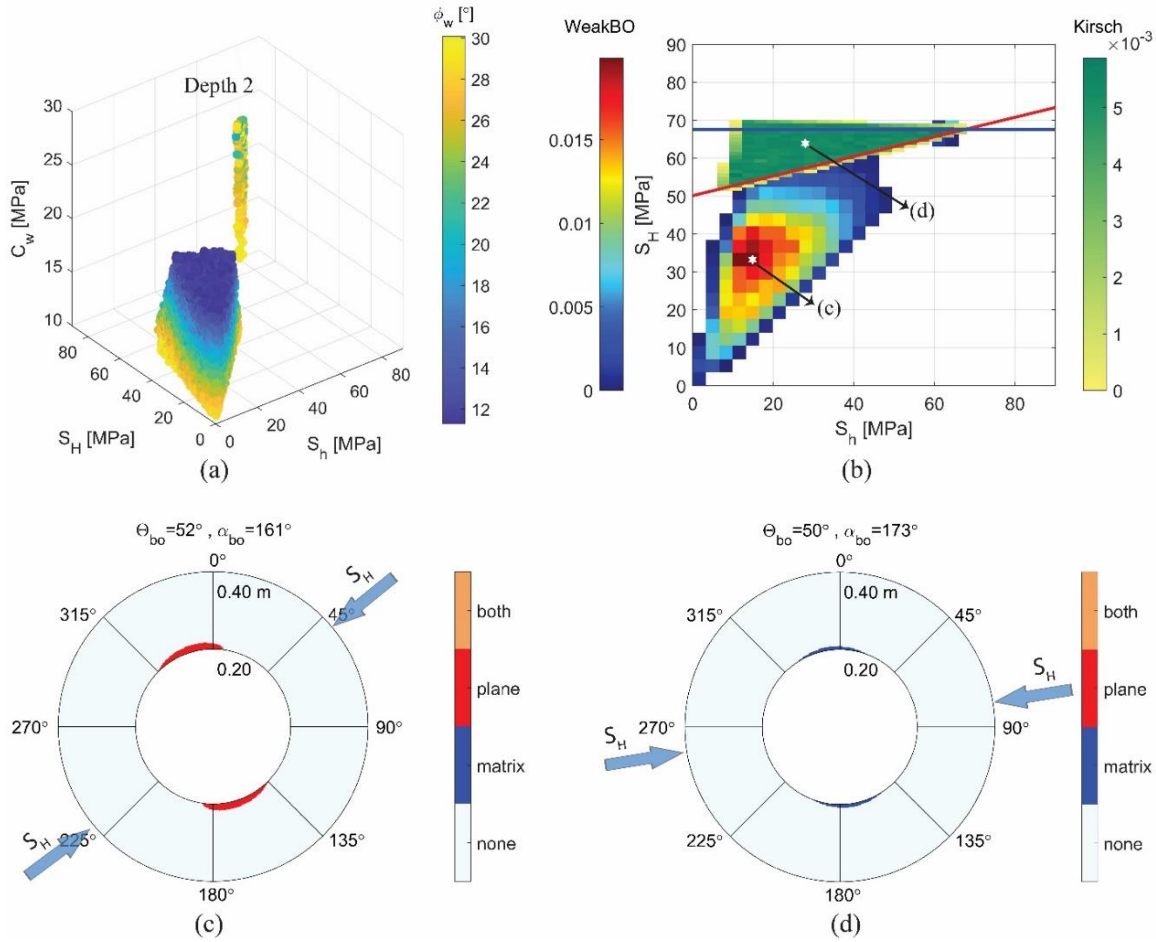

311 **Figure S6.** Feasible stress magnitudes and modelled failure patterns at the depth zone 2
312 (2000 m).

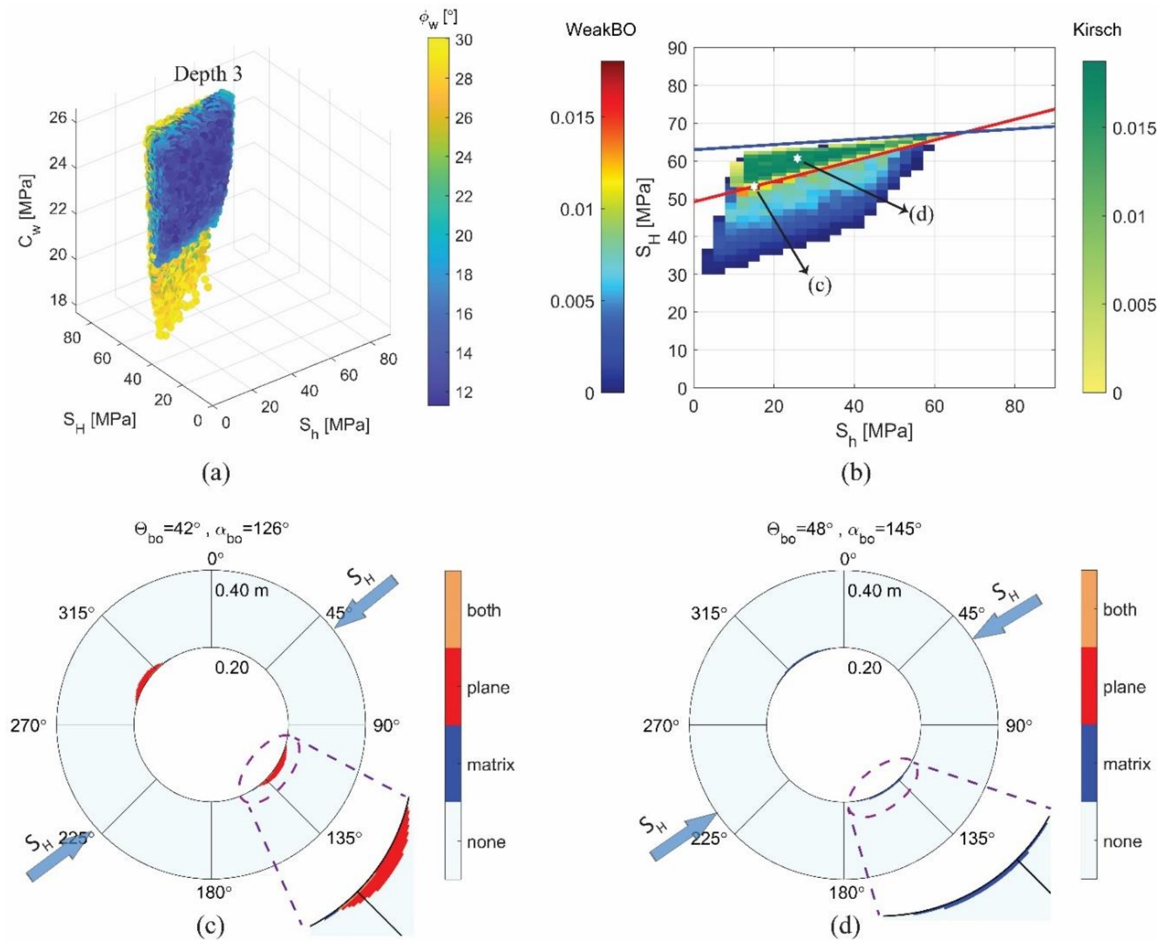

Figure S7. Feasible stress magnitudes and modelled failure patterns at the depth zone 3 (2210 m).

Text S4. Insensitivity of Equation 2

To reiterate, Eq. 2 is widely used to give estimates of the greatest horizontal compressive stress S_H if the unconfined compressive strength (UCS), the magnitude of the least horizontal compressive stress (S_h), and the full breakout width given as a circumferential angle Θ are known as per:

$$S_H = \frac{UCS - S_h(1 - 2\cos\Theta)}{1 + 2\cos\Theta}$$

Estimation of S_H remains difficult, and therefore the usage of this equation is popular as often S_h, UCS, and Θ can be measured through a combination of borehole and core measurements (Schmitt et al., 2012; Zoback et al., 2003).

In Figure S8, S_H is calculated as a function of Θ for S_h = 20 MPa and UCS = 135 MPa which are representative values found in the study. This plot shows that S_H is largely insensitive to the breakout width at least up to Θ ~45°, and this helps to explain the wide ranges of possible realizations in the modelling for the isotropic case.

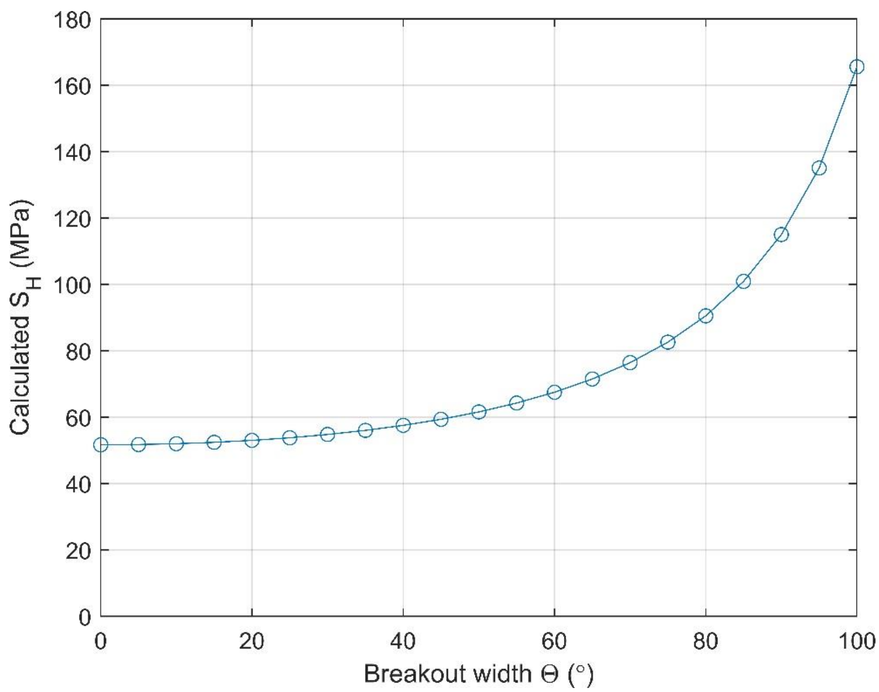

Figure S8. Calculated greatest horizontal compressive stress S_H as a function of breakout width Θ for the case with S_h = 20 MPa and UCS = 135 MPa according to Eq. 2.

Reference

Amadei, B. (1983). *Rock anisotropy and the theory of stress measurements*. Berlin: Springer-Verlag. https://doi.org/10.1007/978-3-642-82040-3

Azzola, J., Valley, B., Schmittbuhl, J., & Genter, A. (2019). Stress characterization and temporal evolution of borehole failure at the Rittershoffen geothermal project. *Solid Earth*, *10*(4), 1155–1180. https://doi.org/10.5194/se-10-1155-2019

Bell, J. S., & Gough, D. I. (1979). Northeast-southwest compressive stress in Alberta evidence from oil wells. *Earth and Planetary Science Letters*, *45*(2), 475–482. https://doi.org/10.1016/0012-821X(79)90146-8

Boness, N. L., & Zoback, M. D. (2004). Stress-induced seismic velocity anisotropy and physical properties in the SAFOD Pilot Hole in Parkfield, CA. *Geophysical Research Letters*, *31*(15), L15S17. https://doi.org/10.1029/2003GL019020

Boness, N. L., & Zoback, M. D. (2006). A multiscale study of the mechanisms controlling shear velocity anisotropy in the San Andreas Fault Observatory at depth. *Geophysics*, *71*(5), F131–F146. https://doi.org/10.1190/1.2231107

Brudy, M., & Zoback, M. D. (1999). Drilling-induced tensile wall-fractures: Implications for determination of in-situ stress orientation and magnitude. *International Journal of Rock Mechanics and Mining Sciences*, *36*(2), 191–215. https://doi.org/10.1016/S0148-9062(98)00182-X

Chan, J. (2013). *Subsurface geophysical characterization of the crystalline Canadian Shield in Northeastern Alberta: implications for geothermal development*. *Master thesis*. Edmonton: University of Alberta. https://doi.org/10.7939/R3BR8MQ6B

Chan, J., & Schmitt, D. R. (2015). Initial seismic observations from a deep borehole drilled into the Canadian Shield in northeast Alberta. *International Journal of Earth Sciences*, *104*(6), 1549–1562. https://doi.org/10.1007/s00531-014-1110-x

Fang, X., Cheng, A., & Fehler, M. C. (2015). Investigation of borehole cross-dipole flexural dispersion crossover through numerical modeling. *Geophysics*, *80*(1), D75–D88. https://doi.org/10.1190/geo2014-0196.1

Goswami, D., Roy, S., & Akkiraju, V. V. (2019). Delineation of damage zones from 3 km downhole geophysical logs in the Koyna Seismogenic Zone , Western India. *Journal of Geophysical Research: Solid Earth*, *124*(6), 6101–6120. https://doi.org/10.1029/2018JB017257

Goswami, D., Hazarika, P., & Roy, S. (2020). In situ stress orientation from 3 km borehole image logs in the Koyna Seismogenic Zone, western India: implications for transitional faulting environment. *Tectonics*, *39*(1), e2019TC005647. https://doi.org/10.1029/2019TC005647

Gough, D. I., & Bell, J. S. (1982). Stress orientations from borehole wall fractures with examples from Colorado, east Texas, and northern Canada. *Canadian Journal of Earth Sciences*, *19*(7), 1358–1370. https://doi.org/10.1139/e82-118

Hiramatsu, Y., & Oka, Y. (1962). Analysis of stress around a circular shaft or drift excavated in ground in a three dimensional stress state. *Journal of Mining and Metallurgy Institute of Japan*, *78*, 93–98.

Iturrino, G. J., Goldberg, D., Glassman, H., Patterson, D., Sun, Y. F., Guerin, G., & Haggas, S. (2005). Shear-wave anisotropy from dipole shear logs in oceanic crustal environments. *Geological Society Special Publication*, *240*, 117–131. https://doi.org/10.1144/GSL.SP.2005.240.01.10

Kerkela, S., & Stock, J. M. (1996). Compression directions north of the San Fernando Valley determined from borehole breakouts. *Geophysical Research Letters*, *23*(23), 3365–3368. https://doi.org/10.1029/96GL03054

Kirsch, E. G. (1898). Die theorie der elastizitat und die bedurfnisse der festigkeitslehre. *Zeitschrift Des Vereines Deutscher Ingenieure*, *42*(29), 797–807.

Majorowicz, J., Chan, J., Crowell, J., Gosnold, W., Heaman, L. M., Kück, J., et al. (2014). The first deep heat flow determination in crystalline basement rocks beneath the Western Canadian Sedimentary Basin. *Geophysical Journal International*, *197*(2), 731–747. https://doi.org/10.1093/gji/ggu065

Morin, M. L. (2017). *Natural and drilling induced fractures in the Grosmont Formation, Alberta: implications for the state of stress*. *Master thesis*. Edmonton: University of Alberta. https://doi.org/10.7939/R3B56DJ60

Schmitt, D. R., Currie, C. A., & Zhang, L. (2012). Crustal stress determination from boreholes and rock cores: fundamental principles. *Tectonophysics*, *580*, 1–26. https://doi.org/10.1016/j.tecto.2012.08.029

Sinha, B. K., Norris, A. N., & Chang, S.-K. (1994). Borehole flexural modes in anisotropic formations. *Geophysics*, *59*(7), 1037–1052. https://doi.org/10.1190/1.1443660

Stork, A. L., Nixon, C. G., Hawkes, C. D., Birnie, C., White, D. J., Schmitt, D. R., & Roberts, B. (2018). Is CO2 injection at Aquistore aseismic? A combined seismological and geomechanical study of early injection operations. *International Journal of Greenhouse Gas Control*, *75*, 107–124. https://doi.org/10.1016/j.ijggc.2018.05.016

Thomsen, L. (1986). Weak elastic anisotropy. *Geophysics*, *51*(10), 1954–1966. https://doi.org/https://doi.org/10.1190/1.1442051

Winkler, K. W. (1997). Acoustic evidence of mechanical damage surrounding stressed boreholes. *Geophysics*, *62*(1), 16–22. https://doi.org/10.1190/1.1444116

Wu, H.-Y., Ma, K.-F., Zoback, M. D., Boness, N., Ito, H., Hung, J.-H., & Hickman, S. (2007). Stress orientations of Taiwan Chelungpu-Fault Drilling Project (TCDP) hole-A as observed from geophysical logs. *Geophysical Research Letters*, *34*(1), L01303. https://doi.org/10.1029/2006GL028050

Wu, Y.-H., Yeh, E.-C., Dong, J.-J., Kuo, L.-W., Hsu, J.-Y., & Hung, J.-H. (2008). Core-log integration studies in hole-A of Taiwan Chelungpu-fault Drilling Project. *Geophysical Journal International*, *174*(3), 949–965. https://doi.org/10.1111/j.1365-246X.2008.03841.x

Zoback, M. D., Barton, C. A., Brudy, M., Castillo, D. A., Finkbeiner, T., Grollimund, B. R., et al. (2003). Determination of stress orientation and magnitude in deep wells. *International Journal of Rock Mechanics and Mining Sciences*, *40*(7–8), 1049–1076. https://doi.org/10.1016/j.ijrmms.2003.07.001